17th INTERNATIONAL CONGRESS of the Geological Society of Greece

BULLETIN OF THE GEOLOGICAL SOCIETY OF GREECE, SP. PUBL.

EXTENDED ABSTRACT 136

Climate changes, neglected and emerging diseases.

P. Karanis[1]

(1) Department of Basic and Clinical Sciences, University of Nicosia Medical School, Cyprus, karanis.p@unic.ac.cy

The climate crisis is one of humanity's most pressing challenges and has visible and widespread impacts on public health. The presentation links the climate crisis to disease distribution, research, and control. From rising temperatures and the increasing frequency of extreme weather events to the emergence of climate-related diseases and nutritional inequalities, the climate crisis seriously threatens the health and well-being of the population. Using the interdisciplinary approach, we report on the challenges emerging, reemerging, and neglected diseases arising and being influenced by the climate crisis and how they affect our health and everyday life.

Climate change is expected to significantly impact neglected tropical diseases (NTDs), affecting their transmission patterns and geographic distribution. Vector-borne NTDs are particularly susceptible to environmental changes, as climate influences vector biology and habitat. Rising temperatures and altered rainfall patterns may lead to the emergence and re-emergence of NTDs in previously unaffected regions. Current NTD mitigation strategies, including mass drug administrations, are vulnerable to global events like the COVID-19 pandemic. There is a need for improved surveillance, monitoring, and research to understand better and address the complex interactions between climate change and NTDs. We will highlight the synergistic effects and advocate for a One Health concept by integrating insights from climate science, ecology, geology, water resources and medicine to address the interdisciplinary relation and the gaps to strengthen the resilience of Mediterranean health systems.

Neglected tropical diseases (NTDs) are diverse tropical infections caused by various pathogens, including viruses, bacteria, protozoa, and parasitic worms or helminths. Globalization and increased international trade and travel bring vectors and pathogens together, even where they are limited and prevalent. Climate change is another force driving the expansion of NTDs. A warmer and wetter climate has made the continent more welcoming to vectors of debilitating and sometimes deadly pathogens.

Although the impact of these diseases is not on the same scale in any country compared to tropical countries, cases of vector-borne diseases have become endemic in countries where they were not prevalent before, and they are on the rise. No one country long thought itself safe from NTDs is free. Old certainties that antibiotics and drugs will defend against the risks have evaporated. As Earth warms, the creatures that spread neglected tropical diseases are gaining a foothold in many countries.

Climate, demographic, geological, and geopolitical changes and floods pose new challenges in surface water quality monitoring. They bring forth usual or unusual pathogens, thus requiring new test designs. This demands the development of faster and easier tests to control the quality of drinking or reusing treated wastewater at all points, from plants to end users.

NTDs are also characterized by inequity, which is closely associated with poverty. This inequity has given rise to neglect. Wealthy countries must prepare themselves for more cases. We will discuss and propose options for action and innovative approaches that we can adopt to address these challenges and safeguard public health in an era of climate uncertainty and existing, emerging, reemerging, and neglected diseases related to water supply and vector disease distribution.

One of the most concerning impacts of climate change on human health is the rising prevalence and altered distribution of vector-borne diseases greatly influenced by environmental factors. Tick-borne diseases represent a particularly pressing threat, as climatic shifts influence pathogen transmission dynamics, host-vector interactions, and the geographic spread of key vector species. Ticks are blood-feeding ectoparasites found in mammals, birds, and reptiles worldwide. Unlike nest-dwelling tick species, non-nidicolous ticks are found on vegetation, such as grasses and bushes, onto which they climb and wait to attach themselves to their prey. They feed by sucking blood from their hosts, which can be pets, farm or wild animals, and humans. Ticks are known as carriers for a wide range of pathogens, including viruses, bacteria, protozoa, and helminths, and therefore, numerous tick-borne diseases are transmitted through their bite. Ticks, like mosquitoes, are recognized as the leading global arthropod vectors of human diseases and of primary medical and veterinary importance. Beyond these immediate concerns, ticks are vectors for pathogens that significantly increase morbidity and mortality, amplifying rising public health costs and disease management challenges.

Greece is a popular summer destination for tourists worldwide. Tourists and immigrants represent a melting pot of human activities that brings many people from all over the world together and potentially serves as a source of contamination that can cause endemic infectious diseases on the islands and the whole country. During their

visit, they overconsume diverse water resources by swimming, drinking a lot of water, and eating a lot of fresh produce with minimal preparation, especially salad ingredients and leafy greens. The objective evaluation of the epidemiological status is complex due to the unknown levels of pathogenic contamination in the water supplies, the degree of swimming pool contamination, and the distribution of contaminated food irrigated with contaminated water. Environmental pressure thereby is created and affects both humans and wildlife.

The annual average temperature increases (°C) in four Mediterranean basin countries (Greece, Cyprus, Italy, and Tunisia) from 1960 to the present. Since the 1990s, temperatures in the region have accelerated, with projections suggesting further increases, particularly in the summer months. Under different climate scenarios, the temperature could rise by 2 to 6°C by the end of the century, with a potential summer temperature increase of up to 3°C if global temperatures rise by 2°C. These warming trends are expected to lead to more frequent and intense heat waves, which will pose significant challenges to humans.

Infections have been reported, although outbreaks have been reported in limited numbers. The absence of outbreak documentation indicates the lack of an efficient screening and detection system and that these threats are not on the authorities ' alarm agenda until an outbreak occurs. Global warming negatively influences public health, the environment, and wildlife. Responding to these One Health threats promptly is critical. Specific pathogens were the leading etiological agents of waterborne and foodborne outbreaks. The parasites ' dormant and transmissive stages can infect a broad host range with multiple transmission routes. Consumption of various vegetables, direct or indirect contact with infected food products and ingesting contaminated water through drinking or swimming can lead to a foodborne and waterborne outbreak. Food and water safety are critical global health concerns, with specific foodborne and waterborne pathogens threatening human and animal health and environmental stability. Addressing the detection and monitoring challenges to water resources, leafy greens, and water supplies will overlap two questions.

Climate change and its influence on emerging disease transmission threaten public health and countries ' economies. This perspective emphasizes a critical knowledge gap by exploring how climate-induced environmental changes interact synergistically with disease transmission dynamics to heighten disease risks in Mediterranean countries. Research on the combined effects of climate change and disease transmission will establish bridges and fill the gaps, offering an integrated perspective on the interconnected pathways through which climate change affects public health. By integrating climate science, ecology/ecological modelling, geology and public health aspects, research efforts will advance existing part of knowledge by developing a holistic framework for assessing climate-driven threats. It underscores the necessity of adaptive strategies, including improved disease surveillance, integrated disease management, and climate-informed policy interventions. One Health approach is a cornerstone of the proposed solutions, fostering cross-sectoral collaboration to enhance resilience against climate-driven emerging risks

17th INTERNATIONAL CONGRESS of the Geological Society of Greece

BULLETIN OF THE GEOLOGICAL SOCIETY OF GREECE, SP. PUBL.

EXTENDED ABSTRACT 137

AI-Driven Approaches for Landslide Modeling: Challenges and Opportunities

Karantanellis E.[1], Marinos V.[2], Braun A.[3]
(1) University of Michigan, Ann Arbor, USA, stratis@umich.com
(2) National Technical University of Athens, Athens, Greece
(3) Technische Universität Berlin, Germany

Introduction

Landslides are among the most pervasive and destructive natural hazards, threatening lives, infrastructure, and ecosystems worldwide. Triggered by factors such as intense rainfall, earthquakes, volcanic activity, and human-induced changes, landslides are inherently complex phenomena influenced by dynamic interactions between geological, hydrological, and climatic conditions. Effective prediction and risk mitigation are critical to minimizing their societal and environmental impacts. However, traditional modeling approaches, which often rely on deterministic or statistical frameworks, face significant limitations in capturing the multifaceted and nonlinear processes underlying landslide occurrence. In recent years, artificial intelligence (AI) has emerged as a transformative tool in addressing complex problems across various scientific domains (Catani, Nava, and Bhuyan 2025). In the field of landslide modeling, AI-driven approaches leverage machine learning (ML), deep learning (DL), and advanced data analytics to process large, heterogeneous datasets, uncover hidden patterns, and make predictions with unprecedented accuracy (Sun, Bocchini, and Davison 2020). These technologies offer new opportunities to improve landslide susceptibility mapping, hazard assessment, and early warning systems.

The integration of AI into landslide modeling is particularly timely given the increasing availability of high-resolution remote sensing data, real-time sensor networks, and global climate models. These data sources provide the foundational input for AI algorithms to identify correlations and interactions among diverse variables such as slope angle, soil properties, rainfall intensity, and vegetation cover. Moreover, AI's adaptability allows models to evolve with changing environmental conditions, making them highly suited for long-term hazard management in a rapidly changing world (Dahal and Lombardo 2022). Despite its promise, the application of AI in landslide modeling is not without challenges. Issues such as data quality and availability, model interpretability, and uncertainty quantification remain significant hurdles. Furthermore, the successful implementation of AI requires interdisciplinary collaboration, bridging expertise in geosciences, computer science, and engineering, and transparency for decision-makers. Addressing these challenges is crucial to unlocking the full potential of AI in landslide risk reduction. This study aims to explore the opportunities and challenges associated with AI-driven in landslide modeling. It provides a review of methodologies, evaluates effectiveness, and highlights emerging trends and research directions.

Challenges and Opportunities

In recent years, the integration of AI with geotechnical and environmental sciences has opened new avenues for enhancing landslide modeling accuracy and effectiveness. AI approaches leverage computational algorithms to learn from data, enabling the extraction of hidden insights and the development of robust predictive frameworks (Zhao et al. 2024). Data complexity and availability remain significant barriers in landslide modeling, largely because these models require input from diverse datasets spanning geological attributes, hydrological dynamics, land cover, and climatic variables. The heterogeneity of these data sources often complicates their integration into cohesive models. Geological maps, satellite imagery, rainfall records, and field measurements vary in scale, resolution, and format, necessitating extensive preprocessing pipelines to harmonize inputs. This process can be computationally intensive and prone to errors. Additionally, data scarcity in remote or underdeveloped regions limits the accuracy and scope of modeling efforts. For instance, in areas without detailed geological surveys, proxy variables are often used, introducing uncertainties. Noise and errors in data, such as interference in remote sensing imagery due to cloud cover or inaccuracies in manually collected field data, further exacerbate the challenge. High temporal resolution data, critical for capturing dynamic triggers such as rainfall or seismic events, are frequently unavailable, reducing the model's ability to identify precursors to landslide events.

The temporal and spatial variability of landslide occurrences adds another layer of complexity. Landslides are influenced by short-term events like extreme rainfall, as well as long-term processes such as progressive slope deformation driven by climate change. AI models must therefore be capable of addressing these overlapping timescales. On the spatial front, landslides range from localized slope failures to regional mass movements, and models trained on small-scale events may not generalize well to larger-scale phenomena. Variability in lithology, vegetation, and human

activities such as deforestation and construction introduces nonlinear and region-specific interactions, complicating predictions further. Capturing these dynamics requires multi-scale modeling approaches capable of representing both broad regional trends and localized instabilities (Dahal, Huser, and Lombardo 2024). Uncertainty in AI-driven landslide models is another critical challenge, stemming from both the inherent unpredictability of landslides and limitations in data and algorithms. Quantifying uncertainty is essential for practical applications, as decision-makers must understand the confidence level of predictions. Probabilistic approaches, such as Bayesian neural networks or ensemble methods, can address this need but often demand substantial computational resources. Validation of model outputs against historical landslide inventories is another challenge, as such inventories are frequently incomplete or biased toward more visible events. This bias can reduce the reliability of model predictions. Furthermore, high-dimensional AI models risk overfitting to limited training data, underscoring the importance of rigorous cross-validation and feature selection to ensure generalizability.

Despite these challenges, AI offers transformative opportunities for advancing landslide modeling. One of the most significant benefits is enhanced prediction accuracy. AI algorithms can analyze large, complex datasets to uncover intricate patterns and nonlinear relationships that traditional methods often overlook. For example, deep learning models can extract geomorphological features indicative of slope instability from high-resolution satellite imagery, leading to improved landslide susceptibility mapping. These models also provide insights into the relative importance of input variables, such as rainfall intensity versus slope angle, which can guide future data collection and mitigation strategies. The scalability of AI further enables the development of regional and global models with unprecedented detail. Real-time monitoring and early warning systems represent another area where AI can have a profound impact. By integrating with data sources such as Internet of Things (IoT) sensors (Mendoza-Cano et al. 2021), AI models can continuously update landslide risk assessments in near real-time. Advanced algorithms, including recurrent neural networks and long short-term memory networks, excel at detecting anomalies in time-series data, serving as early indicators of potential slope instability (Zhao et al. 2024). These systems can also facilitate community engagement by delivering timely warnings through mobile applications, empowering at-risk populations to take preventive action and minimizing casualties. AI-driven models are inherently adaptive, evolving with new data inputs and changing environmental conditions. This adaptability is particularly valuable in the context of climate change, where shifting weather patterns and land-use practices continuously alter landslide dynamics (Ajraoui et al. 2024). Continuous retraining ensures that models remain relevant and accurate over time. AI can also simulate hypothetical scenarios, such as the impact of land-use changes or extreme weather events, aiding long-term planning and resilience building. Moreover, by automating data analysis and hazard mapping tasks, AI reduces the cost of landslide risk management, making advanced solutions accessible even to regions with limited resources. Numerous open-source libraries e.g. for R and python, such as the Scikit-learn library, and the implementation of AI algorithms in GIS platforms or Google Earth Engine make AI methods highly accessible. AI is being used in a variety of ways to improve landslide modeling, including data collection and integration, real-time monitoring, predictive modeling and early warning systems.

Figure 1. Conceptual schematic plot of landslide modeling where different conceptual elements are integrated (created in Gemini).

Discussion

This review has examined the burgeoning field of AI-driven approaches for landslide modeling, highlighting their potential to revolutionize our understanding and management of these geohazards. We have observed a growing body of research demonstrating the superior performance of AI algorithms, particularly deep learning models, in capturing complex non-linear relationships within landslide datasets. This has resulted in improved accuracy, enhanced prediction capabilities, and the ability to handle high-dimensional and heterogeneous data. However, several critical challenges persist. Data scarcity and heterogeneity remain significant hurdles, hindering the development and validation of robust AI models. The lack of standardized data collection and sharing protocols exacerbates these issues. Furthermore, the inherent "black-box" nature of many AI models raises concerns regarding interpretability and the potential for unintended biases. This lack of transparency can hinder trust and limit the widespread adoption of AI-based landslide prediction systems. Despite these challenges, the potential benefits of AI are substantial. AI-driven approaches can significantly enhance early warning systems, enabling more accurate and timely predictions of landslide events. This can facilitate proactive evacuation procedures and minimize human casualties. Moving forward, several key research directions are crucial.

- **Data-centric workflows:** Prioritizing the development of robust data acquisition and sharing frameworks, including initiatives to improve data quality, standardize formats, and enhance data accessibility.
- **Cognitive AI:** Developing and implementing techniques to enhance the interpretability of AI models, such as feature importance analysis, visualization methods, and rule extraction algorithms.
- **Hybrid approaches:** Exploring hybrid models that combine the strengths of AI with traditional geotechnical and statistical methods, leveraging the interpretability and domain expertise of traditional approaches while benefiting from the predictive power of AI.
- **Real-world applications:** Focusing on the practical implementation of AI-based landslide models in real-world settings, including their integration into operational systems and decision-making processes.

Ultimately, the successful application of AI in landslide modeling requires a multidisciplinary approach. Collaboration between researchers, practitioners, policymakers, and the public is essential to address the challenges, maximize the benefits, and ensure the responsible and ethical development and deployment of AI-based landslide prediction and mitigation systems.

References

Ajraoui, Abdelrhani, Said Chakiri, Hammou Mansouri, Mohamed Benhaddou, Oussama Laassilia, and Abdelkrim Saouabe. 2024. "Landslide Prediction Methods: A Comparative Overview of Traditional and AI-Based Decision-Making Approaches." In *2024 International Conference on Decision Aid Sciences and Applications (DASA)*, 1–5. Manama, Bahrain: IEEE. https://doi.org/10.1109/DASA63652.2024.10836546.

Catani, Filippo, Lorenzo Nava, and Kushanav Bhuyan. 2025. "Artificial Intelligence Applications for Landslide Mapping and Monitoring on EO Data." In *Earth Observation Applications to Landslide Mapping, Monitoring and Modeling*, 119–45. Elsevier. https://doi.org/10.1016/B978-0-12-823868-4.00007-6.

Dahal, Ashok, Raphaël Huser, and Luigi Lombardo. 2024. "At the Junction Between Deep Learning and Statistics of Extremes: Formalizing the Landslide Hazard Definition." *Journal of Geophysical Research: Machine Learning and Computation* 1 (3): e2024JH000164. https://doi.org/10.1029/2024JH000164.

Dahal, Ashok, and Luigi Lombardo. 2022. "Explainable Artificial Intelligence in Geoscience: A Glimpse into the Future of Landslide Susceptibility Modeling." https://doi.org/10.1002/essoar.10512130.1.

Mendoza-Cano, O., R. Aquino-Santos, J. López-de La Cruz, R. M. Edwards, A. Khouakhi, I. Pattison, V. Rangel-Licea, et al. 2021. "Experiments of an IoT-Based Wireless Sensor Network for Flood Monitoring in Colima, Mexico." *Journal of Hydroinformatics* 23 (3): 385–401. https://doi.org/10.2166/hydro.2021.126.

Sun, Wenjuan, Paolo Bocchini, and Brian D. Davison. 2020. "Applications of Artificial Intelligence for Disaster Management." *Natural Hazards* 103 (3): 2631–89. https://doi.org/10.1007/s11069-020-04124-3.

Zhao, Tianjie, Sheng Wang, Chaojun Ouyang, Min Chen, Chenying Liu, Jin Zhang, Long Yu, et al. 2024. "Artificial Intelligence for Geoscience: Progress, Challenges, and Perspectives." *The Innovation* 5 (5): 100691. https://doi.org/10.1016/j.xinn.2024.100691.

17th INTERNATIONAL CONGRESS of the Geological Society of Greece

BULLETIN OF THE GEOLOGICAL SOCIETY OF GREECE, SP. PUBL.

EXTENDED ABSTRACT 138

Evaluation of Greek clay for pottery applications

Karountzou G.[1], Panagiotaki M.[1], Semitekolos D.[1], Charitidis C[1]

(1) Research Lab of Advanced, Composite, Nano-Materials and Nanotechnology (R-NanoLab), School of Chemical Engineering, National Technical University of Athens, 9 Heroon Polytechniou St., Zographos, Athens 15780, Greece, karountzou@chemeng.ntua.gr

Abstract

The use of clay in the ceramics industry is significant, because the properties influence greatly the final product's quality and performance. Greece has clay deposits that remain underexploited for artisanal and handicraft applications and imported clays are predominantly used. This study aims to evaluate the suitability of specific clayey raw materials for ceramic applications such as pottery, through characterization and mechanical testing. The research involves granulometric analysis, particle size analysis, and determination of Atterberg limits to assess plasticity. Experimental clay specimens are manufactured and subjected to mechanical strength tests, including flexural, tensile and compression testing, at two different firing temperatures. Additionally, mineralogical characterization is performed on both clayey raw materials and sintered specimens to investigate phase transformations. Particle size analysis and other complementary techniques are employed to further understand the material's behavior. Raw material prospection and sampling were undertaken, in accordance with the data provided from Mineral & Aggregate Resources Division of Greek Ministry of Environment, Energy and Climate Change. The clay samples are sourced from active quarries in Greece, specifically from Central Euboea, Central and Western Macedonia, and Central Greece, as potential material sources for pottery applications. The results will provide critical insights into the clay's applicability in ceramic production, highlighting its structural integrity and performance under different conditions. Additionally, these findings will promote the use of Greek clays in pottery applications.

Introduction

Clay-based ceramics have been extensively used in artistic and functional applications due to their durability and versatility. However, the performance of ceramic products depends on the properties of the clay raw materials. This study focuses on evaluating the suitability of selected clay sources for pottery through a comprehensive characterization approach. The main objective is to determine whether the studied Greek clays have the required mechanical and mineralogical properties for industrial use.

Methodology

The methodology consists of several steps. Initially, granulometric analysis is conducted to determine the textural properties and particle size distribution of the clay samples. Atterberg limits are measured to evaluate plasticity, which are critical for workability in artisanal applications. Then, the selected clay materials are processed into standard experimental specimens, which undergo mechanical strength testing. To study the influence of temperature on material properties, the specimens are fired at two different temperatures. Furthermore, mineralogical characterization using X-ray diffraction (XRD) and other techniques are performed to identify phase transformations occurring before and after firing. Additional particle size analysis and complementary characterization methods provide further insights into the structural and functional suitability of the clay for artisanal pottery applications.

Expected Results and Discussion

This study will reveal critical information regarding the development of clay materials during the ceramic production process. The impact of particle size distribution and mineral composition on mechanical strength is expected to be significant. The results will offer insights into how firing temperature influences phase transformations and overall material performance.

Conclusion

This study will contribute valuable data on the potential application of selected clays in pottery industry. Future work may include further refinement of processing parameters and extended mechanical testing to improve ceramic product development.

Acknowledgements

This study is funded by Hellenic Ministry of Culture under the program titled Study of value chains and materials investigation in cottage industry – craftsmanship.

17th INTERNATIONAL CONGRESS of the Geological Society of Greece

BULLETIN OF THE GEOLOGICAL SOCIETY OF GREECE, SP. PUBL.

EXTENDED ABSTRACT 139

The 2025 seismic crisis reveals a coupled magma feeding system at Santorini and Kolumbo

Jens Karstens[1], Paraskevi Nomikou[2], Marius Isken[3], Michelle Maree Parks[4], Vincent Drouin[4], Emilie E.E. Hooft[5], Thomas R. Walter[3,6], Mahmud Haghshenas Haghighi[7], Dimitris Anastasiou[8] and the research team

(1) GEOMAR Helmholtz Centre for Ocean Research Kiel, Kiel, Germany
(2) National and Kapodistrian University of Athens, Laboratory of Geography and Climatology, Department of Geology and Geoenvironment
(3) GFZ Helmholtz Centre for Geosciences, Potsdam, Germany
(4) Icelandic Meteorological Office, Reykjavík, Iceland
(5) Department of Earth Science, University of Oregon, Eugene, OR, USA
(6) Institute of Geosciences, University of Potsdam, Potsdam, Germany
(7) Institute of Photogrammetry and GeoInformation, Leibniz University Hannover, Hannover, Germany
(8) School of Rural, Surveying and Geoinformatics Engineering, National Technical University of Athens, Zographos, Greece

Abstract

The 2025 volcano-tectonic crisis of Santorini and Kolumbo volcanoes in the Greek Aegean Sea has provided unprecedented insights into the complex, interconnected magmatic systems beneath these neighbouring volcanic centres. Through the integrated analysis of seismological data and geodetic measurements, the migration of magma prior to and during this significant event has been reconstructed. The crisis began with a gradual deformation of the ground within the Santorini caldera from July 2024, with an uplift of about 45-50 mm detected by GNSS and satellite data, accompanied by increased H_2 and CO_2 gas emissions. On 27 January 2025, an intense earthquake swarm initiated 10 km northeast of Santorini, near Kolumbo volcano. The seismic activity continued for a period of over 30 days, during which time the intensity fluctuated. The seismic activity can be subdivided into distinct phases, beginning with deep seismicity (12-18 km) accompanied by strong tremors. This was followed by northward migration of increasingly shallow earthquakes towards Anhydros Island at velocities of approximately 1 km/h. The identification of at least 12 seismic surges, characterised by sharp increases in seismicity rate, magnitude intensification, and concurrent tremor activity, followed by lateral migration of seismic fronts, underscores the complexity of the crisis. A thorough analysis of 180 earthquake moment tensors for events with MW>3.6 revealed a consistent NW-SE-oriented tension axis perpendicular to the earthquake migration path, consistent with normal faulting patterns typical of dike intrusions. Our high-resolution earthquake catalogue, which contains over 28,000 events, shows a segmented, laterally ascending complex dike intrusion characterised by incremental, non-uniform and rapid expansion. Furthermore, periods of dike growth coincided with intense seismicity and large-magnitude earthquakes (MW>5) concentrated at the advancing dike tip. Between surges, when the dike boundary was stationary, seismicity was predominantly lower magnitude (MW 1-3), consistent with gradual pressurisation due to continuous magma inflow. Joint inversion of ground deformation data suggests two primary sources: a volume decrease within a mid-crustal reservoir beneath Kolumbo volcano and a uniform opening along a ~13km long dislocation between Kolumbo and Anhydros, representing the emplacement of a dike. The deflation source has been estimated at a depth of ~7.6 km beneath Kolumbo, with an inferred volume decrease of ~0.08 km³. In contrast, the volume increase in the dike has been calculated at ~0.3 km³. Following the initiation of the dike, there was a rapid increase in the magma inflow rate, which peaked between 4-12 February, with average inflow rates exceeding 200 m³/s, before decreasing to almost zero by 24 February, which is likely to mark the end of the intrusion. The sequential timing of these events – shallow magma chamber inflation at Santorini, followed by dike intrusion into the Anhydros Block with concurrent deflation at Kolumbo – points to coupling between reservoirs of both volcanoes. The interaction between the reservoirs likely occured through crustal stress transfer or pressure changes within the fluid plumbing system at depth, while there is no evidence for direct

connection between the shallow magma reservoirs.

Acknowledgements
The authors would like to acknowledge the research team: Eleonora Rivalta, Gareth J. Crutchley, Simone Cesca, Sebastian Hainzl, Joachim Saul, Kostas Raptakis, Nikolai M. Shapiro, Jannes Münchmeyer, Quentin Higueret, Jean Soubestre, Florent Brenguier, Rebeckah S. Hufstetler, Kaisa R. Autumn, Maria Tsakiri, Dietrich Lange, Heidrun Kopp, Morelia Urlaub, María Blanch Jover, Jonas Preine, Christian Hübscher, Mahdi Motagh, Daniel Müller, Torsten Dahm, Christian Berndt for their contribution.

17th INTERNATIONAL CONGRESS of the Geological Society of Greece

BULLETIN OF THE GEOLOGICAL SOCIETY OF GREECE, SP. PUBL.

EXTENDED ABSTRACT 140

The role of painting as historical evidence of relative sea-level change: a review

Karymbali Th.[1]
(1) School of Humanities, Hellenic Open University, Patras, Greece, theodorak2000@gmail.com

Background

Certain artworks can provide important perspectives on historical environmental and climate changes and may be used by scientists as proxies in measuring such changes. The extent to which they can be utilized depends greatly on the nature of the artwork, ranging from abstract and interpretive to strikingly precise, and the specific climate phenomenon being studied (Smithers, 2011). For instance, the variety of animals depicted in prehistoric cave and rock art offers clues about the prevailing climate at the time, though such interpretations must account for critical limitations. Pieter Bruegel's paintings, while inconclusive, have been linked to evidence of the onset of the Little Ice Age (Mann, 2002), while Mid-19th-century depictions of glaciers serve as useful benchmarks for assessing modern glacial retreat. Additionally, analyses of sunsets in various artworks have provided precise data on the atmospheric effects of volcanic eruptions (Zerefos *et al*., 2007).

When studying mean sea-level fluctuations, geomorphological data are valuable for identifying long-term rates of relative sea-level change, while historical data and records can be used to study local sea-level variations over recent centuries. By identifying and locating these indicators and determining their age and elevation relative to present-day sea-level, changes in relative sea-level can be established.

Geomorphological sea-level indicators can have the form of erosional landforms (such as marine notches, sea caves, arches, shore platforms, and marine terraces) or depositional landforms (such as beachrocks, beach ridges, tidal flats, and coral formations) (Vacchi, 2016). When these erosional or depositional features become inactive (fossilized) and appear above or below the current level at which similar landforms are currently forming, they provide evidence of sea-level changes since the time of their formation. In addition, various organisms (corals, algae, various types of shells, worms etc.) or their remnants that, when alive, inhabited known specific tidal levels, can now be found fossilized at different elevations. These biological sea-level indicators reflect changes in sea level that occurred after the organisms' death. The fossils mark the location of the ancient shoreline, representing the time when these organisms lived (Karymbalis, 2010). Sea-level indicators may also include archaeological evidence, such as ancient coastal cities or harbor structures that are now situated above or below the current sea-level (Kolaiti *et al.*, 2024). These findings demonstrate that during their period of peak activity, sea-level was at a different position than it is today.

Historical data and records often serve as valuable indicators of more recent sea-level changes. These include written documentary evidence, as well as old tidal gauge measurements, which span over 100 years but are available for only a few regions worldwide (such as northwestern France). Additionally, old high precision paintings that accurately depict coastal landscapes, whether natural or urban, can serve as historic sea-level indicators, providing valuable insights into the sea-level's position at the time they were created.

An example of using paintings to study changes in relative sea-level and the geomorphological evolution of a coastal area is the work by Mattei *et al*. (2020). Among the various geomorphological and historical elements they interpreted to reconstruct the relative sea-level variations and associated morpho-evolutive trends of the Naples coast since the mid-Holocene, they utilized five paintings created between 1790 and 1836 by different artists. However, the most notable example of how paintings can be successfully used to reconstruct recent relative sea-level changes is Venice. For centuries, Venice has long wrestled with the effects of subsidence and the rising sea-level, well before the onset of the industrial era and has abundant evidence of rising sea-level and historical evdence of past high waters. High precision 18th century paintings have been systematically used by Camuffo *et al*., 2017, Camuffo and Sturaro (2003), and Camuffo (2001; 2021)to identify water levels in Venice in the period before instrumental records were kept.

This review paper explores how sea-level evidence on buildings in Venice, as well as architectural features captured in paintings, serve as powerful witnesses to geological and climatic processes. These indicators reveal the recent rise in sea-level driven by both global eustatic sea-level rise and local land subsidence caused by natural and human forces. It primarily focuses on how the height of algae line on palaces, accurately depicted by two painters, has been used as a sea-level proxy over the last three centuries, demonstrating how art and geomorphology can collaborate in reconstructing past sea-level fluctuation.

Methodology

The methodology for this study is based on a comprehensive review of existing literature on the topic. A systematic approach was employed to identify key studies addressing long-term land subsidence and relative sea-lever rise, as well as the use of historical evidence depicted on paintings in Venice. The literature search led to a series of papers and book chapters on the

topic published mostly by Dario Camuffo and his co-authors who have been exhaustively studying these types of historical sea-level indicators in Venice over the past few decades.

Venice

Venice is located in northeastern Italy and is the capital of the Veneto region (Figure 1). It rests atop a network of 127 islands, interconnected by 472 bridges and divided by canals and open waterways. These islands are nestled within the shallow Venice Lagoon, a sheltered bay located between the mouths of the Po and Piave rivers. The lagoon has been a hub of human activity since pre-historic times, with early inhabitants relying on its rich resources for fishing and hunting. By the Neolithic period, the area was already settled, and by the Bronze Age, significant communities, such as Altinum, had emerged. From its very origins, Venice's identity has been inseparable from water. The lagoon offered natural protection against invaders and served as a vital lifeline for its people. Yet, life in this extraordinary setting has always demanded resilience, as Venetians have faced and adapted to the challenges of land subsidence and shifting sea-level.

Carminati *et al*. (2003) assessed a long-term subsidence rate of 0.7–1.0 mm/yr for the greater Venice area, which aligns closely with the slightly lower rate of 0.5 mm/yr estimated by Kent *et al*. (2002) for the past 2.6 million years. The geological-scale subsidence affecting Venice is primarily driven by the subduction of the Adriatic plate beneath the Apennines (Carminati and Di Donato, 1999), as the city lies at the northeastern edge of the Po Plain, which is the foreland basin for two fold-and-thrust belts: the Northern Apennines and the Southern Alps (Cuffaro *et al*., 2010). A natural subsidence rate of 0.45±0.09 mm/yr has also been calculated for the last 124 ka (Rovere *et al*., 2024), consistent with all the above-mentioned long-term rates. However, it is important to note that subsidence rates in regions as geologically complex as the Venice lagoon and its surrounding coastal plain can vary significantly over space and time. Holocene subsidence rates appear to be greater than those observed over extended geological periods. Tosi *et al*. (2009) offer a possible explanation for this difference, suggesting that sediment compaction could be a contributing factor. They propose that this process significantly impacts Holocene sediments, whereas its effect on older sediments is minimal.

Figure 1. Location of Venice (Source: Google Earth).

Paintings as historical relative sea level change indicator

While geological data are essential for determining long-term rates of relative sea-level change, accounting for eustatic, isostatic, and tectonic components, understanding localized sea-level fluctuations over recent centuries is particularly critical for a city like Venice. This period spans both the pre-industrial and post-industrial eras, the latter marked by accelerated ice melt and rising sea-level driven by human-induced greenhouse gas emissions (Fox-Kemper *et al*. 2021). For the past century, modern tools such as tide gauges and satellite altimetry have provided accurate sea-level measurements. Venice presents a unique case study as its centuries-old architecture, constructed in close proximity to the water's edge, combined with artistic depictions of the city by painters, allows the reconstruction of sea-level changes dating back as far as 1300 CE (Camuffo, 2021). This rich historical and cultural record offers insights unavailable in most other coastal locations.

The contributions of the paintings by two prominent Venetian painters, Antonio Canal (better known as Canaletto, 1697–1768) and Bernardo Bellotto (1722–1780) were of great importance in sea-level change reconstruction (Camuffo, 2001). Born in Venice on October 18, 1697, Canaletto grew up in a family of artists. He initially worked as a theatrical scene painter but eventually embraced a new artistic direction that shaped his legacy: veduta, or "view painting." This genre, which originated in the 17th century, focuses on exceptionally detailed portrayals of cityscapes and urban landmarks (Kowalczyk, 2018). Drawn to this style, Canaletto turned his attention to capturing the essence of daily life in Venice through his meticulously crafted cityscapes and architectural views often referred to as "veduta". In his paintings, Venice is portrayed as a grand theatrical production, with the

Grand Canal serving as the stage, the buildings forming the curtains, and the intricate architecture creating the backdrop of the scenery (Kowalczyk, 2018). Bernardo Bellotto (1721–1780) was a nephew and pupil of Canaletto known also for his stunning "veduta" painting. He even signed some of his works as "Bernardo Canaletto", capitalizing on his uncle's fame. However, Bellotto developed his own distinct style, marked by highly detailed and often large-scale depictions of cities, dramatic lighting, and a cooler palette (Kowalczyk, 2016).

To discuss the role of paintings as indicators of sea-level change, it is essential to understand the concept of the "Comon Mark" ("CM") or "Marine Common Level" in sea-level reconstruction studies, both generally and specifically in the context of Venice. The "CM" refers to reference benchmarks used to measure and monitor sea-level changes. These benchmarks might include tidal markers, which are physical markers set at specific locations that serve as references for mean-sea level, tidal datums, or other standardized elevations for data comparison (Rovere *et al*., 2024). Essentially, common marks agreed-upon reference points or datasets that allow for consistent comparisons across different regions or time periods. The role of the "CM" in sea-level change studies is crucial because it provides consistency across locations. A shared CM or "common level" ensures that measurements are comparable on a global scale. Additionally, using standard baselines allows researchers to track global sea-level rise and its impacts on coastal regions making "CM"s indispensable for understanding long-term trends.

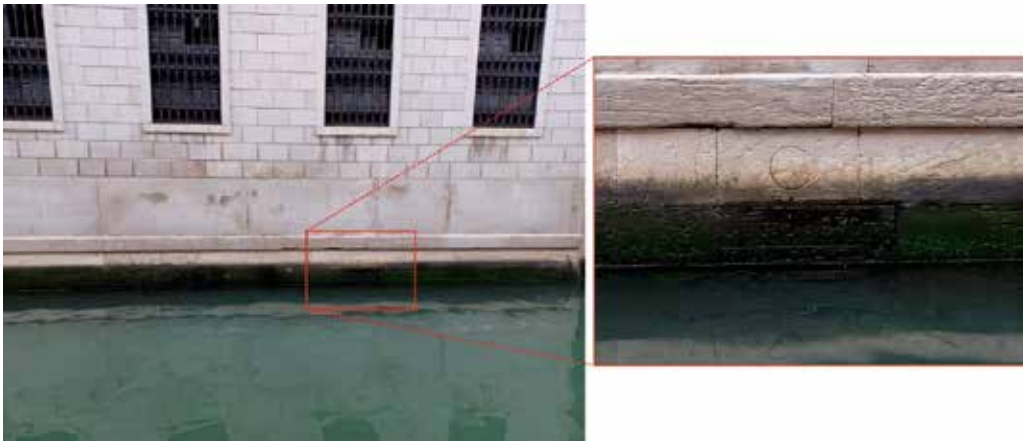

Figure 2. Photo showing the present brown-green microorganisms mark on a building wall facing a canal and the letter "C" (the official sea-level reference engraved when the benchmark was made in 970).

In the case of Venice, the "CM" refers to the distinctive dark green-brown belt formed by photic algae that grows on buildings, walkways, and bridges throughout the city (Rovere *et al*., 2024). This belt's elevation is slightly above the high tide level, influenced by the standing waves generated by boats during calm days in the lagoon. As noted by Camuffo (2023), the ancient Venetians sometimes formalized this marker by engraving it onto walls as "CM" or simply "C", designating it as an official sea-level reference at the time the benchmark was made (Figure 2). The use of the "CM" as a benchmark for water level in Venice has been well-documented in historical sources, including a 16th century book by Cornaro, (1560) and the writings of Temanza (1761).

Canaletto and Bellotto achieved an almost photographic precision in their depictions of urban landscapes, faithfully reproducing buildings down to the smallest details, a realism made possible by their use of the camera obscura (Camuffo and Sturaro, 2003). The camera obscura, an early precursor to the modern camera, functions by allowing a beam of light to pass through a lens or small opening, it is then reflected by a mirror or prism and subsequently projected onto a glass surface (Figure 3a). The painter would position a canvas or sheet of paper over the glass surface to trace the outlines of the projected image, creating a highly detailed, almost "photographic" rendering. Although the overall proportions of the scene might not always be maintained, Cannaleto and Bellotto meticulously reproduced intricate details, including the "CM" on buildings. This technique enabled painters to achieve remarkable detail and realism in their cityscapes. Canaletto's camera obscura, is kept at the Correr Museum in Venice (Figure 3b). The accuracy of detail in Canaletto and Bellotto's works can be tested by scaling and comparing elements across multiple paintings of the same building, all created using a camera obscura. Although these paintings are often regarded as copies of an original, the varied patterns of minor discrepancies suggest that the two artists likely revisited the site at different times to produce fresh sketches of the same structure. The precision in depicting even the smallest details highlights that their paintings are faithful, high-quality representations of the real world rather than imaginative or fictional compositions.

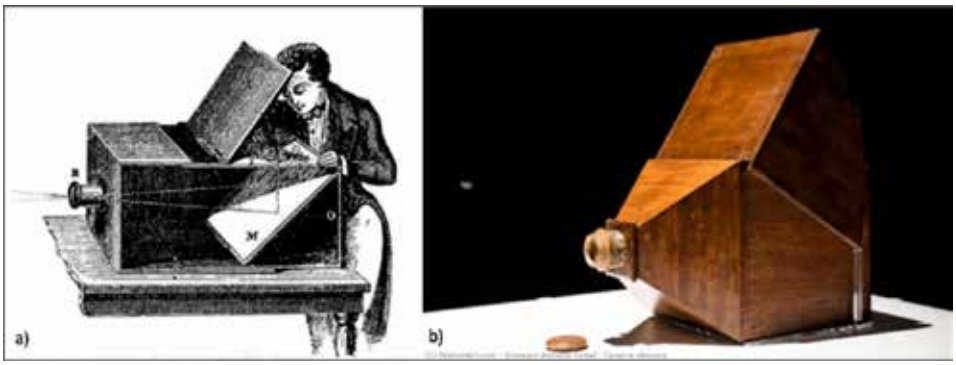

Figure 3. (a) An artist sketching from life using a 19th century camera obscura. The device includes: B (lens), M (mirror), and O (the path of light if unobstructed by the mirror). The artist used thin tracing paper to outline the image, then transferred it onto canvas, board or paper to complete the drawing. (Source: Wikipedia Commons) (b) A camera obscura made, or perhaps simply owned, by Canaletto, as revealed by the inscription.

From the above it is clear that it becomes possible to reconstruct the sea-level at the time the painting was created. Although the exact tidal stage during the painting's execution cannot be determined, both Canaletto and Bellotto incorporated the "CM" into their works, providing a reliable reference point. The process begins by identifying the precise location of the "CM" in the painting, relative to recognizable architectural features. Next, the site is visited, typically by boat, to locate the building, where the "CM" (level reached by algae) from the painting is compared to the current algae line on the structure. The difference between the two levels indicates the rise in relative sea-level from the time the painting was made to the present. Before arriving at a final estimate, several adjustments must be made. Key factors, such as the difference in wave patterns created by motorboats today compared to those caused by the rowing and sailing vessels of the 18th century, as well as the amplification of tidal wave due to dynamic effects, must be carefully taken into consideration (Rovere *et al*., 2024). The analysis of eleven paintings of Canaletto and Bellotto (Figure 4) revealed that the "CM" has risen on average by 69±11 cm since the early 18th century (Camuffo and Sturaro, 2003) as shown in Figure 5a.

Figure 4. Four of the paintings of Canaletto and Bellotto that were used as historical relative sea level change indicator (a) "The Punta della Dogana" by Canaletto (1727); (b) "View of the Grand Canal at San Stae" by B. Bellotto (1740); (c) "The Grand Canal, Venice, Looking East from the Palazzo Flangini to the Palazzo Venramin Calergi" by B. Bellotto (1741); (d) "Grand Canal From the Campo Santa Sofia Towards the Rialto Bridge" by Canaletto (1730-31). (Source: WikiArt, Visual Art Encyclopedia).

Beyond changes in the "CM" elevation shown in paintings, another architectural feature that can act as a proxy for relative sea level is the positioning of steps in front of residential buildings or leading to canal walkways. Camuffo *et al*. (2017) explored this proxy, grounded in the principle that stairs were designed for practical use—allowing people to descend from buildings into boats, and vice versa. To facilitate this, the lowest step was typically aligned with the boat's gunwale (side level), ensuring it was free of algae, meaning it was positioned slightly above the "CM".
By integrating evidence from paintings, staircases, and historical written documents detailing changes in "CM" elevation relative to known architectural features, Camuffo *et al*. (2017) reconstructed trend in relative sea-level from 1300 to around 1800 CE. Camuffo *et al*. (2017) and Camuffo (2021; 2022a) identified an exponential rise in relative sea-level from 1350 to the present. This acceleration in sea-level rise is also exponential, indicating the importance of long-term processes (such as melting continental glacier, isostatic adjustments, and tectonic movements) alongside climate change. While the precise mechanisms driving this exponential trend remain to be fully understood, they likely involve a complex interaction of Glacial Isostatic Adjustment, historical subduction, and post-industrial sea-level rise. Over the entire period from 1350 to 2016 CE, the average local sea-level change is estimated at 1.9±0.1 mm/yr. A key unresolved issue lies in the significant discrepancies between historical records and geological data reported by Vacchi *et al*. (2016). These differences suggest the possibility of substantial pre-industrial sea-level fluctuations that remain unexplained. Bridging the gap between geological and historical relative sea-level data is essential and represents a promising direction for future research in understanding long-term sea-level dynamics.

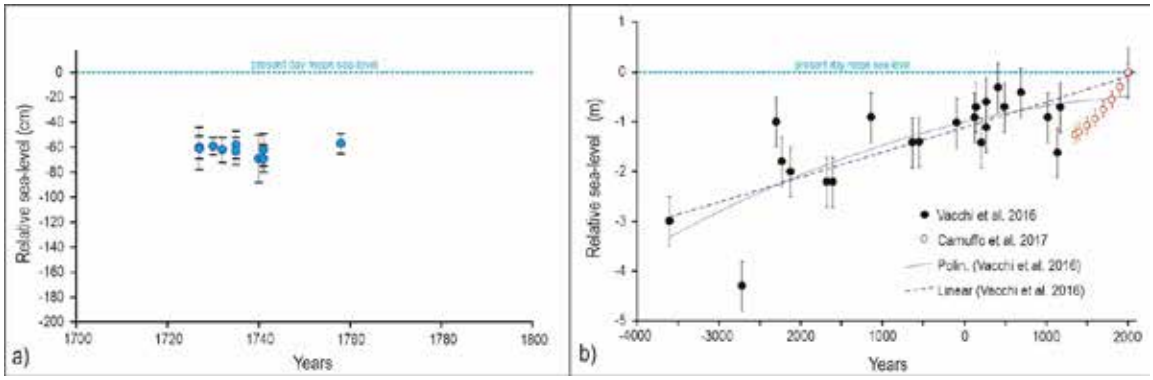

Figure 5. Data on relative sea level (RSL) changes in Venice through multiple sources. (a) The graph illustrates RSL trends based on estimations derived from the paintings of Canaletto and Bellotto (white dots with error bars, covering 1727–1758). The RSL values from the paintings were inferred by comparing the algae belt's position depicted in the artwork to its present-day level; (b) a long-term reconstruction of relative sea-level rise over the past 6000 years. Black dots represent data from natural proxies as compiled in Vacchi *et al*. (2016), while red circles indicate sea-level estimates reconstructed by Camuffo et al. (2017). (Source: Camuffo *et al*. (2022b).

In the context of climate change, the study area is expected to face significant challenges due to both short- and long-term sea-level rise (Tosi et al., 2002; Zanchettin et al., 2021; Lionello et al., 2021).
Taking into account the spatial distribution of vertical land movement (1–3 mm/year of subsidence, with peak values reaching 7 mm/year) and tide gauge data, projections indicate that by 2150, more than 112 km² could be at risk of flooding under the SSP1-2.6 low-emission scenario, with this figure increasing to 139 km² under the SSP5-8.5 high-emission scenario. During extreme high-water events—driven by the combined effects of astronomical tides, seiches, and atmospheric forcing—the relative sea-level rise (RSLR) in 2150 could temporarily reach up to 3.47 m (Andizei et al., 2024, 2025). These findings emphasize the urgent need for local communities to strengthen flood resilience strategies to mitigate the projected impacts of RSLR by 2150, particularly in the UNESCO-listed city of Venice and its ecologically significant lagoon (Alberti et al., 2023; Andizei et al., 2024).

Closing Remarks

Painting and other forms of art have emerged as significant proxies for understanding climate change impacts including sea-level rise. Venice, with its continuous habitation and unique coastal environment characterized by significant interaction between water and buildings, stands out as a one-of-a-kind region globally where painting can play a pivotal role in studying sea-level changes. The distinctive technique and faithful depiction of the city's urban landscape by painters such as Canaletto and Bellotto have significantly contributed to the investigation of relative sea level changes since the early 18th century, making Venice one of the finest examples of the collaboration between

painting and geomorphology, yielding impressive results. While paintings can help reconstruct historical sea-levels from the time they were created, several critical factors that further complicating accurate interpretations must be taken into account. In the case of Venice such issues include significant differences in wave patterns generated by modern motorboats compared to those produced by the rowing and sailing vessels of the 18th century, as well as the amplification of tidal wave due to dynamic effects.

The integration of artistic expression with scientific data allows for a unique communication of climate change, particularly in relation to sea-level rise. Beyond utilizing works of art to study changes in relative sea-level, art can also motivate audiences to consider the implications of climate change more seriously. Artists often depict landscapes threatened by rising waters, creating a visual narrative that underscores the urgency of climate change and the need for a sustainable future.

References

Alberti, T., Anzidei, M., Faranda, D., Vecchio, A., Favaro, M., Papa, A., 2023. Dynamical diagnostic of extreme events in Venice lagoon and their mitigation with the MoSE. Sci. Rep., 13, 10475.

Anzidei, M., Tolomei, C., Trippanera, D., Alberti, T., Bosman, A., Brunori, C.A., Serpelloni, E., Vecchio, A., Falciano, A., Deli, G., 2025. Multi-temporal Relative Sea Level Rise Scenarios up to 2150 for the Venice Lagoon (Italy). Remote Sens., 17, 820.

Anzidei, M., Alberti, T., Vecchio, A., Loizidou, X., Orthodoxou, D., Serpelloni, E., Falciano, A., Ferrari, C., 2024. Sea level rise and extreme events along the Mediterranean coasts: the case of Venice and the awareness of local population, stakeholders and policy makers. Rendiconti Lince Sci. Fis. Nat., 35, 359–370

Camuffo, D., 2023. The Treatise on Waters by Cornaro (1560) and a quantitative assessment of the historical sea surges “Acqua Alta” in Venice. Climatic Change 176, 18.

Camuffo, D., 2022a. A discussion on sea level rise, rate ad acceleration. Venice as a case study. Environmental Earth Sciences, 81, 349.

Camuffo, D., 2022b. Historical Documents as Proxy Data in Venice and Its Marine Environment. Oxford Research Encyclopedia of Climate Science. Retrieved 31 Jan. 2025, Historical Documents as Proxy Data in Venice and Its Marine Environment.

Camuffo, D., 2021. Four centuries of documentary sources concerning the sea level rise in Venice. Climatic Change, 167, 54.

Camuffo, D., 2001. Canaletto’s paintings open a new window on the relative sea level rise in Venice. Journal of Cultural Heritage, 4, 227–281.

Camuffo, D., Sturaro, G., 2003. Sixty-cm submersion of Venice discovered thanks to Canaletto’s paintings. Climatic Change, 58(3), 333-343.

Carminati, E., Doglioni, C., Scrocca, D., 2003. Apennines subduction-related subsidence of Venice (Italy). Geophysical Research Letters, 30(13), 1717.

Carminati, E., Donato, G.D., 1999. Separating natural and anthropogenic vertical movements in fast subsiding areas: The Po plain (N. Italy) case. Geophysical Research Letters, 26(15), 2291-2294.

Cornaro, L., 1560 Trattato di Acque, Perchacino, Padua.

Cuffaro, M., Riguzzi, F., Scrocca, D. Antonioli, F., Carminati, E., Livani, M., Doglioni, C., 2010. On the geodynamics of the northern Adriatic plate. Rendiconti. Fis. Acc. Lincei 21(Suppl 1), 253–279.

Fox-Kemper, B., Hewitt, H.T., Xiao, C., Aðalgeirsdóttir, G., Drijfhout, S.S., Edwards, T.L., Golledge, N.R., Hemer, M., Kopp, R.E., Krinner, G., Mix, A., Notz, D., Nowicki, S., Nurhati, I.S., Ruiz, L., Sallée, J.-B., Slangen, A.B.A., Yu, Y., 2021: Ocean, Cryosphere and Sea Level Change. In: Masson-Delmotte, V., Zhai, P., Pirani, A., Connors, S.L., Péan, C., Berger, S., Caud, N., Chen, Y., Goldfarb, L., Gomis, M.I., Huang, M., Leitzell, K., Lonnoy, E., Matthews, J.B.R., Maycock, T.K., Waterfield, T., Yelekçi, O., Yu, R., Zhou, B. (Eds.), Climate Change 2021: The Physical Science Basis. Contribution of Working Group I to the Sixth Assessment Report of the Intergovernmental Panel on Climate Change. Cambridge University Press, Cambridge, United Kingdom and New York, NY, USA, 1211–1362.

Karymbalis, E., 2010. Coastal Geomorphology, ION Publishing Group, p. 240.

Kent, D.V., Rio, D., Massari, F., Kukla, G., Lanci, L., 2002. Emergence of Venice during the Pleistocene. Quaternary Science Reviews, 21(14-15), 1719-1727.

Kolaiti, E., Simosi, A., Mourtzas, N., 2024. Archaeological sea level indicators in the Argolic Gulf since the 14th century AD: Bourtzi Fortress, Myloi Lernas and Mylos Beach in Agios Andreas. In: M. Xanthopoulou et al. (Eds), Archaeological Work in the Peloponnese 3, Proceedings of the 3rd International Scientific Meeting AWOP3, Kalamata, 2-5 June 2021, University of the Peloponnese, Kalamata, 837-853.

Kowalczyk, B.A., 2018. Canaletto1697-1768. p. 256.

Kowalczyk, B.A., 2016. Bellotto e Canaletto Lo stupore e la luce. p. 304.

Lionello, P., Nicholls, R.J., Umgiesser, G., Zanchettin, D., 2021. Venice Flooding and Sea Level: Past Evolution, Present Issues, and Future Projections (Introduction to the Special Issue). Nat. Hazards Earth Syst. Sci., 21, 2633–2641.

Mann, M.E., 2002. Little Ice Age, in: MacCracken, M.C., Perry, J.S. (Eds.), Encyclopedia of Global Environmental Change, Vol 1: The Earth system: physical and chemical dimensions of global environmental change, 504-509.

Mattei, G., Aucelli, P.P., Caporizzo, C., Rizzo, A., Pappone, G., 2020. New geomorphological and historical elements on morpho-evolutive trends and relative sea-level changes of Naples coast in the last 6000 years. Water, 12(9), 2651.

Rovere, A., Camuffo, D., Cerrone, C., 2024. Living on the water towards 2100. Fieldtric guide. Ca´ Foscari University of Venice. p. 26.

Smithers, S., 2011. Sea-level indicators. in: Hopley, D. (Ed.), Encyclopedia of modern coral reefs. Encyclopedia of earth sciences series. Springer, 978–991.

Temanza, T. 1761. Dissertazione sopra l'antichissimo territorio di Sant'Ilario nella diocesi di Olivolo. Pasquali, Venice.

Tosi, L., Teatini, P., Carbognin, L., Brancolini, G., 2009. Using high resolution data to reveal depth-dependent mechanisms that drive land subsidence: The Venice coast, Italy. Tectonophysics, 474(1-2), 271-284.

Tosi, L., Carbognin, L., Teatini, P., Strozzi, T., Wegmüller, U., 2002. Evidence of the present relative land stability of Venice, Italy, from land, sea, and space observations. Geophys. Res. Lett., 29, 3-1–3-4

Vacchi, M., Marriner, N., Morhange, C., Spada, G., Fontana, A., Rovere, A., 2016. Multiproxy assessment of Holocene relative sea-level changes in the western Mediterranean: Sea-level variability and improvements in the definition of the isostatic signal. Earth-Science Reviews, 155, 172-197.

Zanchettin, D., Bruni, S., Raicich, F., Lionello, P., Adloff, F., Androsov, A., Antonioli, F., Artale, V., Carminati, E., Ferrarin, C., et al., 2021. Sea-level rise in Venice: historic and future trends (review article). Nat. Hazards Earth Syst. Sci., 21, 2643–2678.

Zerefos, C.S., Gerogiannis, V.T., Balis, D., Zerefos, S.C., Kazantzidis, A., 2007. Atmospheric effects of volcanic eruptions as seen by famous artists and depicted in their paintings. Atmospheric Chemistry and Physics, 7, 4027–4042.

17th INTERNATIONAL CONGRESS of the Geological Society of Greece

BULLETIN OF THE GEOLOGICAL SOCIETY OF GREECE, SP. PUBL.

EXTENDED ABSTRACT 141

Challenges and Opportunities in the AI Era: Promoting Earth Science Education for Deaf and Hard of Hearing Students

Katheri M.[1], Koumoutsakou O.[1], Antonarakou A.[1]

(1) Department of Geology and Geoenvironment, Kapodistrian University of Athens, Ilisia, Greece, mar.katheri@hotmail.com

Introduction / Background

The formal education of Deaf and Hard of Hearing (DHH) students has a long and often controversial history, particularly in Earth Sciences. Despite the legal guarantee of equal education for DHH students, its practical implementation often lacks inclusivity. Many students, while physically present in the classroom, are academically and socially excluded due to deficiencies in the education system (Howerton-Fox & Falk, 2019), though these deficiencies may vary by region or institution. Considering inclusion, accessibility, and the greater representation of persons with disabilities in science and engineering fields (NCSES, 2023), including Earth Sciences, the need for redesigning Earth Science teaching at all educational levels becomes evident, especially in the new AI era.

The Challenges of DHH Students in Geosciences

DHH students are often discouraged from participating in Earth Science due to practical constraints and social biases (Connors, 2023). Fieldwork, which is a cornerstone of Geosciences (Whitmeyer & Mogk, 2009), presents significant difficulties. Challenges such as outdoor communication difficulties, insufficient educational materials, and the absence of sign language for specialized terms create significant barriers to equal participation.

At the same time, inclusive pedagogical approaches often omit deafness as a key factor, ignoring the need for tailored solutions. The responsibility for accommodation is often placed on DHH students, burdening them with additional stress and challenges (Carabajal *et al.*, 2017). The challenges faced by DHH students considering intersectionality (e.g., gender, ethnicity, socioeconomic status) may compound these challenges.

Assistive Technologies and Innovations

Today, technology is providing new opportunities to support DHH students. Tools such as Communication Access Real-time Translation (CART) and sign language interpreters improve communication (NAD, 2023). However, these tools often have limitations, such as incomplete coverage of specialized terms in Earth Sciences. Newer technologies like real-time AI-based sign language generation, tactile feedback devices, virtual and augmented reality education platforms, and AI tools and datasets reflect recent innovations (Kouremenos & Ntalianis, 2025; Hossain, 2024; Ulrich et al., 2024).

In addition, initiatives such as the Signing Earth Science Dictionary (SESD) offer access to approximately 750 Earth Science terms for DHH students (Vesel & Hurdich, 2014). Similar efforts are being extended to British Sign Language, with the addition of terms related to biodiversity and ecology. Thus, maintaining and expanding such dictionaries and similar efforts to address evolving terminology remains a challenge.

Innovative Pedagogical Methods

Virtual technologies provide unique teaching opportunities in Earth Sciences. Research projects, such as the use of virtual worlds, have demonstrated that virtual fieldwork can effectively simulate the experience of outdoor teaching (Allison & Miller, 2012) especially for students who might not have access to physical field experiences due to disabilities or other constraints. Moreover, devices such as the deformational sandbox demonstrate that hands-on learning can be effectively adapted for DHH students, enhancing their understanding of complex geological processes (Kahn *et al.,* 2013).

Fieldwork and Inclusive Education

Fieldwork remains a critical area for adaptation to support DHH students. Despite these barriers, educators have developed practices to improve accessibility in field experiences. Virtual field applications, while not a full replacement for the experience, offer significant support and learning opportunities (Guillaume *et al.,* 2023).

The Role of Inclusion in the Earth Sciences

Inclusion in geoscience is not only about DHH students' access to education but also about creating a more diverse and welcoming science environment. Research shows that the presence of minority faculty encourages students to remain in the field, fostering a sense of community (Dutt, 2020). Peer support networks, accessibility policies, and inclusive course design, also play a significant role in retention and fostering community.

Conclusions and Perspectives

Addressing the challenges DHH students face in geosciences requires a multi-dimensional approach. From the development of assistive technologies and customized pedagogies to the creation of inclusive learning environments, progress in this area is essential. An education system emphasizing intellectual abilities over physical limitations can unlock the full potential of DHH individuals and enrich Earth Sciences with diverse perspectives and ideas. In addition, wider social and professional barriers, including funding challenges, recruitment biases, and the need for more mentoring programs need to be taken seriously.

References

Allison, C. and Miller, A. (2012). Open virtual worlds for open learning. Higher Education Academy St. Andrews, UK.

Carabajal, I.G., Marshall, A.M., Atchison, C.L. (2017). A synthesis of instructional strategies in geoscience education literature that address barriers to inclusion for students with disabilities. Journal of Geoscience Education 65(4), 531–541, https://doi.org/10.5408/16-211.1.

Connors, I.C. (2023). Racial diversity in the Geosciences: Engaging community cultural wealth for success. J of Women & Minor. in Sc. and Eng. 29(2), 1-23.

Dutt, K. (2020). Race and racism in the geosciences. Nature Geoscience 13(1), 2–3, https://doi.org/10.1038/s41561-019-0519-z.

Guillaume, L., Laurent, V., Genge, M.J. (2023). Immersive and interactive three-dimensional virtual fieldwork: Assessing the student learning experience and value to improve inclusivity of geosciences degrees. Journal of Geoscience Education 71(4), 462–475, https://doi.org/10.1080/10899995.2023.2200361.

Hossain, S. (2024). Human AI Collaborative Framework to Aid in Computer Science Technical Sign Generation: Towards Enhancing Deaf and Hard Of Hearing Participation in Technical Higher Education. Thesis. Arizona State University.

Kahn, S., Feldman, A., Cooke, M.L. (2013). Signs of Autonomy: Facilitating Independence and Inquiry. Journal of Science Education for Students with Disabilities 17(1), 2.

Kouremenos, D., & Ntalianis, K. (2025). GLaM-Sign: Greek Language Multimodal Lip Reading with Integrated Sign Language Accessibility. https://arxiv.org/pdf/2501.05213 (retrieved 21/01/2025) https://doi.org/10.5281/zenodo.14610495

NAD, 2023. Position Statement on Inclusion. National Association of the Deaf, https://www.nad.org/about-us/positionstatements/position-statement-on-inclusion.

NCSES (2023). Diversity and STEM: Women, Minorities, and Persons with Disabilities. National Center for Science and Engineering Statistics. Special Report NSF 23-315, Alexandria, VA: National Science Foundation, https://ncses.nsf.gov/wmpd.

Ulrich, L., Carmassi, G., Garelli, P., Lo Presti, G., Ramondetti, G., Marullo, G., Innocente, C., Vezzetti, E. (2024). SIGNIFY: Leveraging Machine Learning and Gesture Recognition for Sign Language Teaching Through a Serious Game. *Future Internet* **2024**, *16*, 447. https://doi.org/10.3390/fi16120447

Vesel, J. and Hurdich, J. (2014). Signing Earth Science: Accommodations for Students Who Are Deaf or Hard of Hearing and Whose First Language Is Sign. In: Proceedings of American Geophysical Union, Fall Meeting 2014, abstract id: ED31I-04.

Whitmeyer, S. and Mogk, D. (2009). Geoscience field education: A recent resurgence. Transactions American Geophysical Union, Eos 90(43), 385–386, https://doi.org/10.1029/2009EO430001.

17th INTERNATIONAL CONGRESS of the Geological Society of Greece

BULLETIN OF THE GEOLOGICAL SOCIETY OF GREECE, SP. PUBL.

EXTENDED ABSTRACT 142

Preliminary results of displacements from the recent seismic and volcanic crisis in the Santorini Island complex, Greece

Katsafados I.[1,2], Anastasiou D.[2], Paraskevas M.[1,2], Tsakiri M.[2], Nomikou P.[3], Synolakis C.[4]
(1) Hellenic Military Geographical Service, john.katsafados@gmail.com
(2) National Technical University of Athens
(3) National and Kapodistrian University of Athens
(4)University of Southern California

Research Highlights
GNSS campaign measurements conducted in February 2025 reveal measurable displacements across the Santorini caldera, with patterns consistent with low-level magmatic deflation. Comparison with 2012 benchmark data confirms ongoing deformation and underscores both the value and the limitations of campaign-based observations relative to continuous GNSS monitoring.

Introduction

The Santorini Island complex, located in the southern Aegean Sea, is one of the most active volcanic regions in the Eastern Mediterranean. It forms part of the Hellenic Volcanic Arc and comprises several islands, including Thera (Santorini), Therasia, and Nea Kameni, which collectively outline a partially submerged caldera formed during the catastrophic Minoan eruption around 1600 BCE (Friedrich et al., 2006; Druitt et al., 1999). Volcanic activity in the region is driven by the subduction of the African plate beneath the Eurasian plate, resulting in both tectonic and magmatic processes that have shaped the morphology and evolution of the caldera (Nomikou et al., 2014; Pyle & Elliott, 2006).

In recent years, the Santorini complex has experienced a period of renewed geophysical unrest, marked by increased seismic activity, observed ground displacements, and subtle geochemical anomalies (Parks et al., 2012; Bagnardi et al., 2013). This ongoing activity—reminiscent of the 2011–2012 unrest episode—has raised concerns about the potential reactivation of the volcanic system. Early detection and monitoring of ground deformation are therefore essential for understanding subsurface processes and assessing potential volcanic hazards (Newhall et al., 2000).

This study presents preliminary results of ground displacements associated with the most recent seismic and volcanic activity in the Santorini Island complex. Our analysis is based on a combination of continuous GNSS (cGNSS) data from permanent stations established and maintained by various Institute, Universities and private companies and measurements from GNSS campaign surveys conducted at selected pillars of the National Triangulation Network of Greece, established and maintained by the Hellenic Military Geographical Service, across the island complex. By comparing recent observations with historical GNSS datasets, we detect and quantify ground deformation patterns related to the ongoing unrest. The aim is to identify spatial trends, evaluate the magnitude and direction of surface displacements, and explore possible links to underlying volcanic and tectonic processes. These results contribute to a better understanding of Santorini's geodynamic behavior and provide valuable input for hazard monitoring and risk assessment in the region.

Previous Measurements (2011–2012 Unrest)

During the period of increased volcanic unrest in the Santorini Island complex between 2011 and 2012, an extensive geodetic campaign was conducted to detect and quantify ground deformation. The network consisted of ten permanent GNSS stations established progressively across the islands, with dense spatial coverage especially after mid-2011 in response to the signs of volcanic reactivation. Key stations were operated by several institutions including the Dionysos Satellite Observatory of the NTUA, the University of Patras, the University of Oxford, UNAVCO, and the University of Athens. To enhance spatial resolution, the permanent network was supplemented by 19 non-permanent (campaign) stations, measured during two epochs: the first in September 2011 and the second between January and early October 2012. These campaigns allowed for the detection of short-term displacements by comparing coordinates between the two time periods. GNSS data were processed using the Gamit/Globk software package (10.4), with results validated against independent solutions produced using the Bernese software (Version 5.0) at the Dionysos Satellite Observatory (Dimitriou, 2013).

The analysis revealed measurable displacements across the caldera, particularly evident in the radial outward motion and uplift consistent with magmatic inflation processes. Linear velocities and coordinate time series were derived for both campaign and permanent stations, referenced to the ITRF08/IGS08 Reference Frame (Altamimi et al., 2012), using IGS stations to ensure geodetic consistency.

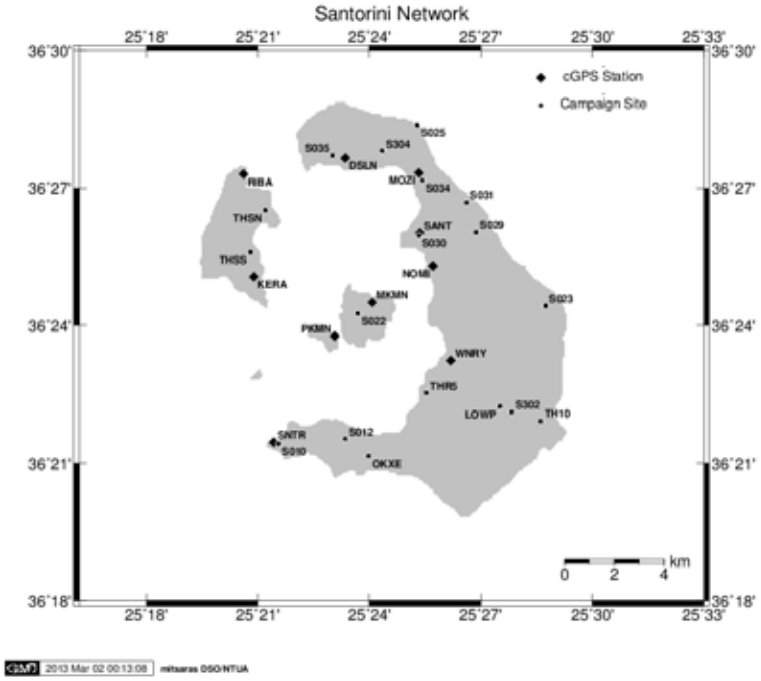

Figure 1. Santorini GNSS Network (Dimitriou, 2013)

3. Recent GNSS Campaign

In the framework of the current study, GNSS measurements were carried out at 16 benchmarks that had originally been observed during the 2012 measurement campaign (Fig. 2). The 2025 observations were conducted using dual-frequency GNSS receivers, with each session lasting at least two hours to ensure high-precision positioning suitable for geodetic applications. The measurement campaign was conducted over the period 6 – 13 February 2025, a period of time during which the seismic phenomenon was in full swing. The raw data were processed using the Bernese GNSS Software (Version 5.2) via the AUSPOS service, which delivers precise coordinate solutions in the ITRF2020 reference frame (Table 1 & 2).

However, the coordinates of the benchmarks measured at 2012 were originally computed in the IGS08 reference frame. To allow a reliable and rigorous comparison between the two epochs, a dedicated transformation and alignment procedure was implemented to bring both datasets into a common reference system and epoch.

Table 1 – GNSS Data processing parameters

Processing – Adjustment strategy	Phase preprocessing is undertaken in a baseline-by-baseline mode using triple-difference and weighted least-squares algorithm.
Reference Stations	11 IGS permanent GNSS stations
Tidal displacements	Solid earth tidal: IERS Conventions 2010 Ocean tide loading: Not applied
Tropospheric Mapping Function	DRY/WET - GMF
Orbits	IGS precise orbits
Data Windowing	7^0 elevation mask
Ambiguity resolution	Ambiguities are resolved using the Code-Based strategy for 200-6000km baselines, the Phase-Based L5/L3 strategy for 20-200km, the Quasi-Ionosphere-Free (QIF) strategy for 20-2000km and the Direct L1/L2 strategy for 0-20km.

Figure 2 - GNSS campaign (February 2025)

Table 2 - Preliminary results of GNSS processing (m)

id	X	Y	Z	σx	σy	σz
S012	4645987.168	2205009.115	3760475.682	0.007	0.008	0.026
S022	4642998.614	2204148.098	3764501.625	0.009	0.007	0.024
S023	4639536.759	2210862.974	3764705.381	0.009	0.007	0.025
S025	4637854.918	2204331.020	3770555.816	0.006	0.005	0.016
S029	4639171.945	2207601.822	3767093.660	0.01	0.008	0.03
S030	4640442.048	2205642.223	3767168.724	0.007	0.007	0.026
S031	4638679.806	2206932.288	3768055.825	0.008	0.007	0.03
S034	4639145.943	2205182.794	3768936.203	0.01	0.006	0.024
S035	4640030.934	2201621.482	3769625.629	0.007	0.007	0.029
S302	4642794.671	2210899.110	3761560.174	0.008	0.007	0.022
S304	4639217.564	2203433.204	3769888.083	0.008	0.006	0.025
TH10	4642339.911	2211981.450	3761145.342	0.008	0.006	0.021
THR5	4643592.806	2207486.308	3761951.473	0.006	0.005	0.021
THSN	4642430.113	2199760.327	3767915.240	0.019	0.008	0.039
THSS	4643652.696	2199681.385	3766578.974	0.006	0.006	0.019
OKXE	4645876.061	2205981.162	3759846.953	0.009	0.008	0.027

3.1 Methods of data analysis

To achieve compatibility between the two datasets, the 2012 coordinates in IGS08 were first transformed into the ITRF2020 reference frame using the official seven-parameter Helmert transformation, including both positional offsets and their associated rates (Altamimi et al., 2023). Additionally, to ensure that the coordinate comparisons reflect only the true displacements between the two measurement epochs, both datasets were referred to a common epoch. This step is critical because the 2012 and 2025 observations are separated by more than a decade, during which secular tectonic motion could contribute significantly to the apparent coordinate differences. For this purpose, the velocity field of Bitharis et al. (2016)—which provides high-resolution horizontal and vertical velocities for the Hellenic region based on long-term GNSS observations—was used to propagate the transformed coordinates forward in time to the epoch of the 2025 campaign. This allowed the separation of long-term tectonic trends from potential volcanic or local ground deformation signals between the two periods (Figure 3).

Once the coordinates of the campaign of 2012 were transformed into the ITRF2020 frame and propagated to the epoch of the 2025 measurements, the coordinate differences between the two epochs were computed for each benchmark. These differences were initially expressed in geocentric Cartesian coordinates (X, Y, Z), but for geophysical interpretation, they were further transformed into topocentric displacements, in the local North, East, Up (NEU) reference frame.

This transformation allows a clearer visualization and analysis of horizontal and vertical displacements relative to each station's location on the Earth's surface. The NEU components were computed using each station's geodetic latitude and longitude, following standard local frame rotation techniques. This step enables the detection of meaningful surface movements such as uplift, subsidence, or horizontal spreading that may be associated with magmatic or tectonic processes in the Santorini volcanic complex.

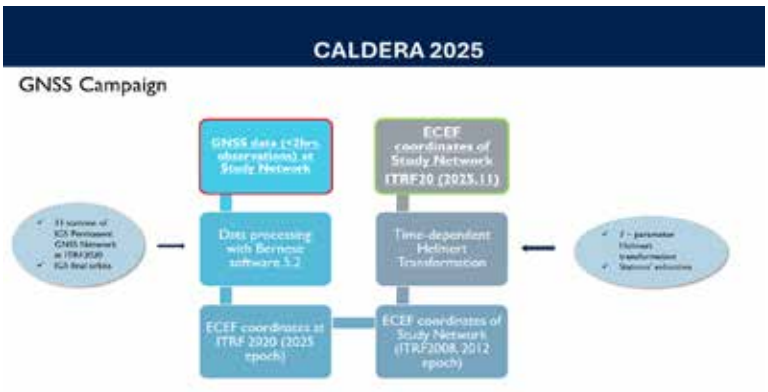

Figure 3 - Schema of the methodology for the data analysis

3.2 Preliminary Results

The comparison between the two GNSS campaign data revealed measurable displacements at the benchmarks across the Santorini Island complex. The displacements are presented both in terms of horizontal (East–North) and vertical (Up) components. The horizontal displacement vectors exhibit a radial pattern centered around the north part of the caldera, with the largest motions observed at stations located near Nea Kameni and the northern part of the island. The magnitude of horizontal displacements generally ranges from 2.5 cm to over 9 cm, suggesting a subtle but coherent deformation field (Figure 4).

Vertical displacements also show spatial variability, with most of the stations inside the caldera experiencing subsidence of up to 15 cm, while peripheral stations remain stable or exhibit minor uplift. These patterns are consistent with low-level deflation of a magmatic source beneath the caldera (Figure 5).

In addition to the comparison between the 2012 and 2025 campaigns, a short-term repeatability test was conducted to assess the internal consistency and reliability of the recent GNSS measurements. Specifically, three benchmarks were successfully re-measured with a time difference of only five days during the February 2025 campaign. These repeat measurements refer to the same reference frame (ITRF2020) and the same epoch, thus eliminating the need for any transformations or epoch propagation. Although limited in number, these observations provide a more detailed snapshot of the ongoing deformation, free from long-term tectonic signals or processing-related uncertainties. The high internal consistency between the repeated measurements enhances confidence in the reliability of the broader displacement patterns observed in the full network.

Figure 4 - Horizontal Displacements (2012-2025)

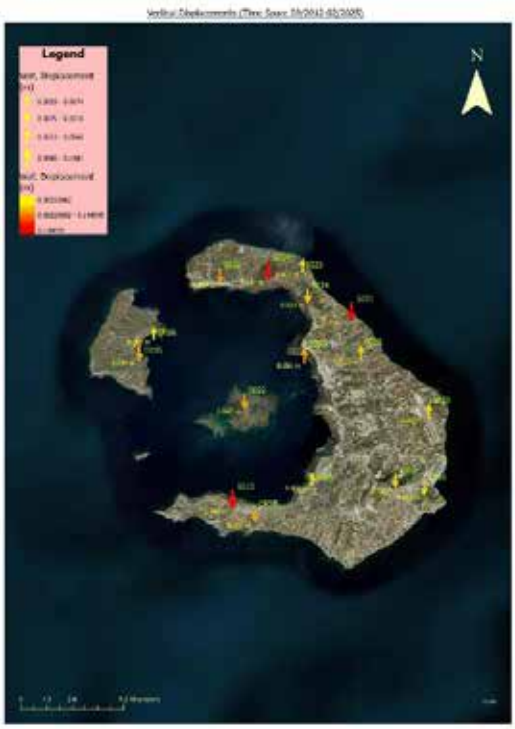

Figure 5 - Vertical Displacements (2012-2025)

The displacements derived from these short-term measurements provide an internally consistent snapshot of ongoing deformation. The horizontal displacements at these three sites range between 2.4 cm and 6.3 cm, indicating significant surface motion over just a few days. In the vertical component, the measurements revealed distinct vertical behavior: no vertical displacement at the caldera center, uplift at the southwestern station, and subsidence at the northeastern station. This spatial variation suggests that deformation is not driven by a simple, symmetric source. Instead, it may reflect a heterogeneous deflation process, possibly involving lateral magma migration or localized hydrothermal activity. The absence of uplift at the caldera center further supports the interpretation of a deflating or stabilizing magmatic system with distributed or compartmentalized subsurface dynamics. Similar patterns of spatially variable deformation were observed during the 2011–2012 unrest and attributed to complex pressurization processes within a multi-level magmatic system (Parks et al., 2012).

Figure 6 - Horizontal Displacements (2025)

Figure 7 - Vertical Displacements (2025)

4 cGNSS station analysis

The data described above were analyzed using the Bernese GNSS Software (v. 5.2) (Dach et al., 2015). Both GPS and
GLONASS observations were used when available. IGS20 was used as the frame of reference, using a set of 19 IGS stations for alignment. CODE final products were incorporated in the analysis, consistent with the frame of choice. The key parameter of interest was station coordinates (Anastasiou et al., 2024).

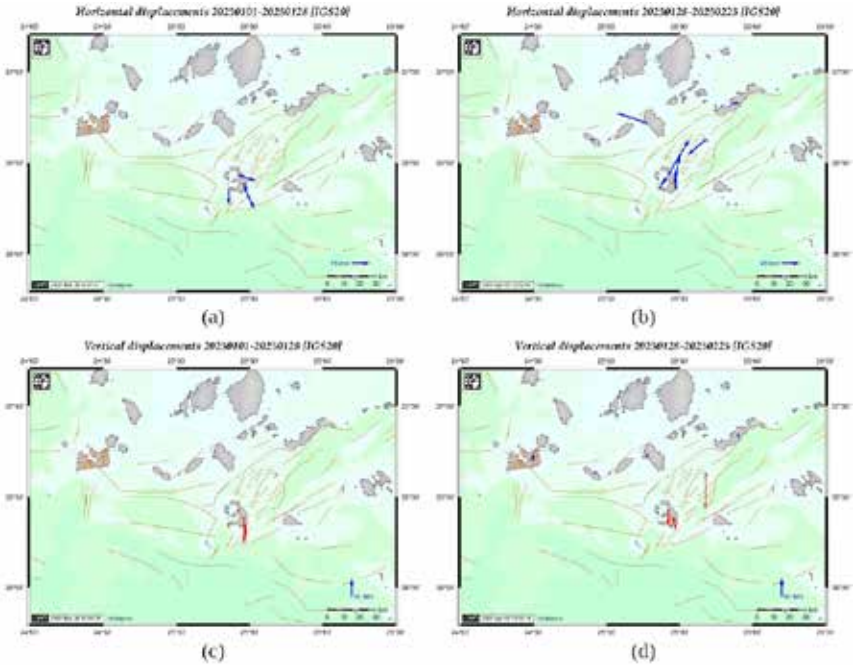

Figure 7 - Horizontal Displacements and vertical displacement of cGNSS stations for two different phases a,c: 01.01.2025-28.01.2025 and b,d: 28.01.2025-25.02.2025

Position time series analysis depicts the different movement of the stations that occurred toward the end of January 2025. Figure 7 illustrates the station displacements in different phases. In Figure 7a, a radial motion of the stations is observed up until the end of January, while in Figure 7b, the stations on Santorini Island are moving in a northeastward direction. A southwestward displacement is observed for the islet of Anydros, and displacements are also estimated on the islands of Amorgos and Ios.

Conclusions

This study presents preliminary results of ground deformation in the Santorini volcanic complex based on a comparison between GNSS campaign measurements from February 2025 and a previous geodetic campaign conducted during the 2011–2012 volcanic unrest. The data analysis, following rigorous transformations and epoch adjustments, revealed coherent displacements in both horizontal and vertical directions, indicating ongoing low-level deflation of a magmatic source beneath the caldera.

While the campaign-based measurements provided valuable spatial coverage and enabled the detection of long-term displacements, the approach has certain inherent limitations when compared to continuous GNSS (cGNSS) monitoring. Continuous GNSS stations offer high temporal resolution, allowing for the detection of short-term deformation transients, long-term trends, and episodic events that may be missed during isolated campaign observations. Moreover, cGNSS data are less affected by field-related errors such as antenna setup inconsistencies, multipath, or variations in session duration—factors that can introduce uncertainty into campaign-based results.

In contrast, the campaign method, while logistically simpler and cost-effective, captures only snapshots in time, making it less suitable for detecting subtle temporal variations or dynamic deformation processes. Nevertheless, it remains a useful tool for benchmarking long-term change, especially when co-located with cGNSS stations for cross-validation.

Future work should aim to integrate campaign results with continuous time series and InSAR data, enabling a more complete and time-resolved picture of the geodynamic processes at Santorini. Expansion of the permanent GNSS network and reoccupation of additional historical benchmarks will further improve spatial resolution and strengthen long-term volcanic monitoring in the region.

Acknowledgements

We thank the GNSS data providers NOA, NKUA, University of Patra, Hellenic Cadastre, Metrica, and JGC. These institutes and private companies provide RINEX data of permanent stations free of charge.

References

Altamimi, Z., Collilieux, X., & Métivier, L. (2011). ITRF2008: An improved solution of the International Terrestrial Reference Frame. Journal of Geodesy, 85(8), 457–473. https://doi.org/10.1007/s00190-011-0444-4

Altamimi, Z., Rebischung, P., Métivier, L., & Collilieux, X. (2023). ITRF2020: An improved realization of the International Terrestrial Reference Frame accounting for non-linear station motions. Journal of Geodesy, 97(2), 23. https://doi.org/10.1007/s00190-023-01739-2

Anastasiou D., Papanikolaou X., Serelis G., Tsakiri M. (2024). Velocity field estimated from HEPOS permanent GNSS network in Greece, preliminary results. EGU General Assembly 2024, https://doi.org/10.5194/egusphere-egu24-17390

Bagnardi, M., Hooper, A., & Wright, T. J. (2013). Revisiting the 2011–2012 unrest at Santorini: New insights from InSAR and GPS observations. Geophysical Research Letters, 40(19), 4954–4958. https://doi.org/10.1002/grl.50952

Bitharis, S., Fotiou, A., Pikridas, C., & Rossikopoulos, D. (2016). Velocity field and crustal deformation of the Hellenic area derived from GPS data (1993–2014). Journal of Geodynamics, 97, 1–16. https://doi.org/10.1016/j.jog.2016.03.003

Dimitriou, D. (2013). Processing of satellite geodetic observations in Santorini [Diploma thesis, National Technical University of Athens]. NTUA Library. (In Greek)

Dach, R., Lutz, P. Walser, P. Fridez (Eds); 2015: Bernese GNSS Software Version 5.2. User manual, Astronomical Institute, University of Bern, Bern Open Publishing.DOI: 10.7892/boris.72297; ISBN: 978-3-906813-05-9.

Druitt, T. H., Edwards, L., Mellors, R. M., Pyle, D. M., Sparks, R. S. J., Lanphere, M., & Collier, L. (1999). Santorini volcano. Geological Society, London, Memoirs, 19(1), 13–18. https://doi.org/10.1144/GSL.MEM.1999.019.01.02

Friedrich, W. L., Kromer, B., Friedrich, M., Heinemeier, J., Pfeiffer, T., & Talamo, S. (2006). Santorini eruption radiocarbon dated to 1627–1600 B.C. Science, 312(5773), 548. https://doi.org/10.1126/science.1125087

Newhall, C. G., & Punongbayan, R. S. (Eds.). (2000). Fire and mud: Eruptions and lahars of Mount Pinatubo, Philippines. University of Washington Press.

Nomikou, P., Papanikolaou, D., Parks, M. M., Pyle, D. M., Mather, T. A., Carey, S., & Livanos, I. (2014). The emergence and growth of a submarine volcano: The Kameni Islands, Santorini (Greece). GeoResJ, 1–2, 8–18. https://doi.org/10.1016/j.grj.2014.02.002

Parks, M. M., Biggs, J., England, P. C., Mather, T. A., Nomikou, P., Palamartchouk, K., ... & Pyle, D. M. (2012). Evolution of Santorini Volcano dominated by episodic and rapid fluxes of melt from depth. Nature Geoscience, 5(10), 749–754. https://doi.org/10.1038/ngeo1562

Pyle, D. M., & Elliott, J. R. (2006). Quantitative morphology, recent evolution, and future activity of the Kameni Islands volcano, Santorini, Greece. Geomorphology, 73(3–4), 242–254. https://doi.org/10.1016/j.geomorph.2005.07.009

17th INTERNATIONAL CONGRESS of the Geological Society of Greece

BULLETIN OF THE GEOLOGICAL SOCIETY OF GREECE, SP. PUBL.

EXTENDED ABSTRACT 143

SANTORY shallow seafloor observatory: First time series data from an active submarine volcano

Katsigera A.[1], Nomikou P.[1], Polymenakou P.[2], Sciré Scappuzzo S.[3], Lazzaro G.[3], Mallios A.[4], Ntouskos V.[5], Spanos S.[5], Antoniou C.[5], Rizzo A.L.[6], Longo M.[3], Escartin J.[7], Karantzalos K.[5], D Alessandro W.[3], Heimburger L.[8], Kilias S[1], Mertzimekis T[1], Grassa F.[3], Lampridou D.[1], Anagnostou E.[1]

(1) National and Kapodistrian University of Athens, Athens, Greece, evinom@geol.uoa.gr (2) Hellenic Centre for Marine Research, Heraklion, Greece (3) Istituto Nazionale di Geofisica e Vulcanologia, Sezione di Palermo, Palermo, Italy (4) Ploa Technology Consultants S.L, Girona, Spain (5) National Technical University of Athens, Athens, Greece (6) University of Milano-Bicocca, Milano, Italy (7) École Normale Supérieure, Paris Sciences Letters (PSL) University, Paris, France (8) Aix-Marseille-University, Marseille, France

Managing volcanic risk encompasses a multifaceted and crucial field, aimed at reducing the hazards posed by volcanic eruptions to human life, infrastructure, and the surrounding environment. This endeavor includes preparedness planning, monitoring, and responsive actions, with continuous monitoring of volcanic activity using state-of-the-art technology and geophysical tools being the first and most essential step (Katsigera et al., 2024).

SANTORY is a state-of-the-art project aiming at submarine volcanic hazard monitoring in the Aegean Sea. Focused on the Kolumbo submarine volcano NE of Santorini Island, this cutting-edge observatory combines advanced imaging, geophysical and geochemical measurements, and real-time monitoring technologies to address one of the region's most important volcanic threats (Nomikou et al., 2022).

For the operation of the observatory, three oceanographic cruises were conducted, during which specialized scientific instruments were deployed inside the crater for several months (Figure 1), later retrieved to collect data, and subsequently re-deployed. These instruments included: the SANTORY underwater observatory, which comprised sensors for collecting acoustic data, temperature (T°C), CO_2, H_2S, O_2, pressure, electrical conductivity (EC), pH, and turbidity; tilt current meters for measuring marine currents within the crater; specialized thermometers for monitoring temperature changes in the polymetallic chimneys of the hydrothermal field; optical cameras positioned in front of active polymetallic chimneys to record hydrothermal fluid flow; and advanced underwater recording stations for measuring physical parameters in water, such as turbidity, temperature, conductivity, pressure, and oxygen levels. Additionally, the ROV was equipped with the following instruments for real-time data collection: a multispectral and stereo camera ("THEIA") for capturing the texture of the seafloor with multispectral data; the gSniffer device for real-time γ-radiation measurements; the γ-radiation imager ("SUGI") for real-time γ-radiation imaging; and a UV camera ("CHERI") for detecting Cherenkov radiation, marking a global first in underwater applications (Figure 2).

Over the past two years, SANTORY has provided unprecedented insights into Kolumbo's geological dynamics and volcanic activity. High-resolution 3D mapping revealed steep slopes, mass-wasting deposits, and hydrothermal vent fields, critical for assessing seafloor instability and potential eruption risks. Novel hyperspectral imaging and autonomous video systems have captured persistent vent activity, bubbling plumes, and environmental changes, thus providing the most complete assessment of hydrothermal processes to date and establishing a baseline for potential tracking of underlying volcanic processes.

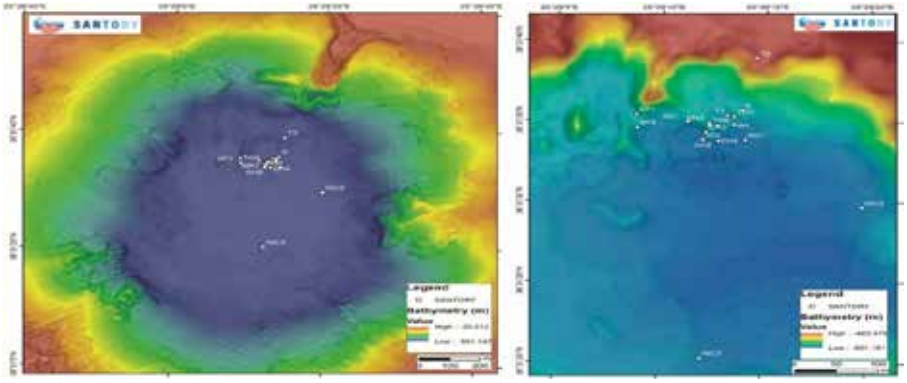

Figure 1. Bathymetry map of Kolumbo crater. Bathymetric data were collected by GEOMAR's autonomous underwater vehicle (AUV) Abyss during mission POS 510 (Hannington et al, 2018). The points indicate the location of the SANTORY observatory and its instruments along the hydrothermal vent field.

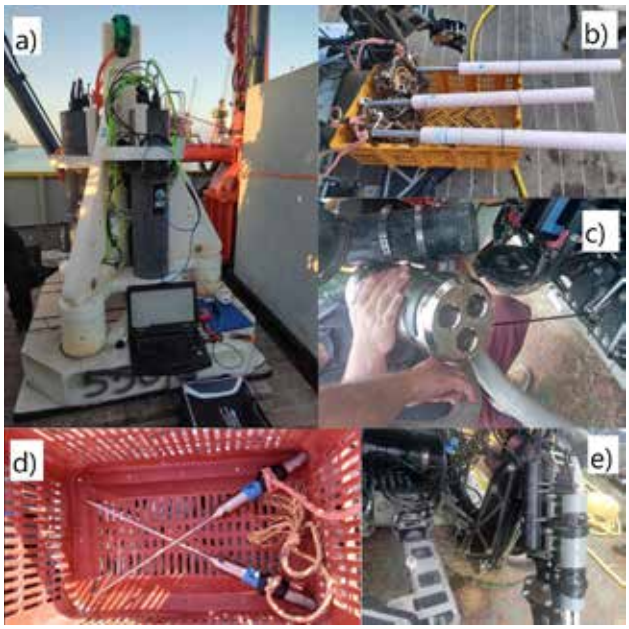

Figure 2. Photographs showing a) the SANTORY observatory, b) The tilt current meters of SANTORY placed in the Kolumbo crater, c) the multispectra and stereo camera "THEIA", d) the sensitive high-temperature thermometers and e) gSniffer for real-time γ-radiation measurements, conducted for the first time on a global scale.

Autonomous sensors deployed on the crater floor have been monitoring hydrothermal outflow temperature, pressure, and chemistry of fluids; these parameters will help quantify chemical fluxes, and reveal periodic variations driven by tides, in addition to magmatic activity. Datasets revealing these hydrothermal fluctuations may thus be critical in detecting precursor signals of volcanic unrest (e.g., changes in subsurface permeability, magmatic degassing). Chemical and isotopic analyses of hydrothermal fluids have revealed the degassing of CO_2-rich fluids characterized by a mantle-like 3He/4He signature. These findings highlight Kolumbo's potential for hazardous eruptions and its classification as a high-risk volcanic system.

Through the program, innovative results emerged, highlighting the uniqueness of the Kolumbo submarine volcano. Acoustic data collected every 30 minutes included one-minute recordings that revealed local hydrothermal events and bubble activity related to CO2 release in the 4000-8000 Hz range (Figure 3). Algorithms were developed to differentiate hydrothermal noise from environmental background noise, identifying bubble radii primarily in the range of 0.20-0.54 mm. Persistent and active bubble activity was observed within the hydrothermal field, with high temperature recordings (232°C) inside hydrothermal chimneys. Local hydrothermal events and fluid dynamics were identified, showing synchronized variations and anomalies in current meters, significant cooling phenomena, and high-velocity currents regulated by tidal forces.

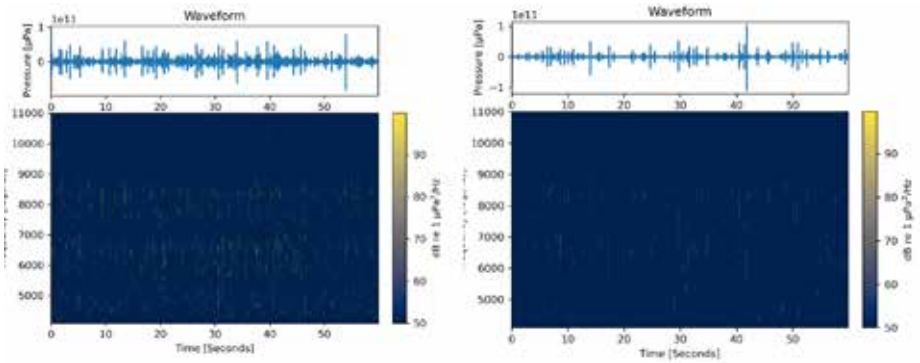

Figure 3. Bubble activity recording from the SANTORY observatory. Bubble activity was detected in the range of 4000-8000 Hz. Due to the presence of ambient noise overlapping the same band, a specialized algorithm was developed to better isolate bubble noise events.

Geochemical analysis confirmed acidic and slightly reducing conditions on the crater floor, helium isotopic composition indicating mixing of atmospheric and magmatic sources, and high concentrations of mercury (Hg) and methylmercury (MeHg) pointing to potential natural pollution. CO2 concentrations were extremely high (96%). Water samples collected at various depths showed anomalies in magmatic/geothermal gases, while trace elements such as Mn, Cs, and Hg exhibited significant deviations. A pH decrease above active chimneys was observed between December 2022 and October 2023, with the lowest value recorded during the last expedition (pH=5.33; 10/2023).

For the first time, natural radioactivity data were recorded within the Kolumbo hydrothermal field. The typical radioactivity measurement rate recorded away from the seafloor and known hydrothermal fields ranges around 1–2 counts per second. In contrast, radioactivity near the hydrothermal chimneys of Kolumbo reaches an impressive level, approximately three orders of magnitude higher, with a maximum of 996 counts per second (Figure 4).

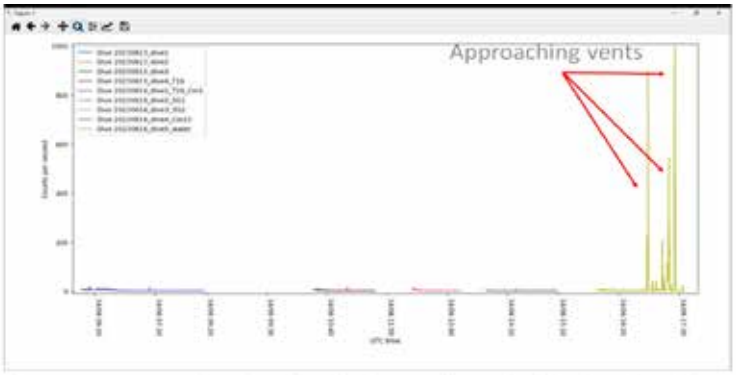

Figure 4. Radioactivity measurements inside the Kolumbo crater. Radioactivity near the hydrothermal chimneys reaches an impressive level, approximately three orders of magnitude higher, with a maximum of 996 counts per second.

Additionally, isolation of microorganisms from Kolumbo's extreme environment was achieved, where these microorganisms are of particular interest for biotechnological applications as they possess unique mechanisms for adapting to extreme conditions. Microbial data also unveiled diverse communities thriving in hydrothermal vent systems, offering insights into their metabolic pathways and resilience mechanisms. Metagenomic analyses uncovered new information about the carbon and methane cycles, which directly impact our planet's climate.

The project results provide valuable information for assessing volcanic hazards, contributing to the protection of the region from natural disasters, safeguarding human lives, and supporting the local economy. SANTORY is more than a research project—it is an initiative for developing a protocol for volcanic hazard mitigation that can be extrapolated to other submarine systems. By integrating cutting-edge technologies and multidisciplinary expertise, the project delivers actionable insights to improve early warning systems and protect vulnerable coastal communities. SANTORY sets a new benchmark in safeguarding against submarine volcanic threats.

All scientific data are accessible through the SANTORY Open Data Hub platform, available to both the residents of the Municipality of Thira and the scientific community. https://santory-open-data-hub-nom.hub.arcgis.com/

Acknowledgements

We are thankful to the International Ocean Discovery Program (IODP), the technical staff of the JOIDES Resolution, and all of the shipboard personnel for a great expedition. We also thank the member organizations of IODP for financial aid, and the Municipality of Thera for help in preparing for the expedition.

References

Katsigera, A., Nomikou, P., & Pavlopoulos, K. (2024). A Preliminary Hazard Assessment of Kolumbo Volcano (Santorini, Greece). GeoHazards, 5(3), 816-832. https://doi.org/10.3390/geohazards5030041

Nomikou P, Polymenakou PN, Rizzo AL, Petersen S, Hannington M, Kilias SP, Papanikolaou D, Escartin J, Karantzalos K, Mertzimekis TJ, Antoniou V, Krokos M, Grammatikopoulos L, Italiano F, Caruso CG, Lazzaro G, Longo M, Scire´ Scappuzzo S, D'Alessandro W, Grassa F, Bejelou K, Lampridou D, Katsigera A and Dura A (2022) SANTORY: SANTORini's Seafloor Volcanic ObservatorY. Front. Mar. Sci. 9:796376. doi: 10.3389/fmars.2022.796376

Hannington, M. D. (2018). RV POSEIDON Fahrtbericht/Cruise Report POS510-ANYDROS: Rifting and Hydrothermal Activity in the Cyclades Back-Arc Basin, Catania (Italy)–Heraklion (Greece) 06.03.-29.03. 2017.

17th INTERNATIONAL CONGRESS of the Geological Society of Greece

BULLETIN OF THE GEOLOGICAL SOCIETY OF GREECE, SP. PUBL.

EXTENDED ABSTRACT 144

Flash drought assessment: insights from Lesvos island, Greece

Katsora, C.[1], Leivadiotis, E.[2], Tzoraki, O. [1], Papadopoulou, N.[1]
(1) University of the Aegean, Mytilini, Lesvos, Greece, geoha23008@geo.aegean.gr, ckatsora@gmail.com
(2) University of Thessaly, Volos, Greece

Traditional drought definitions characterize them as prolonged periods of below-average precipitation, resulting in gradual soil moisture depletion (Wilhite & Glantz, 1985). However, the emergence of flash droughts (Christian et al., 2021), characterized by rapid onset and intensification, challenges this traditional view. While a universally accepted definition remains elusive, key characteristics include rapid soil moisture depletion, often within days or weeks, and significant impacts on agriculture, livestock, and water resources (Oetkin et al., 2018).

Effective flash drought monitoring is crucial for early warning systems and mitigation efforts (Pakkasagi et al., 2023). Monitoring techniques (Lisonbee et al., 2021) encompass satellite remote sensing for soil moisture, vegetation health, and precipitation; ground-based observations from weather stations and soil moisture networks; meteorological models for forecasting; and drought indices such as the Standardized Precipitation Index (SPI) (McKee, 1993), the Evaporative Demand Drought Index (EDDI) (Li et al., 2024), and the Standardized Precipitation Evapotranspiration Index (SPEI) (Spinani et al., 2017).

This study investigates historical flash drought occurrences on Lesvos island (Figure 1a), Greece, an island characterized by a hot-summer Mediterranean climate (Csa), that experiences significant seasonal and spatial rainfall variability, high temperature oscillations, and an average annual temperature of 17.78 °C. The island exhibits diverse vegetation types, reflecting its natural environment and historical agricultural practices (Figure 1b), which can influence vulnerability to flash drought events.

The historical flash drought events have been identified by employing two indices, requiring minimal datasets while yielding reliable results: the Standardized Precipitation Evapotranspiration Index (SPEI) and Soil Moisture (SM).

Figure 2 provides a graphical illustration of the methodology employed for FD identification using the SPEI. This represents a simple climatic water balance (i.e. difference between precipitation and potential evapotranspiration (PET). Meteorological data, comprising precipitation and temperature records from the Agia Paraskevi, Akrasi, and Sigri stations (Figure 1a), were analyzed using R scripts to identify historical flash drought events. This analysis identified forty flash drought events within the past 15 years (Figure 3), with a peak occurrence between March and June (Figure 4a) and an average duration of approximately eight pentads (Figure 4b). The years 2018 and 2012 experienced the most intense (Figure 4c) and severe (Figure 4d) flash drought events within the northeast and north regions, respectively.

Hourly soil moisture data from the ERA5 reanalysis dataset (1950-2024) were used to evaluate the spatial extent, frequency, magnitude, and intensity of flash drought events across Lesvos island. Following the methodology outlined in Figure 5, the results show a higher frequency of flash droughts in the northern part of the island (Figure 6a). The most severe events, characterized by higher magnitude and intensity (graphically presented as percentages), were also observed in the north-northeastern region (Figure 6b,c).

Given the success of this methodology, which integrates meteorological data (precipitation and temperature) with satellite-derived soil moisture, it has the potential for application in other Mediterranean regions with similar climatic characteristics. This approach can be valuable for identifying flash drought occurrences, assessing associated risks, and developing effective mitigation and adaptation plans.

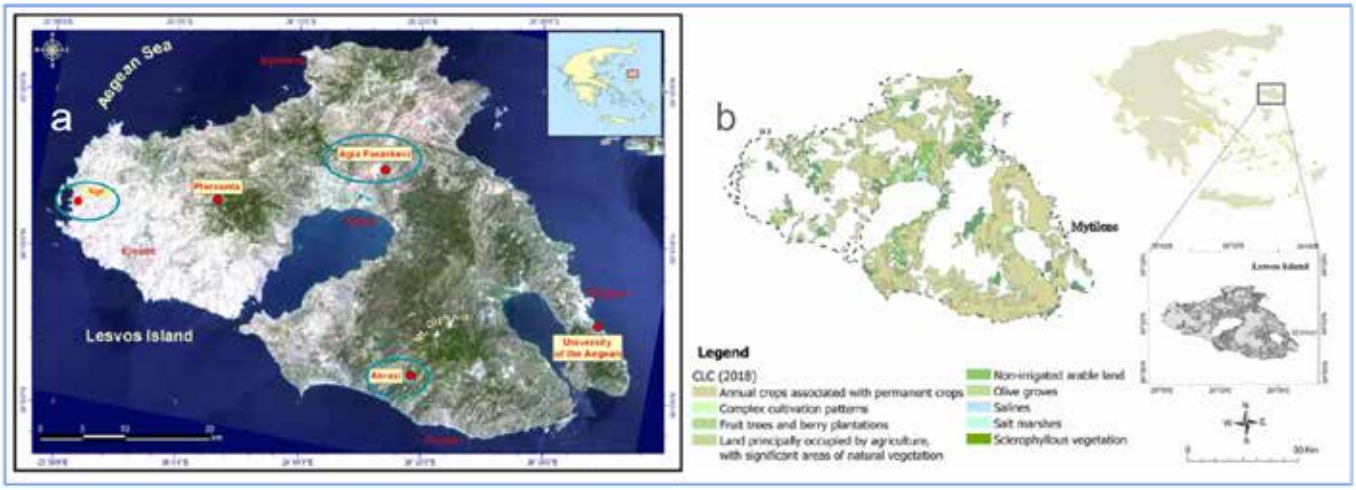

Figure 1: a. Area of interest with available meteorological stations, b. Vegetation types in Lesvos (Palaiologou *et al.*, 2012)

Step 1

Prepare data (precipitation, maximum temperature and minimum temperature):

- remove missing values,
- define the analysis period,
- aggregate the daily data into pentads (five-day periods).

Step 2

Calculate SPEI for each pentad:

- calculate potential evapotraspiration (PET), using Thornthwaite method,
- compute the water balance as the difference between precipitation and PET (Precipitation - PET).

Step 3

Identify flash drought events when SM value falls between the 40th and 20th percentile, with event durations up to 8 pentads (40 days):

- exclude events shorter than 4 weeks from further analysis,
- focus on detecting valid endpoints of FD events that meet the defined criteria,
- remove overlapping onset-endpoint pairs to ensure independent event identification.

Step 4

Calculate flash drought characteristics:

- Frequency: Calculate the total frequency of the FD events,
- Duration: calculate the duration of each FD event, as the absolute value between the start and end pentad, divided by 5 (expressed in days),
- Magnitude: calculate the magnitude of each FD events as the absolute difference between the endpoint and the SPEI value at the onset,
- Intensity, calculate the intensity of each FD event by dividing the magnitude by the duration.

Figure 2: Methodology for identifying flash droughts (based on SPEI)

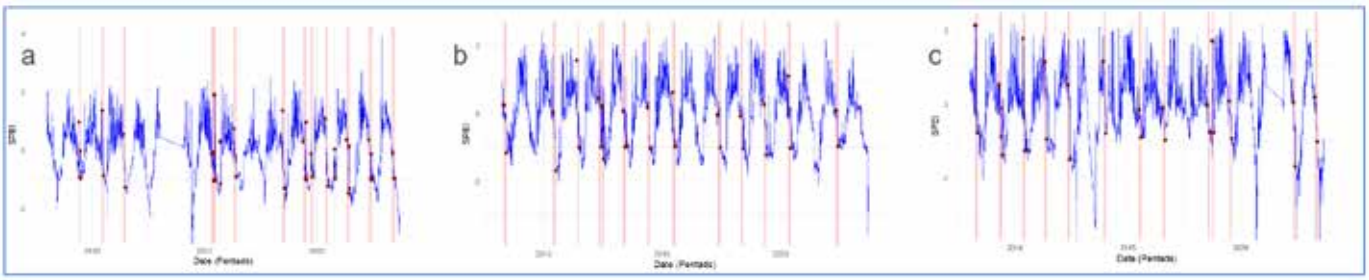

Figure 3: Identification of flash droughts events (based on SPEI), in a. Agia Paraskevi, b. Akrasi and c. Sigri

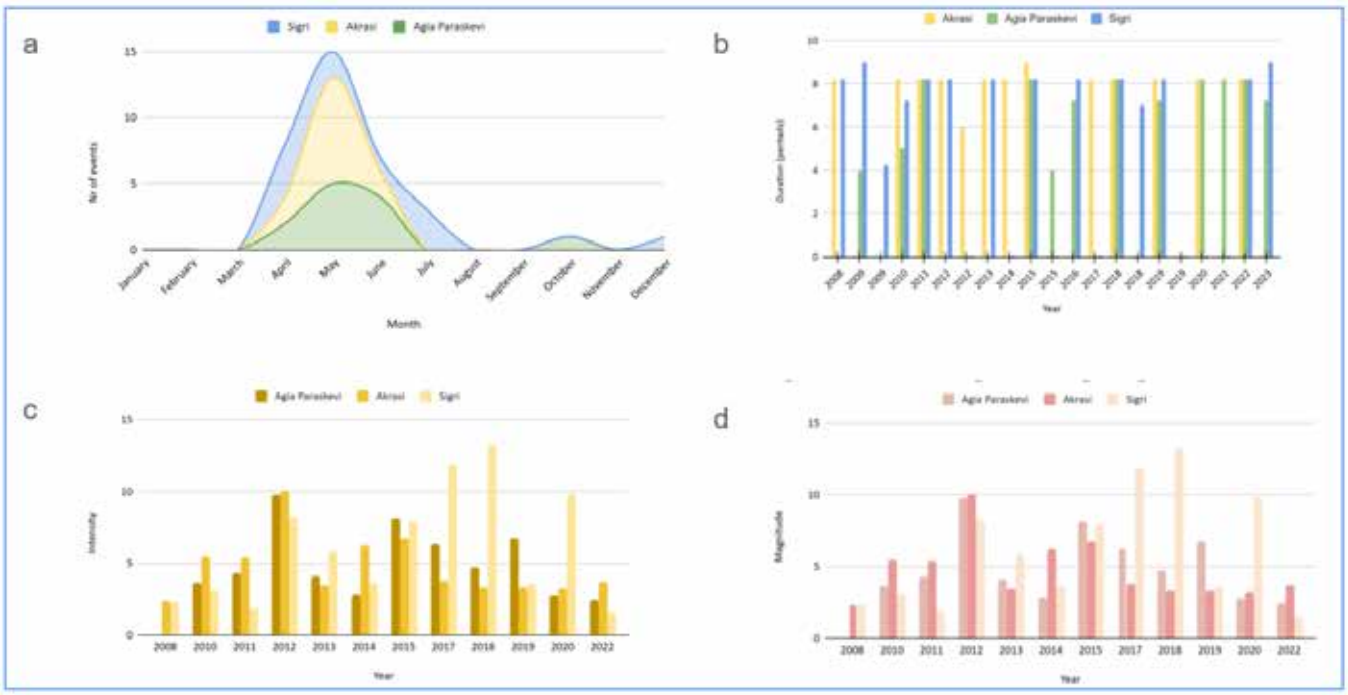

Figure 4: a. Seasonality, b. Duration in pentads, c.Intensity and d. Magnitude of flash droughts (based on SPEI)

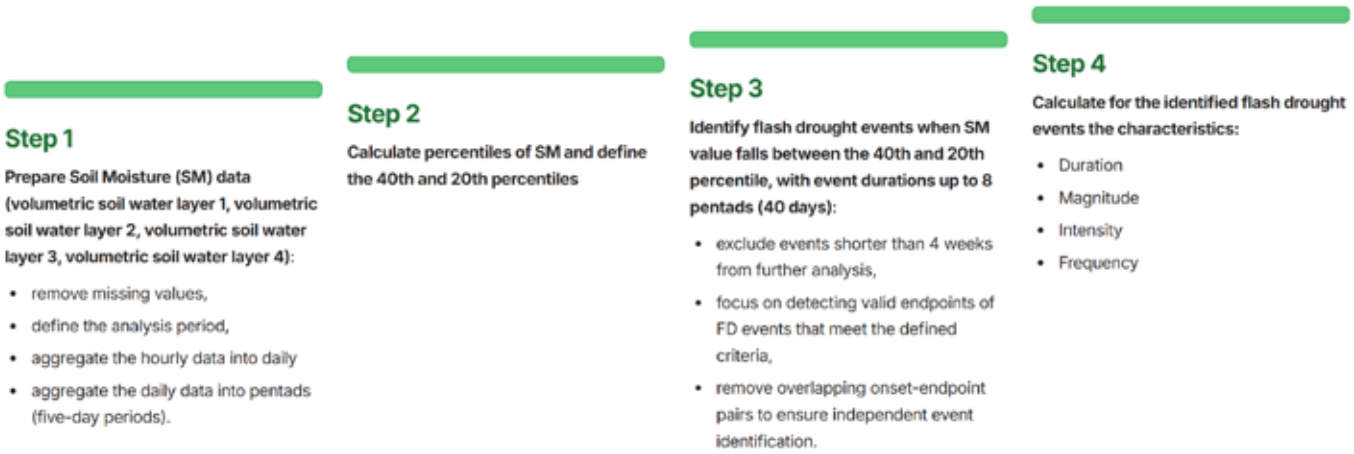

Figure 5: Methodology for identifying flash droughts (based on SM)

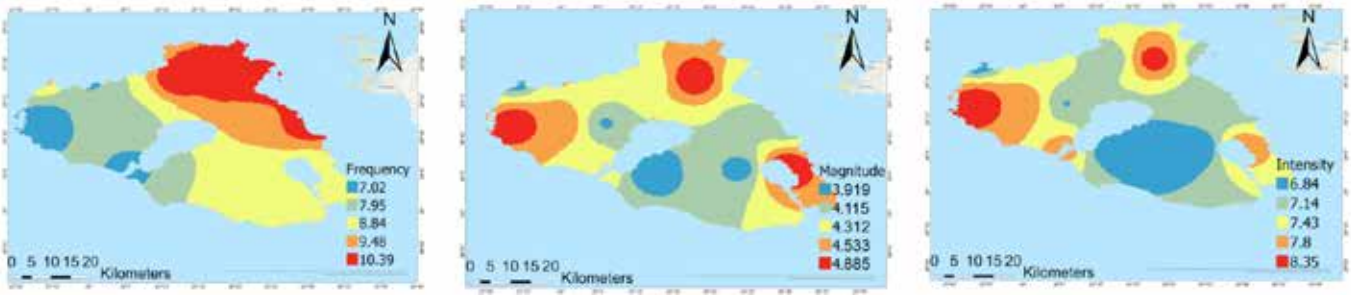

Figure 6: Flash droughts frequency, magnitude and intensity (based on Soil Moisture)

References

Christian, J.I., Basara, J.B., Hunt, E.D., Otkin, J. A., Furtado, J.C., Mishra, V., Xiao, X., & Randall, R.M., 2021. Global distribution, trends, and drivers of flash drought occurrence. Nature Communication 12, 6330. https://doi.org/10.1038/s41467-021-26692-z.

Li, H., Choy, S., Zaminpardaz, S., Wang, X., Liang, H., Zhang, K., 2024. Flash drought monitoring using diurnal-provided evaporative demand drought index, Journal of Hydrology, Volume 633, 130961, ISSN 0022-1694, https://doi.org/10.1016/j.jhydrol.2024.130961.

Lisonbee, J., Woloszyn, M.,Skumanich, M., 2021: Making sense of flash drought: Definitions, indicators, and where we go from here. Journal of Applied and Service Climatology, (1), 1–19, https://doi.org/10.46275/JOASC.2021.02.001.

McKee, T.B., Doesken, N.J., Kleist J., 1993. The relationship of drought frequency and duration to time scales. In: Paper Presented at Eighth Conference on Applied Climatology, American Meteorological Society, Anaheim, CA.

Otkin, J. A., Svoboda, M., Hunt, E. D., Ford, T. W., Anderson, M. C., Hain, C., & Basara, J. B., 2018. Flash droughts: A review and assessment of the challenges imposed by rapid-onset droughts in the United States. *Bulletin of the American Meteorological Society*, *99*(5), 911-919.

Palaiologou, P., Kalabokidis, K., Haralambopoulos, D., Feidas, H., Polatidis, H., 2011. Wind characteristics and mapping for power production in the Island of Lesvos, Greece. Computers & Geosciences 37 (7), 962-972.

Rakkasagi, S., Poonia, V., & Goyal, M. K., 2023. Flash drought as a new climate threat: drought indices, insights from a study in India and implications for future research. Journal of Water and Climate Change, 14(9), 3368-3384.

Spinoni, J., Naumann, G., Vogt, J., 2017. Pan-European seasonal trends and recent changes of drought frequency and severity. Global Planetary Change. 148, 113–130.

Wilhite, D.A., and M.H. Glantz, 1985. Understanding the drought phenomenon: The role of definitions. Water International. 10, 111-120.

Zeng, Z., Wu, W., Peñuelas, J., Li, Y., Jiao, W., Li, Z., Ren, X., Wang, K., Ge, Q., 2023. Increased risk of flash droughts with raised concurrent hot and dry extremes under global warming. Climate and Atmospheric Science 6, 134. https://doi.org/10.1038/s41612-023-00468-2.

17th INTERNATIONAL CONGRESS of the Geological Society of Greece

BULLETIN OF THE GEOLOGICAL SOCIETY OF GREECE, SP. PUBL.

EXTENDED ABSTRACT 145

Rainfall-induced landslides in Corfu island: effectiveness of the regional scale landslide susceptibility map

Kavoura K.[1], Konstantopoulou G.[1], Paschos P.[1]
(1) Hellenic Survey of Geology and Mineral Exploration, Acharnaes, Greece, aikavoura@eagme.gr

Research Highlights

Introduction

A long term investigation on landslide phenomena in Corfu Island, consumes that the majority of them are strongly connected with rainfall events hit Western Greece and Ionian Sea islands, annually. The last years an increasing number of precipitation events occurred in Greece are characterized by meteorologists as extreme events, with a large amount of rain falls in a short time. Depending on the geomorphological and geological conditions of a specific area, this kind of events usually induce soil erosion moreover lead to landslides and floods. For Corfu island, according to the Hellenic National Meteorological Survey the mean annual rainfall is around 1100mm, while high rainfall frequency between October and November is recorded. Additionally, the abundance of recent landslides occur in this period. Based on the landslide database of the Hellenic Survey and Mineral Exploration (H.S.G.M.E.) from 1959 to 2022, 203 landslides in a 592 km^2 area have been officially recorded and mapped into a multi-temporal landslide inventory map.

Analyzing the landslides inventory some interesting results are extracted about landslide features. It is shown that 77% of the landslides are hosted in Neogene sediments followed by Quaternary formations and artificial fills while several rockfalls occur in limestones. Serious instability phenomena are often observed as rotational or translational slides (80%), while in some cases complex landslides occur. Moreover, soil creep often be an important process on extensive areas of the island. Almost 85% of the recorded landslides are located within residential areas and road network, while the rest within forests and cultivated lands (Konstantopoulou *et al*., 2019). In addition, it is stated that rainfall consists the main triggering factor of landslides in this area.

In general, the study area is prone to landslides, but where? Landslide susceptibility assessment is an important tool for identifying areas prone to landsliding. A preliminary landslide susceptibility map of the Corfu Island was presented by Konstantopoulou *et al*., 2022, using the Frequency Ratio (FR) statistical model and four commonly used predisposing factors (lithology, land use, slope, distance from road network). That assessment had a very good ability to classify landslides in susceptibility zones with ROC curves analysis give an AUC=0.895. A newer landslide susceptibility assessment was presented by Kavoura *et al*., 2024 using FR model and six predisposing factors (lithology, land use, slope, road network density, distance from rivers, distance from faults).

An important stage in landslide susceptibility assessment is to evaluate the effectiveness of the produced landslide susceptibility map by transparent validation. The standard evaluation approach is to analyze the agreement between the resulting map and observed data (Corominas *et al*., 2014). This study discusses the quality of the final landslide susceptibility map highlighting the transparency and the acceptance of such maps.

Objectives

Many techniques have improved in order to evaluate the quality of landslide susceptibility models. In this study besides the ordinary validation checks, such as Receiver Operating Characteristics (ROC), the actual predictive performance of future landslide phenomena also be assessed.

The objective of this study was to provide a coordinated approach for quality assessment of landslide susceptibility analysis by focusing not only on the calculation, but also on the evaluation process, even if the landslide susceptibility assessment was prepared under a statistical based method (FR model). More precisely, this approach uses retrospective data from landslides to examine the predictive performance of landslide susceptibility map (Fleuchaus *et al*., 2021). The predictive performance of the susceptibility map was evaluated based on different landslide events triggered by heavy rainfall events between 2022 and 2024.

Methods

For the assessment of susceptibility at regional (1:50,000) scale, six key-role predisposing factors were selected that are often used in such analyses based on literature review and experience in landslide studies. The factors were chosen to reflect the general geological, topographic and environmental settings in the study area:

1. Road network density, represents the impact of road network in occurrence of landslides (Figure 1a)
2. Slope angle, is a fundamental factor in slope stability analysis leading also the landslide mechanism (Figure 1b)

3. Land cover, this factor is associated with human activities. Changes in land uses bring changes to landslide susceptibility (Figure 1c)
4. Geotechnical units, one of the most important factors while failure occurs because the force of gravity becomes greater than either friction or the internal strength of the rock or soil (Figure 1d)
5. Distance from faults, refers to the geotechnical quality of rockmass and soil formations (Figure 1e)
6. Distance from hydrographic network (Figure 1f)

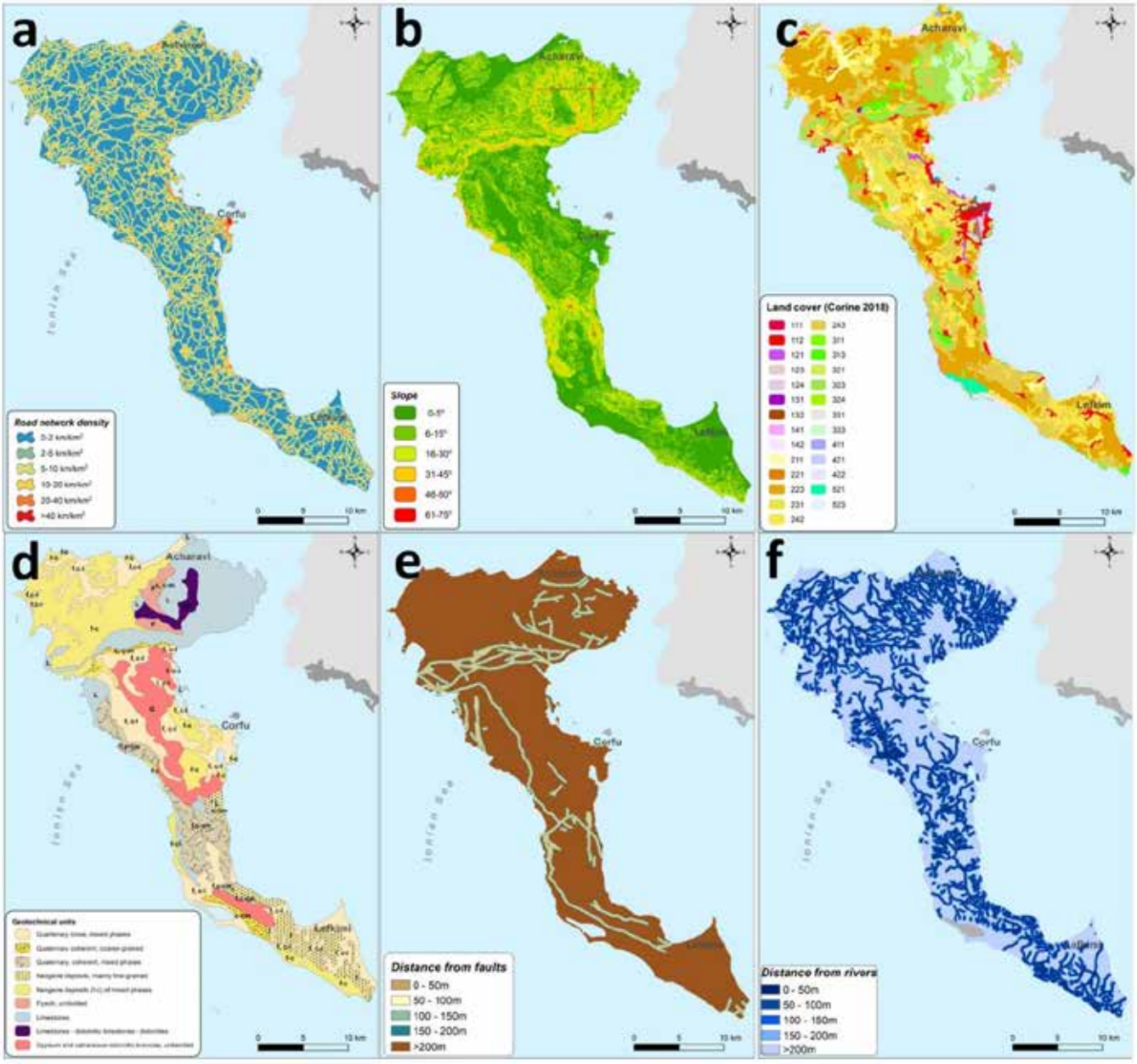

Figure 1. Predisposing factors a) Road network density, b) Slope angle, c) Land cover, d) Geotechnical units, e) Distance from faults and f) Distance from hydrographic network

The Frequency Ration (FR) model was applied to define weights for each factor, using the ratio of the per-centage of landslides in a class of the selected factor to the percentage of the area of this class in the study area. The classification of the susceptibility level is given in a percentage scale of 10%, so that each class differs from the next in terms of the degree of susceptibility, i.e. the probability of a landslide occurring in the area according to the conditions of the area, by 10%. The lower the percentage the lower the susceptibility level (Figure 2).

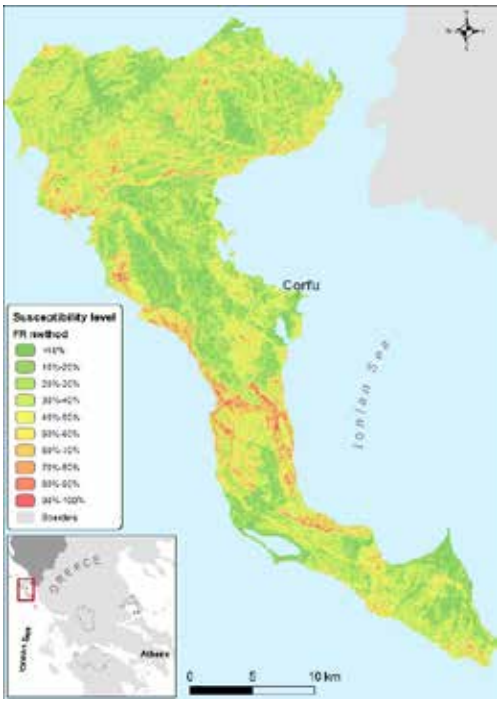

Figure 2. Landslide susceptibility map of Corfu Island

Receiver Operating Characteristic (ROC) curves were used, firstly for checking the reliability of the proposed model (success rate curves) as well as to check the ability of the model to pinpoint landslide-prone areas (prediction rate curves). In the first face, the model was checked using a training set of landslides (landslides were activated before 2020) and an equal number random set of points free of landslides. The process was repeated for the validation set of landslides (landslides were activated after 2020) in order to find if these independent landslide occurrences were correctly adapted in different susceptible areas. It is indicated that in Corfu Island the model can correctly predict the susceptible areas while AUC value is approximately 0.9 ($AUC_{success}$= 0.893 and $AUC_{predict}$=0.906).
Although the study achieves an AUC value higher than 80%, the landslide susceptibility map is subject to the predictive power of landslides activated after 2022, considering the impact of inaccurate input data or the over- and underestimation of causative factors. For this reason, a brief search was made in the local press to find unrecorded landslides in the HSGME database that were activated after 2022. This resulted in the identification of four independent rainfall – induced landslide events in different parts of the island according toTable1.

Table 1. Landslide events after 2022

Landslide event	Rainfall event	Rainfall[1]	Area
1st	8-13/12/2022	57.4 mm	Agios Dimitrios – Chlomos
2nd	19/8/2024	19.4 mm	Ano Garouna
3rd	9-10/9/2024	133 mm	Sinarades – Agios Gordios
4rth	8/1/2025	19.2 mm	Episkepsi (Megas Lakkos)

1: Weather station of Gouvia, Corfu (National Observatory of Athens network).

Results and Conclusions

The posterior validation of the landslide susceptibility map was performed based on the distribution of landslides for individual susceptibility classes (Pareek *et al*., 2024). According to Figure 3a, the majority of landslides are located along slopes in the Chlomos area predicted as being highly susceptible to landslides over 75%. Both landslides of 2024 were activated in Ano Garouna village (Figure 3b) and Sinarades – Agios Gordios (Figure 3c) area were well predicted and plotted into the susceptibility class of 70%-80%. The most recent landslide occurred in January 2025 on a slope of a mountainous road in North Corfu. As illustrated in the Figure 3d the phenomenon is closely linked to a highly susceptible zone along the road.

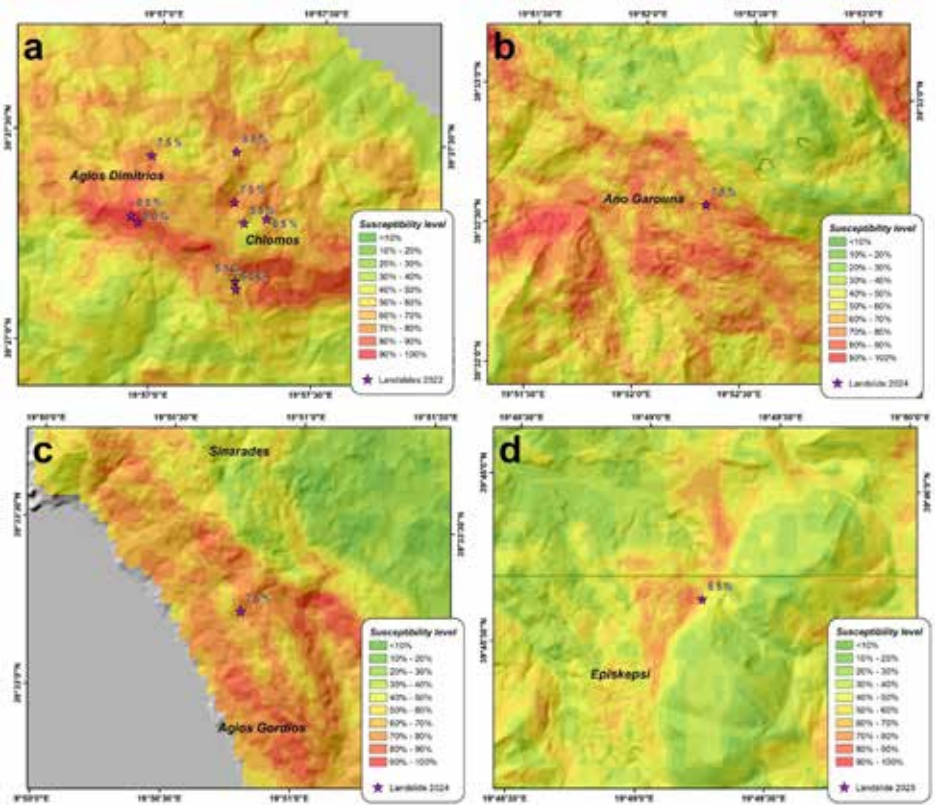

Figure 3. Evaluation of landslide susceptibility map abstracts with overlaid recent landslides at a) Chlomos and Agios Dimitrios villages, b) Ano Garouna village, c) area between Sinarades and Agios Gordios and d) wider area of Episkopi village

The retrospective validation presented in this study revealed significant correlation of the landslide susceptibility map of Corfu Island with respect to recent landslides for the period 2022 – 2025. In particular, the 60 % of the landslides, were activated into the susceptibility class of 70%-80%. This work highlights that the retrospective validation approach could be a promising assessment tool in the field of landslide susceptibility evaluation. While HSGME serves the Nation by providing reliable scientific information and thus minimizing loss of life and property from natural disasters, this research could be a basic tool for managing a sustainable hazard and risk mitigation program in landslide prone areas

References

Corominas, J., Van Westen, C., Frattini, P., Cascini, L., Malet, J.-P., Fotopoulou, S., Catani, F., Van Den Eeckhaut, M., Mavrouli, O., Agliardi, F., Pitilakis, K., Winter, M.G., Pastor, M., Ferlisi, S., Tofani, V., Hervás, J., Smith, J.T., (2014) Recommendations for the quantitative analysis of landslide risk. Bull Eng Geol Environ 73(2):209–263.

Fleuchaus, P., Blum, P., Wilde, M. Terhorst, B., Butscher, C., 2021. Retrospective evaluation of landslide susceptibility maps and review of validation practice. *Environ Earth Sci* **80**, 485. https://doi.org/10.1007/s12665-021-09770-9

Kavoura, K., Spanou, S., Apostolidis, E., Kokkali, P., 2024. Regional Landslide Susceptibility Assessment: Case Studies from Greece. Proceedings of the 6th Regional Symposium on Landslides in the Adriatic-Balkan Region, ReSyLAB2024, ISBN 978-86-7352-402-3. - Vol. 6:193–197. https://doi.org/10.18485/resylab.2024.6.ch27

Konstantopoulou, G., Exintaridi, A., Paschos, P., Nikolaou, N., 2019. Landslide hazard in Corfu Island, Greece. SafeCorfu 2019 □ 6th International Conference on Civil Protection & New Technology

Konstantopoulou, G., Kavoura, K., Exintaridi, A., Paschos, P., 2022. Landslide inventory and preliminary susceptibility mapping of Corfu Island, Greece. 16th International Congress of the Geological Society of Greece, Patras, Greece, Sp. Publ. 10, Ext. Abs. GSG2022-197

Pareek, T., Bhuyan, K., van Westen, C., Rajaneesh, A., Sajinkumar, K. S., Lombardo, L., 2024. Analyzing the posterior predictive capability and usability of landslide susceptibility maps: a case of Kerala, India. Landslides. https://doi.org/10.1007/s10346-024-02389-4

17th INTERNATIONAL CONGRESS of the Geological Society of Greece

BULLETIN OF THE GEOLOGICAL SOCIETY OF GREECE, SP. PUBL.

EXTENDED ABSTRACT 146

Origin of nitrate pollution in groundwater of Mygdonia Plain, Greece

Kazakis Nerantzis[1*], Sideri Ioanna[1], Ntona Maria Margarita[2], Stavropoulou Vasiliki[1], Lampropoulou Dimitra [3], Zagana Eleni[1], Voudouris Konstantinos[2]

(1) Laboratory of Hydrogeology, Department of Geology, University of Patras, Faculty of Natural Sciences, 26504 Rion, Patras, Greece, nkazakis@upatras.gr (2) Laboratory of Engineering Geology & Hydrogeology, Department of Geology, Aristotle University of Thessaloniki, 54124 Thessaloniki, Greece (3) Department of Chemistry, Aristotle University of Thessaloniki, 54124 Thessaloniki, Greece

Research Highlights

- The highest concentration of nitrate is 208 mg/L occurring during the dry period.
- Dual nitrate isotopes in groundwater samples from deep boreholes indicate manure and sewage as primary nitrate sources.

Introduction / Background

Groundwater and surface water nitrate pollution constitute an important environmental issue worldwide. The primary source of nitrate pollution is usually human activities, particularly in regions heavily influenced by agriculture and livestock farming (Kazakis *et al*., 2020). In numerous aquifers across Greece, nitrate concentrations exceed the maximum permissible limit for drinking water (50 mg/L), raising significant concerns due to their potential adverse impacts on human health (Daskalaki and Voudouris, 2008). This research was conducted in a Mediterranean region affected by nitrate pollution where the groundwater originates from porous, karsts and fractured rock aquifers.

This study is focused on the administrative boundaries of DEYA Oraiokastrou due to the elevated concentrations of nitrate in drinking water. The determination of nitrate origin and regime in the porous aquifer is of utmost importance in order to map the polluted aquifer layers and locate zones with nitrate concentration below the permitted drinking limit (50 mg/L).

Study area

The study area is located in Mygdonia Basin, northern Greece. It has a typical Mediterranean climate with a mean annual rainfall of 496 mm for the period of 2015-2022, while the minimum and maximum values observed were 391 mm and 550 mm, respectively. The temperature varies from 11.9 ˚C to 20.6 ˚C with a mean annual temperature of 15.8 ˚C (data from meteo.gr). From a geotectonic perspective, the basin includes two major structural zones: the central and eastern parts are associated with the Serbo-Macedonian Massif, while the western region, where the study area is located, belongs to the Circum Rhodope Belt (Meinhold and Kostopoulos, 2013). The geological substratum comprises Paleozoic two-mica gneisses and amphibolites of the Serbomacedonian Massif, along with Mesozoic phyllites, quartzites, clay-schists, marbles, and granites of the Circum Rhodope Belt (Mountrakis *et al*., 2006). Neogene deposits, primarily red clays, overlay these bedrock formations, with extensive Quaternary materials, including sandy clays, sands, and gravels, dominating the geological formations of the area (Figure 1). The study site is hydrologically divided into two sub-catchments: Koronia sub-basin and Volvi sub-basin. The study area belongs to the 10th Water District of Greece (GR10) and mainly falls within the Cholomontas – Oraiokastro and Koronia Groundwater Systems. According to the second revision, the qualitative and quantitative status of the Koronia Groundwater System is characterized as poor. The aquifer systems in the basin exhibit considerable heterogeneity, with alluvial deposits hosting both shallow unconfined and deeper confined aquifers, while fractured rock aquifers with variable permeability are found within the metamorphic formations (Mylopoulos *et al*., 2007; Devlioti *et al*., 2023).

This complex geological and hydrogeological setting highlights the importance of the Mygdonia Basin as a critical area for tracing nitrate sources in groundwater. The land use in the study area, based on the data from the Corine land cover, is provided in pie diagrams of Figure 2. Based on these data the landscape is primarily allocated to agriculture, with moderate forest coverage and limited urban and industrial development. Agricultural land is the dominant land use, with non-irrigated arable land constituting the largest portion (62%), followed by complex cultivation patterns (26%). Forested areas are primarily broad-leaved forests (45%) and coniferous forests (42%), with smaller contributions from natural grassland and other vegetation types. Artificial surfaces cover the minimum part of the study area and are mainly composed of discontinuous urban fabric (41%) and industrial or commercial units (27%).

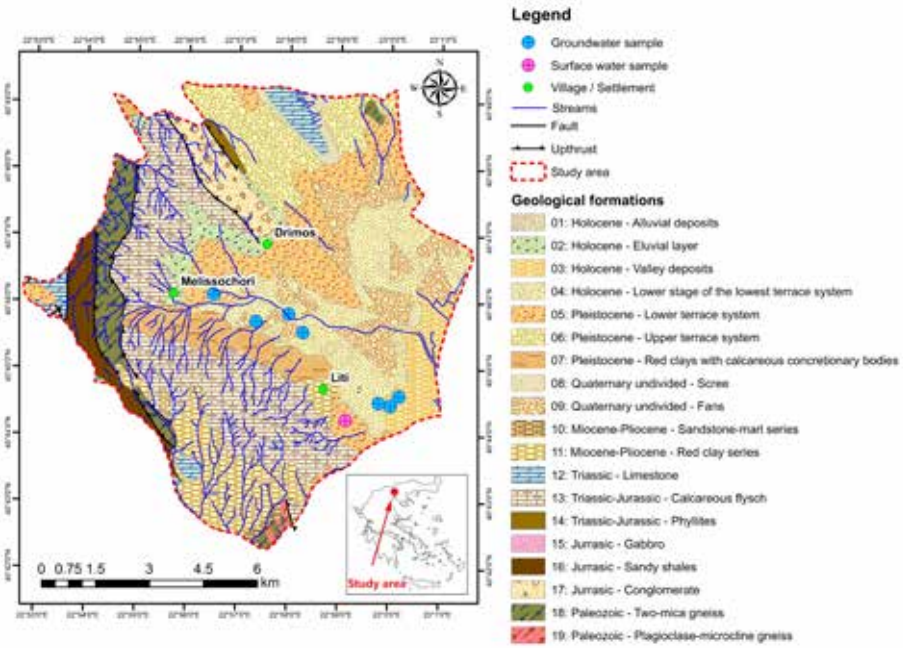

Figure 1. Study area with the groundwater and surface water sampling points.

Methodology

Groundwater and surface water samples were collected from the Mygdonia Basin during two field campaigns conducted in June and September 2023. Sampling locations were strategically selected following a judgmental sampling approach, as described by Ntona *et al.* (2023). The collected samples were analyzed to determine the concentrations of major ions and to perform stable nitrate isotope analyses of $\delta^{15}N\text{-}NO_3^-$ and $\delta^{18}O\text{-}NO_3^-$. Prior to collection, the sampling equipment was thoroughly cleaned with distilled water. Groundwater samples were collected from the well monitoring points and filtered through 0.45 μm filters to remove particulates. The filtered samples were then divided into aliquots, for isotopic analysis. The isotopic data was analyzed to distinguish between different nitrate sources, including synthetic fertilizers, animal manure, and organic matter decomposition. The chemical analyses of water samples were conducted by a private laboratory. The nitrogen isotopes in water ($\delta^{15}N$ and $\delta^{18}O$) were measured in the Isotopic Biotechnology Laboratory of the University of Ghent.

Results and discussion

The results of the chemical and isotope analysis provide important information to understand and investigate the hydrogeological regime of the groundwater in the study area. The water samples have been categorized in various diagrams providing their suitability for human consumption and irrigation purposes. Based on the Durov (Durov, 1948) diagram (Figure 3a), specifically in the square section, in most samples the predominant ions are HCO_3^- and Ca^{2+}, usually indicating rapid water recharge. The rest of the samples plotted higher with primary ions Ca^{2+} and Mg^{2+}, are due to the ion exchange processes. Referring to the Piper diagram (Piper, 1944), in the anion triangle, all samples are concentrated in the HCO_3^- section, while in the cation triangle, all groundwater samples are projected towards Ca^{2+} and the surface water samples have no dominant type (Figure 3b). Most samples are characterized as Ca^{2+}-Mg^{2+}-HCO_3^- water type, while the surface water sample collected in June is separated from the rest samples with higher concentrations of sodium compared to calcium.

The EC values of the same sample vary from 837 to 880 μS/cm, while the pH is 8.1 in the sampling periods. Regarding the suitability of water bodies for irrigation purposes, the Wilcox (Wilcox, 1995) diagram (Figure 4a) was used, which depends on the sodium percentage against electrical conductivity, and indicated that water is of good to permissible quality for irrigation, while only one groundwater sample collected in September showed good to excellent quality. In addition, Richard's plot (Richards, 1954) (Figure 4b) was applied to classify water samples in terms of the degree to which they can cause difficulty in the permeability of soils and the infiltration process, based on their electrical conductivity and the sodium adsorption ratio. Most samples are classified as high salinity hazard and low sodium hazard, indicating that the water

quality is medium and not suitable for semi-tolerant crops (Jafar Ahamed, 2013). Some samples collected in September are categorized as having medium salinity hazard and low sodium hazard, which means they do not require special measures for managing salinity.

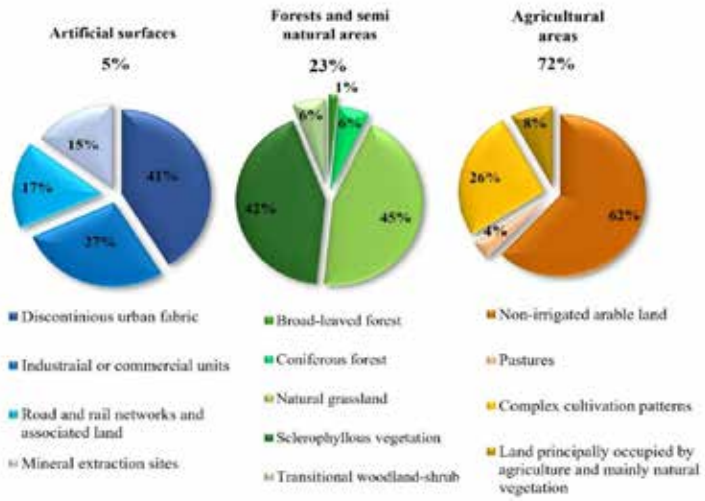

Figure 2. Pie diagrams with the percentages of land use in the study area.

The results of the physicochemical analyses (Table 1 and Table 2) on the samples showed that the pH values in June 2023 ranged from 7.3 to 7.7 and in September 2023 from 7.4 to 7.7 characterizing the groundwater as neutral to alkaline. Electrical conductivity (EC) varies from 831.0 to 1315.0 μS/cm and 734.0 to 1315.0 μS/cm during wet and dry periods, respectively. It is noted that the wider area is characterized by the presence of geothermal fields (Chantzi and Dotsika, 2016).

Nitrate concentrations for the two sampling periods showed a range from 47.8 mg/L to 154.0 mg/L in June and from 49.3 mg/L to 208.0 mg/L in September. The average concentration increased from 100.9 mg/L in June to 128.6 mg/L in September, representing a 27.5% rise.

In addition, almost all samples exceeded the permissible limit of nitrate concentration in drinking water (50 mg/L), with the exception of two samples, one for each period, which are quite close to this limit. With regard to the remaining nitrogen species, NH_4^+ appeared in all the samples with values lower than the detection limit of 0.06 mg/L, while NO_2^- concentration values were below the detection limit of 0.03 mg/L in almost all samples, with maximum values of 0.3 mg/L and 0.1 mg/L for June and September, respectively.

Land use data and field surveys highlight several potential anthropogenic sources of nitrate, including the extensive application of fertilizers, both manure and chemical types, as well as sewage effluent and solid waste disposal practices. To enrich the current results, the dual nitrate isotopes have also been utilized to investigate the contributors of nitrate pollution in the study area (Table 3). The dual nitrate isotope cross-plot diagram (Figure 5) serves as a key analytical tool for identifying the predominant nitrate sources.

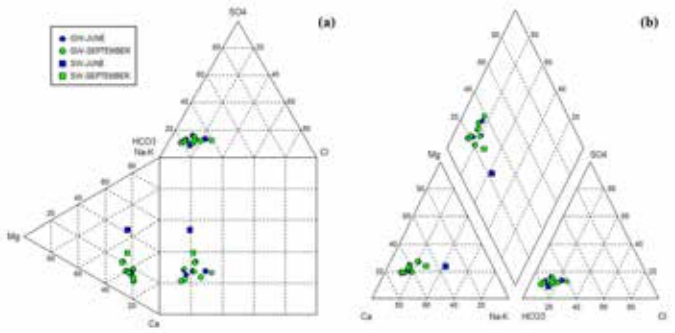

Figure 3. Classification of samples in Durov (a) and Piper (b) diagrams.

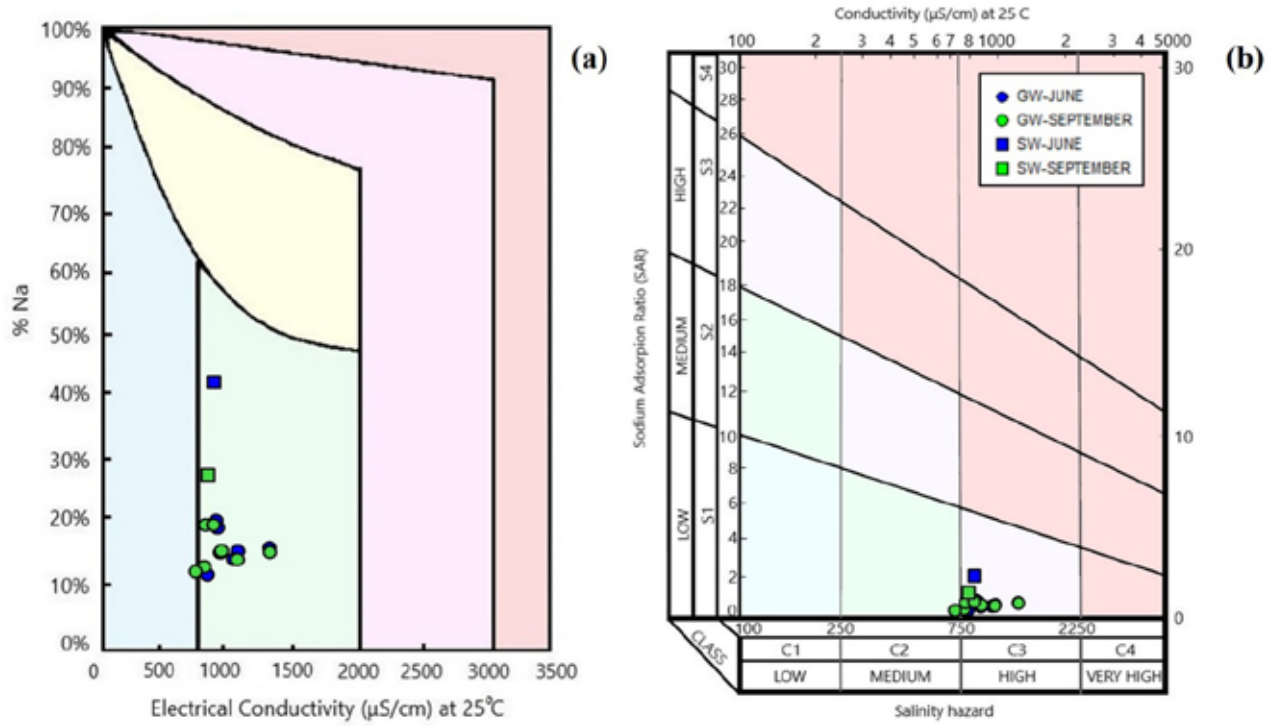

Figure 4. Classification of samples in Wilcox (a) and SAR (b) diagrams.

Table 1. Statistical analysis of the groundwater samples during the wet period of 2023.

Parameter	EC	pH	Ca^{2+}	Mg^{2+}	K^{+}	Na^{+}	NO_3^-	SO_4^{2-}	Cl^-	HCO_3^-
Values	µS/cm		mg/L	mg/L	mg/L	mg/L	mg/L	mg/L	mg/L	mg/L
Minimum	831.0	7.3	104.0	20.1	0.6	23.2	47.8	39.3	21.6	375.0
Average	998.0	7.5	131.1	28.6	0.9	39.3	85.1	58.0	48.6	408.4
Maximum	1315.0	7.7	164.0	39.3	1.5	50.3	154.0	77.7	88.8	437.0
St. Deviation	149.4	0.2	19.66	6.3	0.3	8.4	35.89	12.3	22.7	25.7

Table 2. Statistical analysis of the groundwater samples during the dry period of 2023.

Parameter	EC	pH	Ca^{2+}	Mg^{2+}	K^{+}	Na^{+}	NO_3^-	SO_4^{2-}	Cl^-	HCO_3^-
Values	µS/cm		mg/L	mg/L	mg/L	mg/L	mg/L	mg/L	mg/L	mg/L
Minimum	734.0	7.4	110	19.6	0.5	24.0	49.3	37.7	22.4	375.0
Average	934.0	7.5	136.9	29.0	0.9	39.6	100.7	57.3	53.2	414.3
Maximum	1315.0	7.7	187.0	41.7	1.2	53.7	208.0	74.4	112.0	442.0
St. Deviation	183.9	0.1	26.0	7.4	0.2	9.7	49.4	12.2	29.2	26.6

The results indicate that the majority of the groundwater samples fall within the isotopic range of manure and sewage nitrate sources, as the primary contributors to nitrate pollution in the Mygdonia Plain aquifer. In contrast, chemical fertilizers and soil organic nitrogen were found to play a key role in sample OR1.

The source identification of pollutants such as nitrate constitute the first step for the detection of unaffected aquifer layers. It is obvious that in the study area, chemical fertilizers and manure were excessively used neglecting the protection of groundwater. The upper layers of the aquifer are characterized by extensive nitrate pollution. The next step to secure the water supply for domestic use in the site is the isolation of these layers and pumping from deeper zones. Additionally, the assessment of groundwater vulnerability to nitrate pollution and pollution risk mapping constitutes a further step for water resource management and protection in the wider area of Mygdonia basin.

Table 3. Nitrate concentrations and isotopic composition of groundwater samples.

Sample	$d^{15}N\text{-}NO_3$	$d^{18}O\text{-}NO_3$
	‰	‰
OR1	5.6	3.5
OR2	11.2	4.0
OR3	9.9	3.5
OR4	8.4	4.0
OR5	9.9	3.8
OR6	9.90	3.70
OR7	8.60	4.40

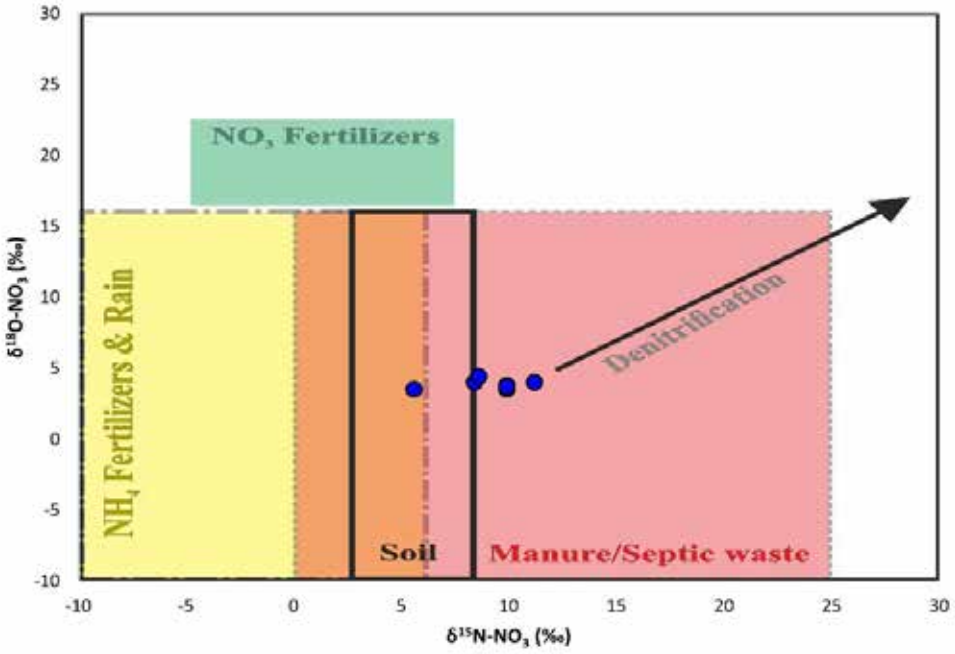

Figure 5. Cross plot of $\delta^{18}O\text{-}NO_3$ and $\delta^{15}N\text{-}NO_3$ of groundwater samples (Kendall, 1998).

Conclusions

This research provides a robust basis for tracing nitrate sources and enhances understanding of groundwater nitrate pollution in the Mediterranean region. The groundwater and surface water samples were collected during June and September 2023, revealing nitrate concentrations that reached up to 154.0 mg/L and 208.0 mg/L, respectively. Using stable nitrate isotopes on groundwater samples plotted on a Kendall diagram, nitrate sources were identified. The main nitrate pollution sources in the Mygdonia Plain aquifer are due to manure and sewage. The hydrochemical analysis of groundwater samples and the plot of water samples on the Piper diagram reveals the Ca^{2+}-Mg^{2+}-HCO_3^- water type of samples.

Further investigation into the role of the geothermal fields on groundwater quality should be implemented in the wider area. Management strategies to mitigate nitrate pollution from these identified sources and protect groundwater quality in the area are of paramount importance. This requires a systematic and continuous monitoring of groundwater quality in Mygdonia Basin.

Acknowledgments

This research was carried out within the framework of the project entitled “Water resources research and nitrate origin in groundwater of the Municipal Unit of Mygdonia” and was funded by the Water and Sewage Management Company of Oraiokastro (DEYAO).

References

Jafar Ahamed, A., Ananthakrishnan, S., Loganathan, K., Manikandan, K., 2013. Assessment of groundwater quality for irrigation use in Alathur Block, Perambalur District, Tamilnadu, South India. Applied Water Science 3, 763-771.

Chantzi, P., Dotsika, E., 2016. Mygdonia Basin (N. Greece) in the view of Isotope Geochemistry. In Energy, Transportation and Global Warming, Green Energy and Technology (Grammelis, P., Ed.). Springer International Publishing: Cham, Switzerland. https://doi.org/10.1007/978-3-319-30127-3_49.

Daskalaki, P., Voudouris, K., 2008. Groundwater quality of porous aquifers in Greece: a synoptic review. Environmental Geology 54, 505-513.

Devlioti, K., Mattas, C., Kaklis, T., Voudouris, K., 2023. Groundwater quality analysis in Mygdonia basin, Greece. Proc. of the 7th International Electronic Conference on Water Sciences (ECWS-7), MDPI (Ed. Loukas, A.), 2023, 25, 45, 313-319.

Durov, S.A., 1948. Natural Waters and Graphic Representation of Their Composition. Doklady Akademii Nauk SSSR, 59, 87-90.

Kazakis, N., Matiatos, I., Ntona, M.M., Bannenberg, M., Kalaitzidou, K., Kaprara, E., Mitrakas, M., Ioannidou, A., Vargemezis, G., Voudouris, K., 2020. Origin, implications and management strategies for nitrate pollution in surface and ground waters of Anthemountas basin based on a δ15N-NO3− and δ18O-NO3− isotope approach. Science of the Total Environment 724, 138211.

Kendall, C., 1998. Tracing nitrogen sources and cycling in catchments, in: Kendall, C., McDonnell, J.J. (Eds.), Isotope Tracers in Catchment Hydrology, 519–576.

Meinhold, G., Kostopoulos, D., 2013. The Circum-Rhodope Belt, northern Greece: Age, provenance, and tectonic setting. Tectonophysics 595-596, 55-68.

Mountrakis, D., Tranos, M., Papazachos, C., Thomaidou, E., Karagianni, E., Vamvakaris, D., 2006. Neotectonic and seismological data concerning major active faults, and the stress regimes of Northern Greece. Geological Society, London, Special Publications 260, 649-670.

Mylopoulos, N., Mylopoulos, Y., Tolikas, D., Veranis, N., 2007. Groundwater modeling and management in a complex lake-aquifer system. Water Resources Management 21, 469-494.

Ntona, M.M., Chalikakis, K., Busico, G., Mastrocicco, M., Kalaitzidou, K., Kazakis, N., 2023. Application of Judgmental Sampling Approach for the Monitoring of Groundwater Quality and Quantity Evolution in Mediterranean Catchments. Water 15, 4018.

Piper, A.M., 1944. A graphic procedure in the geochemical interpretation of water-analyses. Eos, Transactions American Geophysical Union 25, 914-928.

Raptakis, D.G., Manakou, M.V., Chávez-García, F.J., Makra, K.A., Pitilakis, K.D., 2005. 3D configuration of Mygdonian basin and preliminary estimate of its site response. Soil Dynamics and Earthquake Engineering 25, 871-887.

Richards, L.A., 1954. Diagnosis and Improvement of Saline Alkali Soils, Agriculture, 160, Handbook 60. US Department of Agriculture, Washington DC.

Wilcox, L.V., 1995. Classification and use of irrigation waters. Washington, USA Department of Agriculture, pp. 19.

17th INTERNATIONAL CONGRESS of the Geological Society of Greece

BULLETIN OF THE GEOLOGICAL SOCIETY OF GREECE, SP. PUBL.

EXTENDED ABSTRACT 147

Micropaleontological and paleoenvironmental study of carbonate intercalations within Boeotia (Greece) clastic formations

Khan S.A[1,2], Tsourou Th.[1], Skourtsos E.[1], Soukis K. [1], Michailidis I.[1], Skampa E.[1], Triantaphyllou M.V.[1]

(1) National and Kapodistrian University of Athens, Department of Geology and Geoenvironment, Athens, Greece, mtriant@geol.uoa.gr (2) Department of Earth Sciences, University of Lille 1, Villeneuve d'Ascq, France

This study aims to define the age and the paleoenvironmental depositional conditions of various carbonate facies within the Western Boeotia-Thessaly Unit in the broader area of Boeotia, central Greece, through the integration of calcareous nannofossil biostratigraphy and sedimentary microfacies analysis.

The existence of an Upper Jurassic–Lower Cretaceous "flysch" spread across multiple paleogeographic regions, both neritic and pelagic, is the main distinctive characteristic of the Western Thessaly–Boeotia unit that belongs to the outermost part of the Internal Hellenides (Papanikolaou, 2013; Papanikolaou, 2021).

The study area (Figure 1) is comprised of the outcrops of the Western Thessaly-Boeotia and the Parnassos units in Central Greece. The Western Thessaly–Boeotia, Late Jurassic–Early Cretaceous Boeotian flysch is followed by Late Cretaceous pelagic breccia limestones of the Thymiama facies, in contrast to the other more internal units, which remain below the Late Cretaceous transgression (e.g., Papanikolaou, 2021). The investigated successions are mainly composed of carbonate intercalations within the clastic sequences of the Boeotian flysch and the limestone of Thymiama. A selection of samples has been analyzed for the present research (Historical Geology and BioGeosciences Laboratory; National and Kapodistrian University of Athens), representing the carbonate intercalations and/or carbonate sequences from the various geological units and facies defined in the fieldwork campaign. Emphasis has been attributed to the calcareous nannofossil biostratigraphic assignment of the sampled clastic sequences (Figure 2).

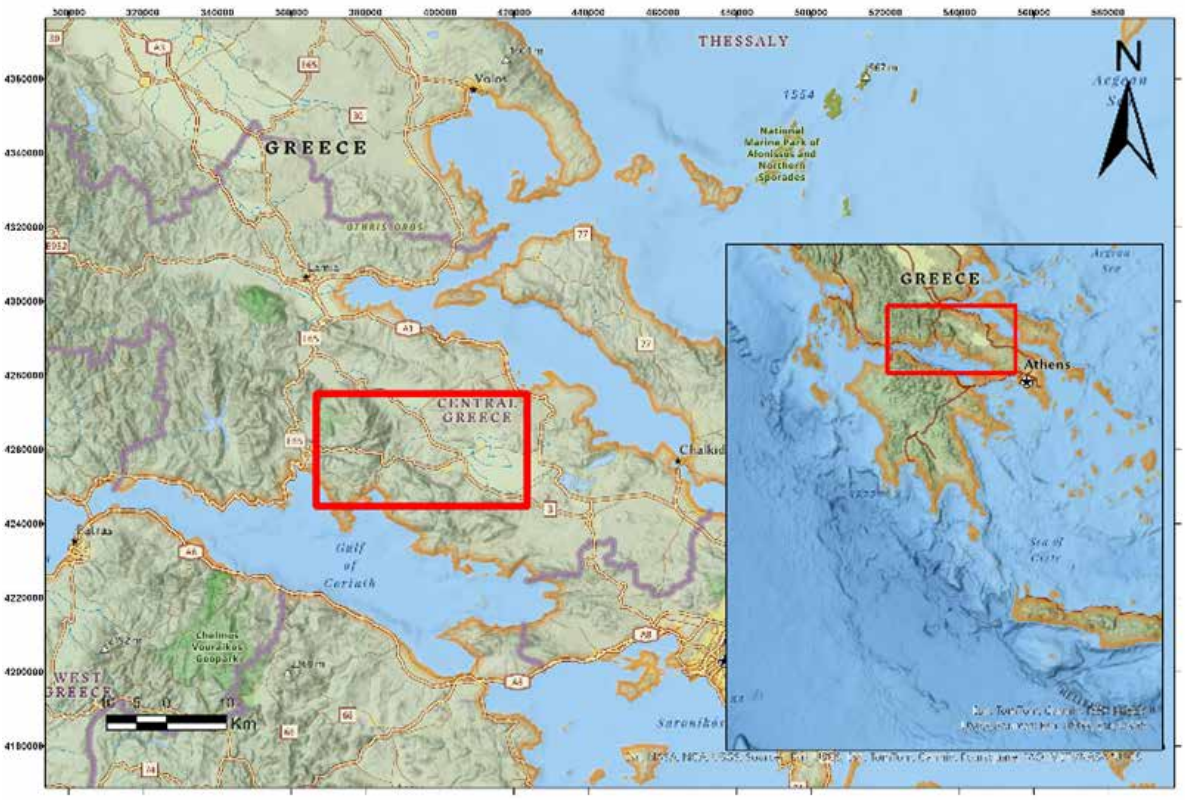

Figure 1. Location map of the study area in Central Greece.

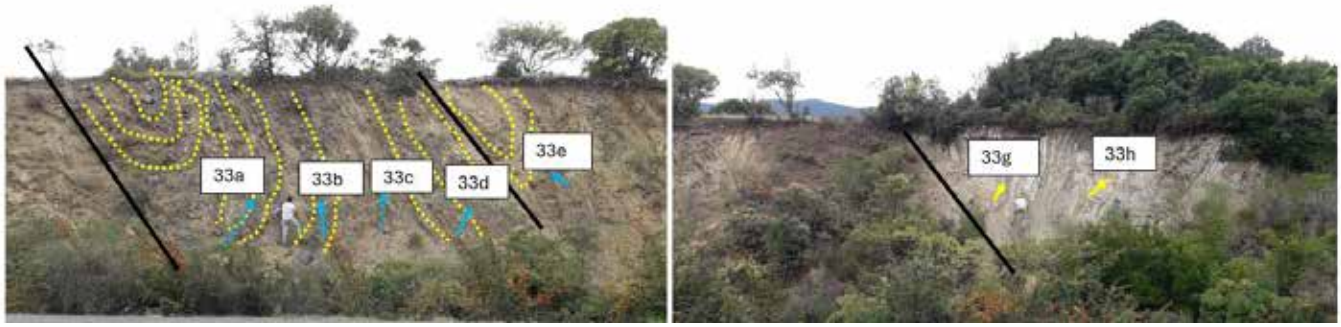

Figure 2. Studied outcrop showing the carbonate intercalations within the clastic sequences of the Boeotian flysch in Karakolithos section.

The nannofossil-based biostratigraphy performed in the clastic sequences being either intercalated or in contact with the studied carbonate samples, suggests that the samples from the Boeotian flysch are of Early Cretaceous age (Berriasian-Valanginian up to Aptian; Nirta et al., 2015; present study). The intercalated carbonate sequences of the Early Cretaceous age Karakolithos section comprise of pelagic biota. Based on the microfacies details, the sediments of the Boeotian flysch have been deposited in toe-of-slope to deep shelf setting in low-energy conditions (FZ-2 and FZ-3). This is evident by the intense presence of radiolarian and planktonic foraminifera within pelagic lime mud.

The Thymiama limestones in Boeotia represent reworked sediments from a reef or platform-derived environments as evidenced by rudist fragments and echinoderms. These have been transported during multiple sedimentary cycles and were redeposited to deeper settings (FZ-4), i.e., a low-energy gradient slope setting, also supported by the occurrence of Orbitolinidae. The nannofossil-based biostratigraphic results from marly intercalations within the Thymiama-type brecciated limestones suggest Turonian age. Also, the Aptian-Cenomanian has been identified in other locations, supporting an overall Aptian-Turonian age for the Thymiama limestones in the Boeotia area.

References

Nirta, G., Moratti, G., Piccardi, L., Montanari, D., Catanzariti, R., Carras, N., Papini, M., 2015. The boeotian flysch revisited: New constraints on ophiolite obduction in central Greece. Ofioliti 40(2), 107–123. https://doi.org/10.4454/ofioliti.v40i2.438

Papanikolaou, D., 2013. Tectonostratigraphic models of the Alpine terranes and subduction history of the Hellenides. Tectonophysics
595–596, 1–24.

Papanikolaou, D. I., 2021. Regional Geology Reviews The Geology of Greece. http://www.springer.com/series/8643.

17th INTERNATIONAL CONGRESS of the Geological Society of Greece

BULLETIN OF THE GEOLOGICAL SOCIETY OF GREECE, SP. PUBL.

EXTENDED ABSTRACT 148

" Vikos-Aoos Geopark: Toponyms as a Link Between Geological Heritage and Culture"

Georgia Kitsaki[1], Christos Stergiou[2], Haritakis Papaioannou[3]

(1) Vikos-Aoos UNESCO Global Geopark - Development Agency of Epirus S.A. (EPIRUS S.A.), Ioannina, Greece, gkitsaki@epirussa.gr (2) Stergiou C.L., Faculty of Geology, Aristotle University of Thessaloniki (AUTH), Thessaloniki, Greece / Vikos-Aoos UNESCO Global Geopark, Ioannina, Greece (3) Vikos-Aoos UNESCO Global Geopark - Development Agency of Epirus S.A. (EPIRUS S.A.), Ioannina, Greece

The Vikos-Aoos Geopark serves as a unique example of the interaction between geological formations, the natural environment, and culture, highlighting the enduring relationship between geological heritage and human activity. The region's geodiversity, characterized by designated geosites and a wide variety of geological formations, provides evidence of long-term geodynamic processes that have significantly shaped local ecosystems and biodiversity. At the same time, these geological features have been utilized by local communities, contributing to the development of a biocultural heritage, where the geoenvironment and human activity have jointly shaped the landscape and cultural identity of the area.

The integration of the geological environment into the daily lives of local communities extends beyond the mere exploitation of natural resources, such as the use of rocks in traditional architecture. Instead, it is deeply embedded in the toponymic tradition, the process by which geographical features are named, allowing communities to attribute distinct characteristics and meaning to the landscape. Toponyms are not merely linguistic data; rather, they function as carriers of valuable information across multiple disciplines, including history, archaeology, geology, and folklore. Geology, by examining the gradual transformations of the Earth's surface, contributes to the understanding of geographic and cultural migrations of populations, as well as the selection of specific sites for human settlement. Meanwhile, folklore studies investigate how toponyms encapsulate religious beliefs, local traditions, and ritual practices, establishing a profound connection between inhabitants and their natural surroundings, transforming the landscape from a natural into a humanized space.

Research Methodology and Objectives

The present research aims to identify and highlight examples that demonstrate the dynamic relationship between geological formations and human activity, illustrating the connection between geological heritage and cultural identity. Additionally, it seeks to enhance the participation of local communities in the management and promotion of the Vikos-Aoos Geopark, recognizing the significance of local knowledge in preserving both natural and cultural heritage. To collect, analyze, and interpret data, a qualitative research methodology was applied, aiming at an in-depth investigation of experiences and social processes related to the region's geological heritage. Data collection techniques included:

- Literature review and content analysis of scientific and historical sources.
- Interviews with local residents of the Geopark to document local perceptions and oral traditions.
- Participant observation through field research in locations of particular geological and cultural interest.

As part of the field research, studies were conducted in the community of Pyrgos in Konitsa, where an on-site visit was carried out with its President, Mr. Christos Papadimitriou, and in the village of Laista in Zagori, where data was collected in collaboration with the President of the Laista Mountaineering Association, Ms. Toula Poala.

Findings and Conclusions

Preliminary research findings indicate that the Vikos-Aoos Geopark hosts numerous locations of significant geological interest and designated geosites that have been incorporated into the collective memory of local communities through toponymic tradition. Notable examples include "Nterti", "Vrachos tou Chodza" ("Hodja's Rock"), "Kokkino Lithari" ("Red Rock"), as well as the well-known Dragon Lakes of Smolikas and Tymfi. These findings suggest that diverse geological formations—ranging from steep cliffs to crystalline springs—have acquired profound significance for local populations, becoming an integral part of their cultural heritage.

This exploration of the interplay between geology and culture underscores that geology is not merely a science that interprets the Earth's past but also a bridge to sustainable development and cultural empowerment. The Vikos-Aoos Geopark serves as a living example of the intricate relationship between the natural environment and human activity, emphasizing the need for holistic approaches in the management and promotion of geological heritage.

Prospects and Management of Geocultural Heritage

The management of the region's geocultural heritage aligns with the principles of UNESCO, fostering the systematic

interpretation of geological and cultural heritage while promoting sustainable development. Strengthening the connection between humans, nature, and culture through the management of the Vikos-Aoos Geopark is a priority, ensuring the preservation of the geological and cultural elements that make the area unique.
Thus, understanding the relationship between geological structures and cultural practices not only contributes to scientific knowledge but also plays a crucial role in reinforcing local identity and ensuring the sustainable development of the region.

References

Toponymy of Zagori, Konstantinos Ev. Oikonomou, Ph.D. Dissertation, University of Ioannina, 1986
Toponymics, N.G. Politis, P.D. Sakellariou Publications, Athens, 1914 and 1916
Our Toponyms: Their Value and Their Problems, Thomopoulos I., Thessaloniki, 1958
Toponyms & Oikonyms of the Mason Villages of Konitsa: Documentation, Interpretation, Etymology, Comments, Ziogas Th., Athens, 2013
A Tree Spreads Its Branches, G. Poala, Laista Zagori Mountaineering Club, Ioannina, 2006
The Echoing Rock of Sellio and Stratiani, Soureli-Galani Eleni, Kaktos Publications, Athens, 2023
Miscellaneous Folklore Studies, Nitsiakos V., Odysseas Publications, 1997
Building Space and Time, Nitsiakos V., Odysseas Publications, 2003
The Kantsiotika", Informational and Cultural Publication of the Drosopigi Brotherhood, Issue No. 22, August 2015
Technical Report on the Geological Formations of the Vikos-Aoos UNESCO Global Geopark, EPIRUS S.A., Ioannina, 2023
Vikos-Aoos Geopark: Nature Narrates Its History, Papaioannou Ch. & Kitsaki G. (eds.), IPIROS S.A., Region of Epirus, 2014

17th INTERNATIONAL CONGRESS of the Geological Society of Greece

BULLETIN OF THE GEOLOGICAL SOCIETY OF GREECE, SP. PUBL.

EXTENDED ABSTRACT 149

A Duration Model for Strong Seismic Motions of Intermediate-Depth Earthquakes in the Southern Aegean and its implication for stochastic simulations

Kkallas Ch.[1], Papazachos C.[2], Margaris B.[3]
(1) Aristotle University of Thessaloniki, Thessaloniki, Greece, chkkalla@geo.auth.gr
(2) Aristotle University of Thessaloniki, Thessaloniki, Greece, kpapaza@geo.auth.gr
(3) Institute of Engineering Seismology & Earthquake Engineering (EPPO-ITSAK), Thessaloniki, Greece, margaris@itsak.gr

Introduction

The southern Aegean subduction zone experiences the highest active deformation rates along the entire Africa-Eurasia collision zone, accounting for over 60% of Europe's seismicity. The Aegean microplate is moving southwestward at an average velocity of ~35 mm/yr relative to Eurasia, while the nearly stalled Mediterranean-Nubian plate system moves slowly toward Europe at ~5 mm/yr (Reilinger et al., 1997; Papazachos et al., 1998; Papazachos, 1999; McClusky et al., 2000; Ganas and Parsons, 2009) (Figure 1). This subduction process of the Eastern Mediterranean lithosphere beneath the Aegean microplate leads to the presence of partial melt in the mantle wedge above the subducting slab. As a result, P and S waves from intermediate-depth earthquakes (depths >45-50 km) are strongly attenuated along the South Aegean volcanic arc, while body waves from in-slab events that propagate toward the outer Hellenic arc experience high-frequency amplification (Skarlatoudis et al., 2013). The attenuation of seismic wave energy observed in the recordings appears to affect the durations of their seismic records. The ground motion duration is usually defined using the segment of the seismogram corresponding to the 0% (or 5%) to 95% energy range, as determined by Husid plots (Husid, 1969). A typical example is presented in Figure 2 which shows the corresponding Husid durations at a back-arc station (KOSI) and along-arc station (KAPA) for the 09 July 2016 **M**4.6 intermediate-depth earthquake. As we can see from both plots, there is a notable difference in the duration between the back-arc and along-arc stations, with the back-arc region exhibiting longer durations compared to the along-arc stations. This variation highlights the influence of the geotectonic setting on seismic wave propagation and attenuation. In this study, we examine the variation of strong ground motion duration as a function of hypocentral distance for intermediate-depth earthquakes. Previous attempts to correlate epicentral distance with quantitative measures of recorded ground motion duration have been performed by several researchers (e.g. Papazachos et al., 1992; Koutrakis et al., 2002; Tselentis and Danciu 2008), using shallow earthquake data (typically h < 50 km) for the broader Aegean area. No such relationships have been proposed for intermediate-depth earthquakes, mainly due to the limited data available.

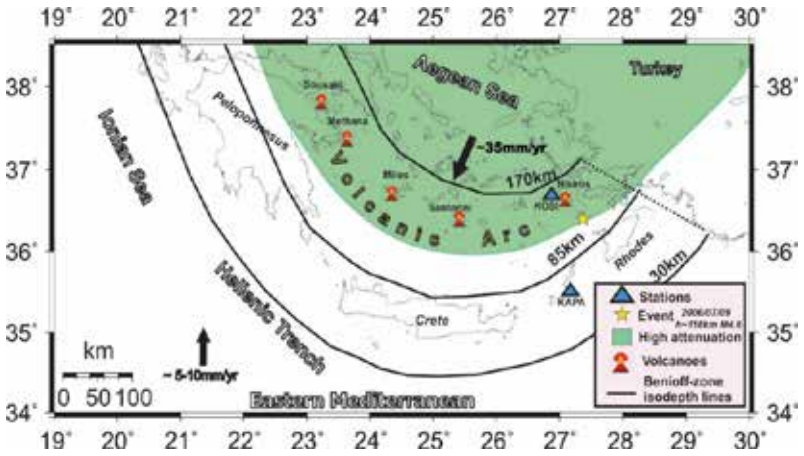

Figure 1. Schematic geotectonic map of the southern Aegean Sea subduction (southern Greece). Plate motions relative to stable Europe are shown with solid vectors. Indicative Benioff-zone isodepths are also indicated. The shaded area identifies the high-attenuation back-arc region (Skarlatoudis et al., 2013). We also present the 09 July 2006 M4.6 intermediate-depth earthquake with a yellow star, while the stations of Fig. 2 (KOSI and KAPA) are depicted with blue triangles.

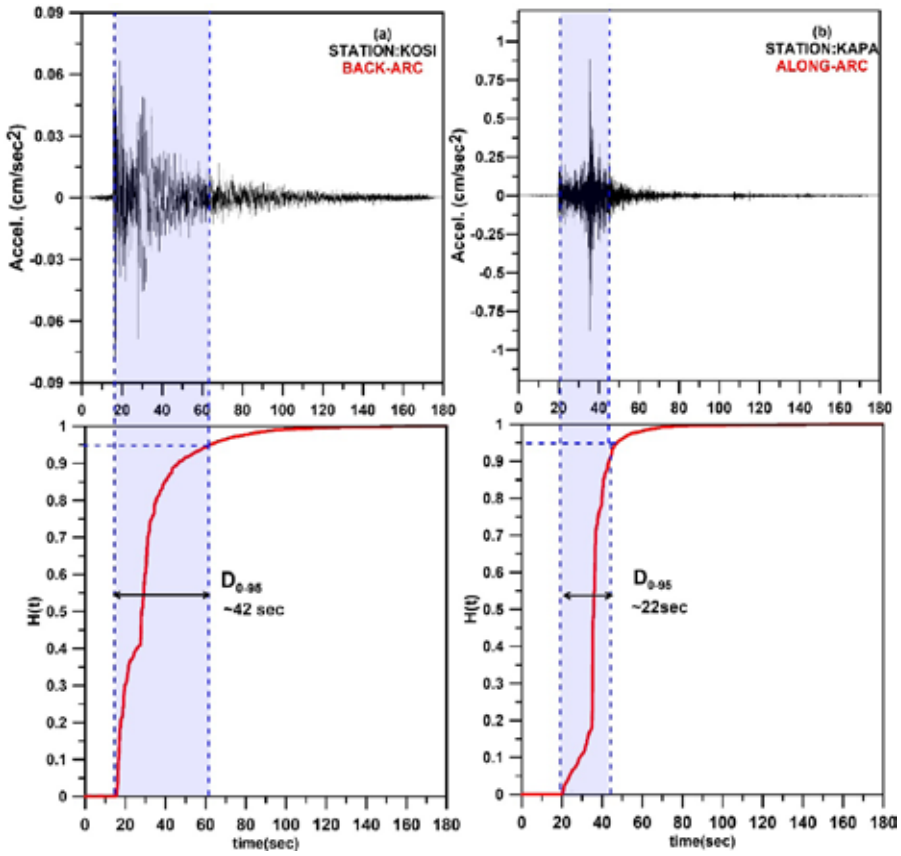

Figure 2. Husid duration for the 0%–95% range of the Arias intensity computed only for S-waves, for a back-arc station (KOSI) and a along-arc station (KAPA) [2006/07/09 M4.6 earthquake, h~118 km]. Although the stations are located at approximately the same epicentral distance, the back-arc station (KOSI) shows a significantly longer duration compared to the along-arc station (KAPA).

Data and method

We estimated the Husid duration for back-arc and along-arc area using a larger number of instrumental recordings based on previous works (Kkallas et al., 2018 and Skarlatoudis et al., 2013). Waveform data were collected and processed for the Southern Aegean subduction, providing the basis for a detailed study of the duration model, using information provided by horizontal components. To calculate the ground motion durations, we used waveform data from both acceleration and broadband-velocity sensor instruments for intermediate-depth earthquakes (depths >45km) with **M**4.5-6.7 that occurred along the southern Aegean Sea Wadati-Benioff zone. We considered the "significant" duration, as this was examined for the energy range 0% –95% of the Arias intensity of both P and S wavetrains. It should be noticed that the selection of 0% rather than the 5% often used refers to our choice to define a duration that starts exactly at the arrival time of the S (or P) waves, indicating the onset of the wave under study. We also excluded data from very large hypocentral distances (R^{hyp} > 450km), as the data for very large distances showed a very large scatter and corresponded to very small levels of ground motions.

Data from intermediate-depth earthquakes were analyzed and grouped into three categories based on their focal depths (≤60 km, 60–100 km, >100 km). This classification enabled us to quantitatively examine a possible correlation between S-wave durations and hypocentral distance. Figure 3a depicts a characteristic example, illustrating the spatial variation of Husid durations observed for the 09 July 2006 **M**4.6 intermediate-depth earthquake. Longer duration values are recorded in the back-arc region, at stations more than 100 km from the epicenter, driven by significant back-arc attenuation for events with depths >100 km. Figure 3b shows the variation of strong seismic motion duration, as defined by Husid diagrams, with respect to hypocentral distance. These differences are clearly due to the presence of the mantle wedge, characterized by a low Qs quality factor (Ventouzi et al., 2018), as well as low Vp and Vs velocities (Papazachos and Nolet, 1997), which primarily accounts for the strong attenuation of S-wave energy.

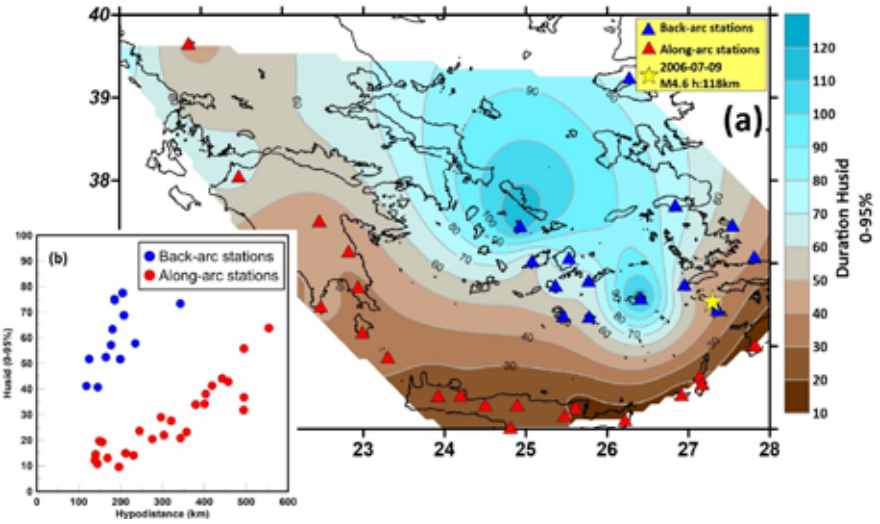

Figure 3. a) Spatial variation of the 0-95% Husid duration for S-waves for the 09 July 2006 M4.6 intermediate-depth earthquake, showing significant spatial variability between the outer Hellenic arc and the back-arc area. b) Variation of the same duration as a function of the hypocentral distance and back-arc/along-arc location of the recording station, showing a ~4 times larger durations for back-arc stations.

Figure 4 shows the variation of the strong motion duration, as defined by Husid diagrams, against the hypocentral distance for the three focal depth intervals (Figures 4a, 4b, 4c). Significant differences in the S-wave duration for earthquakes with focal depths greater than 100 km are identified between stations in the back-arc region and stations along the Hellenic Arc, leading to different linear regressions between duration and hypocentral distance (Figure 4d). This was not the case for shallower intermediate-depth events, where back-arc and along-arc stations exhibit rather similar durations.

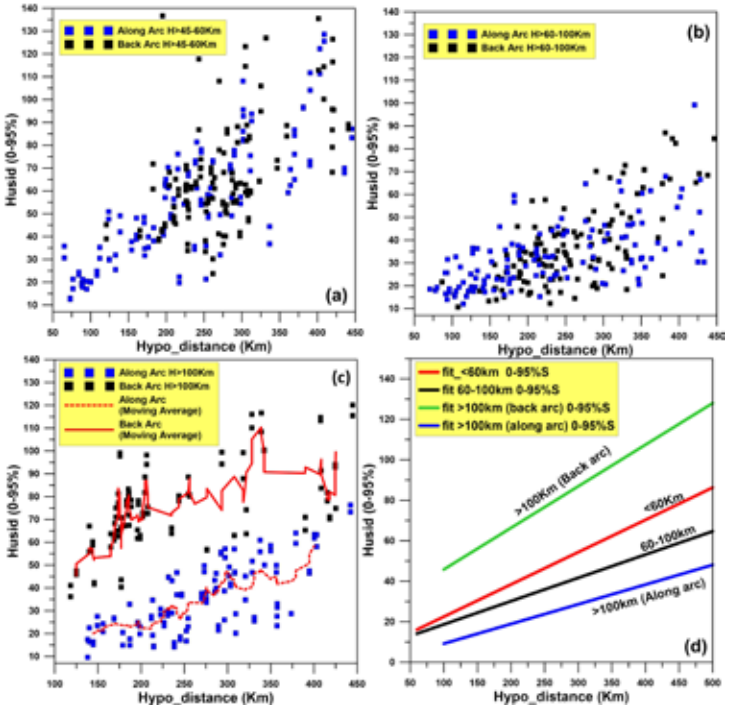

Figure 4. Variation of S-wave significant duration measures (Husid 0%-95%) with hypocentral distance for along-arc and back-arc seismic stations, categorized by depth: a) h≤60 km, b) h:60–100 km, c) h>100 km. d) Linear regression between duration and hypocentral distance for along-arc and back-arc stations, based on the depth classification.

The final relations regarding the duration of strong seismic motion (S-waves) are:

$$S-wave\ durarion(h,R_{hyp})=\begin{cases} if\ 45km \le h < 60km \\ 0.1594 * (R_{hyp}) + 6.5355 \\ if\ 60km \le h < 100km \\ 0.11493 * (R_{hyp}) + 7.1973 \\ if\ h \ge 100km \\ [Back-arc]\ \ 0.2053 * (R_{hyp}) + 25.293 \\ [Along-arc]\ \ 0.0972 * (R_{hyp}) - 0.53475 \end{cases} \quad (1)$$

It should be noticed that no magnitude term is included in the linear equations (1), which may appear rather strange, considering that the input data span a rather wide moment magnitude range (**M**4.5-6.7). However, attempts to simultaneously solve for both distance and magnitude terms using an appropriate linear formulation rendered a very weak dependance on moment magnitude, which is equivalent to a total difference of ~4 sec for the aforementioned magnitude range. Due to the very poor control on the magnitude effect on durations we decided to use the simple form of eq. (1), until a larger dataset is available for intermediate-depth events of the southern Aegean area. We should consider that eq. (1) corresponds to significant durations, which do not reflect the actual level of seismic motions, but rather the time interval within which the largest part of S-wave energy is released by the mainshock. As a result, it is expected that the event magnitude is less critical and that the duration increases with the coda envelope that critically depends on the hypocentral distance.
The results in eq. 1 can be employed in a stochastic simulation scheme to determine synthetic but realistic waveforms using the stochastic approach of Motazedian and Atkinson (2005), as adapted by Boore (2009), and implemented in the EXSIM algorithm. It is important to emphasize that EXSIM does not determine ground motion duration using peak-based or threshold-based criteria, such as the time interval during which acceleration exceeds a fixed value commonly referred to as “strong-motion duration.” Instead, EXSIM adopts a more physically meaningful approach by utilizing energy-based duration metrics, which are derived from Husid plots. These plots represent the cumulative energy of the ground motion over time, allowing the modeled duration to reflect the overall energy content of the seismic signal, rather than being influenced by isolated acceleration peaks or arbitrary thresholds. We used the method as adapted by Kkallas et al. (2018) for the southern Aegean Benioff zone. Moreover, we used the same approach to generate P-wavetrains, using the travel-time curves for intermediate-depth earthquakes of Ventouzi et al. (2013) to deternine the S-P duration, which we considered as the duration of longitudinal (P) waves. The final seismogram was created as the superposition of both P and S waveforms. A typical example is presented in Figure 5 for the 24 July 2015 **M**5.0 Nisyros earthquake (h=133 km). The waveforms (containing both P and S waves) from the stochastic simulation modeling are quite similar with the actual records for stations from both the along-arc (ARG) and back-arc area (VLY), suggesting that the employed duration model can be considered as realistic.

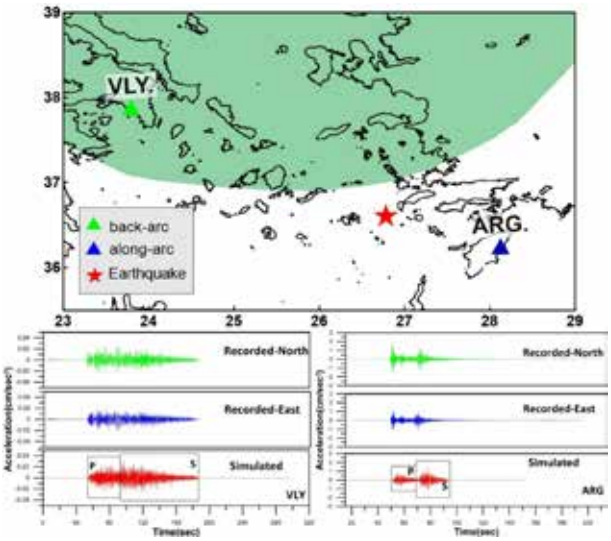

Figure 5. Synthetic acceleration waveforms (P and S waves) for back-arc and along-arc stations for the 24 July 2015 M5.0 Nisyros earthquake from stochastic simulation modeling. Notice the significant differences in the duration of strong ground motion time histories between the back-arc and along-arc stations, with the final composition of the waveforms (P and S waves) being in good agreement with the actual records for both stations (along-arc station ARG and back-arc station VLY).

Conclusions

The study of the strong seismic motion duration for intermediate-depth events of the Southern Aegean Benioff zone revealed that for earthquakes with depths greater than 100 km, the recording stations can be divided into two categories: stations along the external Hellenic Arc (along-arc) and stations in the back-arc region. Stations in the back-arc region exhibit records with longer Husid durations of seismic motion, though with low amplitudes due to the strong attenuation of S-waves caused by the presence of the mantle wedge beneath the volcanic arc. In contrast, records from stations along the Hellenic arc have significantly higher amplitudes and shorter Husid durations. On the contrary, events at shallower depths seem to have comparable significant durations for both back-arc and along-arc stations. It should be noted that this conclusion may seem counterintuitive at first, since it is known that the duration of strong seismic motions for intermediate-depth earthquakes is shorter at stations in the back-arc region compared to those in the along-arc region. However, by "duration", we define the time during which the motion accumulates the total energy of the seismic record, regardless of the level of seismic motion. Consequently, the low-amplitude back-arc records "delay" the accumulation of the total cumulative energy, leading (typically) to a longer strong duration. In contrast, records from stations along the external Hellenic Arc have significantly higher amplitudes (similar to those of shallow earthquakes), resulting in the rapid accumulation of a larger percentage of the energy in the record (shorter strong duration). As we demonstrate in this work, a simple distant-dependent duration model can be adopted and employed in stochastic simulation modeling, allowing the efficient reconstruction of wavetrains for intermediate-depth events in the Southern Aegean subduction zone. The observed weak dependence of duration on moment magnitude is most likely attributed to the limited dataset. Further clarification on the uncertainty quantification in linear regressions could be explored in the future once additional data becomes available, allowing to assess the actual influence of moment magnitude on duration.

References

Boore, D. M. (2009), Comparing Stochastic Point-Source and Finite-Source Ground-Motion Simulations: SMSIM and EXSIM, Bull. *Seism. Soc. Am*., 99(6), 3202-3216, doi:10.1785/0120090056

Ganas, A., Parsons, T., 2009. Three-dimensional model of Hellenic arc deformation and origin of the cretan uplift. Journal of *Geophysical Research: Solid Earth* 114.

Husid, L. R. "Características de Terremotos, Análisis General." Revista del IDIEM 8, Santiago, Chile, 1969: 21–42Kkallas, C., C. B. Papazachos, B. N. Margaris, D. M. Boore, Ch. Ventouzi, and A. Skarlatoudis (2018) Stochastic strong ground motion simulation of the southern Aegean Sea Benioff zone intermediate-depth earthquakes, *Bull Seismol Soc Am*, 108(2), 946-965

Koutrakis, S.I., P.K. Koliopoulos, G.F. Karakaisis, B.N. Margaris and P.M. Hatzidimitriou (2002). Seismic hazard in Greece based on different strong ground motion parameters, *Jour. of Earthquake Engineering*, 6, 75-109.

McClusky, S., Balassanian, S., Barka, A., Demir, C., Ergintav, S., Georgiev, I., Gurkan, O., Hamburger, M., Hurst, K., Kahle, H. and Kastens, K., 2000. Global Positioning System constrains on plate kinematics and dynamics in the eastern Mediterranean and Caucasus. *Journal of Geophysical Research: Solid Earth*, 105(B3), pp.5695-5719.

Motazedian, D., and G. M. Atkinson (2005), Stochastic Finite-Fault Modeling Based on a Dynamic Corner Frequency, *Bulletin of the Seismological Society of America*, 95(3), 995-1010, doi:10.1785/0120030207

Papazachos, B., E. Papadimitriou, A. Kiratzi, C. Papazachos, and E. Louvari, (1998). Fault plane solutions in the Aegean Sea and the surrounding area and their tectonic implications, *Boll. Geof. Teor. Appl*, 39(3), 199-218.

Papazachos, B.C., B.N. Margaris, N.P. Theodulidis and C. A. Papaioannou (1992). Seismic hazard assessment in Greece based on strong motion duration, *Proc. 10th Wor. Conf. Earthq*. Eng., Madrid, July 19-24, I, 425-430.

Papazachos, C. B. (1999). Seismological and GPS evidence for the Aegean□Anatolia Interaction. *Geophysical Research Letters*, 26(17), 2653-2656.

Papazachos, C., and G. Nolet (1997), P and S deep velocity structure of the Hellenic area obtained by robust nonlinear inversion of travel times, Journal of Geophysical Research B: *Solid Earth*, 102(B4), 8349-8367. **[**

Reilinger, R. E., S. C. McClusky, M. B. Qral, R. W. King, M. N. Toksoz, A. A. Barka, I. Kinik, O. Lenk, and I. Sanli (1997), Global positioning system measurements of present-day crustal movements in the Arabia-Africa-Eurasia plate collision zone, Journal of *Geophysical Research B: Solid Earth*, 102(B5), 9983-9999.

Skarlatoudis, A. A., C. B. Papazachos, B. N. Margaris, C. Ventouzi, and I. Kalogeras (2013), Ground-Motion Prediction Equations of Intermediate-Depth Earthquakes in the Hellenic Arc, Southern Aegean Subduction Area, *Bulletin of the Seismological Society of America*, 103(3), 1952-1968, doi:10.1785/0120120265.

Tselentis, G. A., and L. Danciu (2008), Empirical Relationships between Modified Mercalli Intensity and Engineering Ground-Motion Parameters in Greece, *Bulletin of the Seismological Society of America*, 98(4), 1863-1875, doi:10.1785/0120070172.

Ventouzi, C., Papazachos, C., Hatzidimitriou, P., Papaioannou, C., & EGELADOS Working Group. (2018). Anelastic P-and S-upper mantle attenuation tomography of the southern Aegean Sea subduction area (Hellenic Arc) using intermediate-depth earthquake data. *Geophysical Journal International*, 215(1), 635-658.

Ventouzi, C., Papazachos, C., Papaioannou, C. and Hatzidimitriou, P., 2013. Obtaining information on the Q-structure of the southern Aegean subduction area by spectral slopes from temporary and permanent networks. *Bulletin of the Geological Society of Greece*, 47(3), pp.1366-1375.

17th INTERNATIONAL CONGRESS of the Geological Society of Greece

BULLETIN OF THE GEOLOGICAL SOCIETY OF GREECE, SP. PUBL.

EXTENDED ABSTRACT 150

Lunar Pits: Statistical Analysis of Morphometric and Geophysical Properties

Klimis F.[1], Sykioti O.[2], Karymbalis E.[1], Parcharidis I.[1]

(1) Department of Geography, Harokopio University of Athens, Athens, Greece, gs219116@hua.gr (2) Institute of Astronomy, Astrophysics, Space Applications and Remote Sensing, National Observatory of Athens, Athens, Greece

Background and Objectives

Lunar pits are distinct geological features scattered across the Moon's surface that offer significant insights to the subsurface structure of the Moon, potentially indicating the existence of ancient lava tubes formed by volcanic activity. Lava caves or lava tubes are formed when the external part of the a lava flow cools more quickly and makes a hardened crust over the internal lava flow. As the lava flow drains out of the tube, it leaves an empty space. The thin part of the ceiling of lava tube could then collapse to expose the entrance to the lava tube which is called a pit (Haruyama et al., 2009; Robinson et al., 2012; Hong et al., 2014; Wagner & Robinson, 2014). They vary from a few meters to several hundred meters in diameter and display differing depths. Morphologically, these pits can be broadly categorized into two types: those with a direct vertical drop (shaft-like pits) and those that slowly narrow down like a funnel (Figure 1). Lunar pits are mostly identified in near crater impact sites and within maria (large basaltic plains formed by ancient volcanic activity). Much of the original volume of most pits is now filled with debris, but some exhibit significant overhangs and may have present-day cave access (Wagner & Robinson, 2022). As these formations may be linked to subsurface lava tubes, they are not only significant for understanding the geological history of the Moon but also for future lunar exploration, water ice detection and habitat development (Zu et al., 2024; Carrer et al., 2024). According to Horvath et al. (2022), lunar tubes and caves could provide a temperate, stable, and safe thermal environment for long term exploration and habitation. Although, the investigation of pits may be challenging due to steep slopes of loose material at their walls and floors, it could help clarify their formation mechanisms and their implications for the evolution of lunar volcanic and tectonic processes (Nesnas et al., 2023).

This study carries out a statistical morphometric and geophysical analysis of 278 currently observed lunar pits in order to detect and quantify their main attributes. A dataset of morphometric and geophysical measurements was collected in order to perform descriptive statistics and correlation analysis. The analysis is performed on a 2-point axis: (1) descriptive and correlation analysis of morphometric variables, (2) descriptive and correlation analysis of geophysical variables. The main conclusions of the analyses are presented proposing future directions for the continuation of this work.

Data and method

For the purpose of this study, morphometric and geophysical data issued from various satellite and topographic measurements of the lunar surface were collected. The main data source of the morphometric variables was the Lunar Reconnaissance Orbiter Camera Planetary Data System (PDS) archive. A detailed catalogue of 278 lunar pits containing geographical, topographical and morphological data was retrieved and utilized. The Catalogue of Lunar Pits receives updates as more pits are detected manually or by the Pitscan Algorithm developed by Wanger & Robinson (2022). According to Wagner & Robinson (2022), the up-to-date observed pits are 321. However, due to the unavailability of morphometric and geophysical variables of the newly recently detected lunar pits, in this study we used the 2021 pit catalogue that includes 278 pits. The main data source of the geophysical variables was the web platform Lunar QuickMap, implemented by the collaboration between NASA, Arizona State University and Applied Coherent Technology Corporation (https://quickmap.lroc.asu.edu/). Through the QuickMap platform (the platform employs the Wagner & Robinson (2022) pit catalogue), we retrieved the files containing the geophysical variables of 278 pits (example in Figure 2, variables in Table 1).

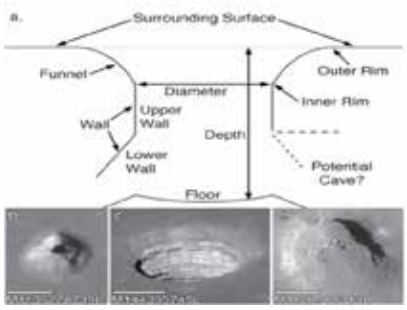

Figure 1. Cross-section of a generic lunar pit (Source: Wagner & Robinson, 2022). Not all pits exhibit all these features, or show these shapes. The inner rim is exaggerated for visibility.

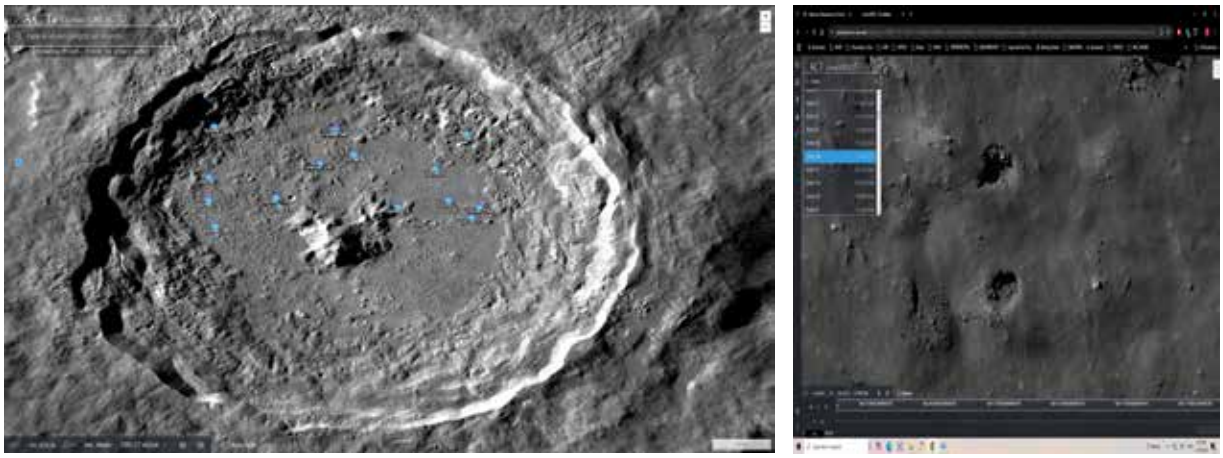

Figure 2. Tycho crater (formed 108 mya, Tycho crater has a diameter of 85km and is one among the thousands of similarly-sized craters on the Moon). Left image: screenshot featuring lunar pit locations within Tycho Crater using the QuickMap Platform (blue dots); Right image: zoom to pits Tycho 17a and Tycho 17b (located within the yellow circle in the left image). The left image scale is shown at the bottom right corner (10km) and the spatial resolution of the image is app. 100m/pixel. The spatial resolution of the right image is app. 0.6m/pixel.

All variables examined in this study are presented in Table 1. For the purpose of the morphometric statistical analysis, the variables were classified into two distinct categories, continuous and nominal variables. Statistical measures were used to provide a comprehensive understanding of the continuous variables, namely mean value, standard deviation, kurtosis and skewness. The Shapiro Wilk Test was also employed to evaluate whether the data follow a distribution. Correlation matrices were employed to determine the strength and correlation type (positive or negative) among pairs of variables such as funnel diameter, depth, slope measurements and terrain characteristics. The Jamovi open-source statistical software was utilized along with plug-ins of the R software in order to perform the correlation analysis. For the nominal variables, histograms were created to explore the distribution of categorical data, such as terrain type, host feature, and other binary indicators like the presence of an entrance ramp, overhangs, etc. Similar to the morphometric analysis, the geophysical analysis involved the use of descriptive statistics, distribution examination and correlation analysis.

Table 1. List of all morphometric and geophysical variables used in this study. The use of "?" shows the boolean character of the variable, meaning the presence or absence of a certain morphometric characteristic.

Morphometric continuous variables	Morphometric categorical variables	Geophysical continuous variables
Funnel max Diameter (m), Funnel min Diameter (m), Inner max Diameter (m), Inner min Diameter (m), Azimuth of the long axis of the inner pit (deg), Depth (m), SLDEM2015 (+LOLA) elevation (m), SLDEMDEM Slope (dynamic) (deg), SLDEM src Azimuth (deg), SLDEM src Slope (deg), Terrain Height (m), Terrain slope (deg)	Terrain type, Host feature, Geometry, Entrance Ramp ?, Overhangs ?, Nearby Pits ?, Nearby Fractures ?, Nearny Depressions ?, In Dome ?, In Depression ?, Colinear Pits ?, Colinear Depressions ?, Colinear Fractures ?, Is Copernical Crater ?, Is Mare ?, Is permanent shadow ?	Clinopyroxene abundance (wt%), FeO abundance (wt%), Olivine abundance (wt%), Orthopyroxene abundance (wt%), Plagioclase abundance (wt%), Thorium abundance (ppm), UVVIS FeO abundance (wt%), Nighttime soil temperature (normalized) (K), Nighttime soil temperature (K), Derived optical maturity (unitless), Diviner H-parameter (m), Rock abundance (unitless)

Results and Conclusions

Statistical analysis of pit morphometric characteristics

With the completion of the morphometric analysis, several key conclusions were drawn regarding the physical characteristics, geophysical context, and local distribution of lunar pits. The statistical results of the descriptive statistical analyses of the continuous variables (Table 1) are presented in Table 2 and examples of the distributions of pit continuous and nominal morphometric characteristics are presented in Figure 3.

Table 2. Results of the main descriptive statistical analysis of the continuous variables.

Variable	Number	Missing	Mean	Median	SD	Skewness	Kurtosis	Shapiro –Wilk
Funnel Max Diam	266	12	48.55	29.00	62.56	3.375	12.885	0.571
Funnel Min Diam	273	5	36.33	21.00	49.66	3.887	17.018	0.518
Inner Max Diam	266	12	31.00	16.00	48.78	4.328	21.931	0.483
Inner Min Diam	261	17	22.82	11.00	40.65	4.631	24.244	0.440
Azimuth	277	1	87.48	70.00	54.08	0.172	-1.364	0.927
Depth	237	41	13.15	9	13.89	3.310	13.072	0.609
SLDEM2015(+LOLA)(m)	278	0	-2008.63	-2293.34	1703.75	1.041	0.351	0.870

The results show significant skewness and kurtosis in both funnel and inner diameters, with the majority of pit dimensions ranging between 22 and 48 meters (Table 2 and Figure 3a). While most lunar pits are relatively shallow, with depths between 10 and 15 meters, there exists a subset of significantly deeper pits, indicating potential variations in formation processes or geological setting (Figure 3b). The azimuth analysis reveals a uniform distribution of pit orientations, suggesting no particular alignment or external directional influence in the formation of these pits (Table 2). Furthermore, the majority of lunar pits are found in impact melt terrains (mostly located within mare regions), and relatively few within mare and highlands (Figure 3c). This suggests a strong association between impact-related processes and pit formation. Many pits tend to cluster near other geological features, especially craters. This clustering suggests that pit formation may be influenced by nearby structural weaknesses, crustal thinning due to impacts or collapse processes related to crater formation. The study identified 28 distinct clusters of pits across various lunar regions. A significant number of pits (228 out of 278) are located near depressions, while very few are located within depressions. This distribution pattern could be related to crustal weakening in the broader area or subsurface voids influencing pit formation. Elevation data show that lunar pits are predominantly located in elevations well below the Moon's reference elevation sphere (Figure 3d).
Regarding the geometric variability, the majority of pits display undefined or elliptical or circular geometries with a variability that could be due to different collapse dynamics or variable composition of the host regolith (Table 3). Examining the overhangs, the presence of overhangs is observed only in a small percentage of lunar pits. Overhangs may be the result of mechanical weathering or collapse of pit walls due to gravitational forces. The majority of pits do not exhibit entrance ramps. Finally, no pits are observed in permanently shadowed regions of the Moon, which could be explained either by lack of data or by poor illumination conditions (e.g. areas of permanent shadow near the lunar poles and inside craters that are not directly illuminated by the sun).

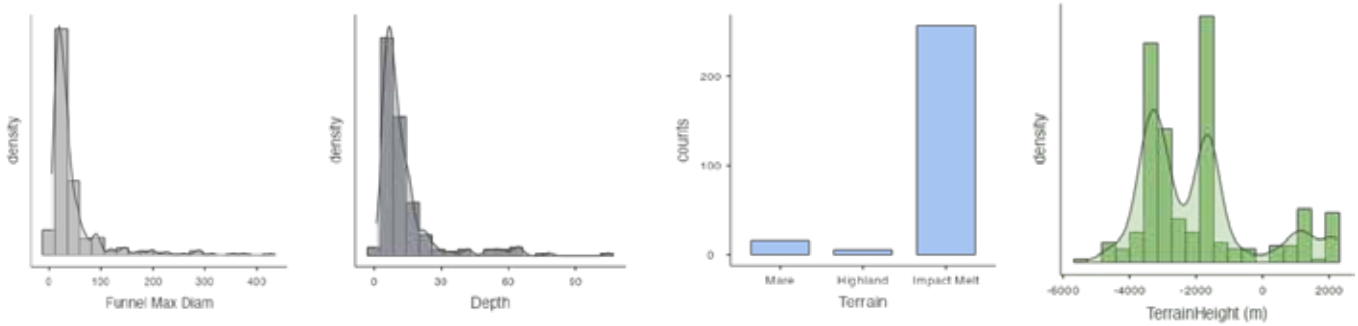

Figure 3. Examples of distributions of pit continuous and nominal morphometric variables: (a) funnel maximum diameter, (b) depth, (c) terrain type and (d) terrain elevation issued from LOLA DEM (elevation values are the distance above or below the reference sphere). Most of the pits show less than 10m funnel maximum diameter, they are rather shallow (10-15m) located in impact melts at altitudes well below the lunar reference elevation sphere.

Table 1. Most frequent pit geometries (shape) (occurrence >5% of total number of pits).

Geometry (shape)	Number of pits	% of total
Elliptical	52	18.7
Rectangular	21	7.6
Irregular	25	9.0
Triangular	19	6.8
Circular	38	13.7
Undefined	57	20.5

Concerning the linear correlation analysis, the first notable observation in the correlation matrix (Figure 4) is the strong relationship between pit dimensions. More specifically, Funnel Max Diameter and Funnel Min Diameter show a very strong positive correlation (Pearson's r = 0.94, p < .001). Similarly, both Inner Max Diameter and Inner Min Diameter show strong positive correlations with Funnel Max and Min Diameters (r > 0.9, p < .001), suggesting that the size of the inner pit is closely linked to the size of the outer funnel. Additionally, the strong positive correlation between Funnel Diameter and Inner Diameter (r > 0.7, p < .001) suggests that deep pits tend to present large diameters.

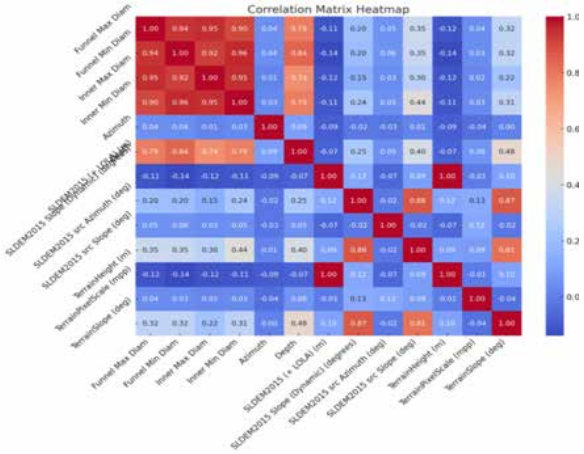

Figure 4. Correlation matrix between morphometric variables. The matrix is symmetric. The highest linear correlations are observed between the funnel diameter (man and min) and the inner diameter (max and min) of the pit.

Statistical analysis of pit geophysical characteristics

The results of the statistical analysis of the geophysical characteristics of the pit areas are in general consistent with the already known geological patterns on the lunar surface. In terms of mineralogy, maria, corresponding to secondary lunar crust formed by basaltic volcanism, exhibit the highest olivine, pyroxene (both clinopyroxene and orthopyroxene) content and the lowest content in plagioclase (32-35 wt%) (Figure 5a). Highlands, corresponding to the primordial lunar crust of anorthositic composition, present medium content in olivines and pyroxenes and a high content in plagioclase (anorthite) (62-65 wt%). Impact melts, corresponding to areas of intense cratering (where most of pits are located), present the lowest content in olivine and pyroxenes and the highest content in plagioclase (70-75 wt%). Correspondingly in terms of chemical composition, iron (Fe) and titanium (Ti) contents are high (15-17wt% and 2.5 – 3.5 wt% correspondingly) within maria pit areas, which are consistent with the maria basaltic compositions (Figure 5b). Highlands present relatively low Ti and Fe-content (7-10 wt%), which is expected due to the predominance of anorthositic rocks. Finally, pit areas within impact melts present the lowest Fe and Ti-content (7-10 wt%), which is consistent with their general low content in mafic minerals (olivines and pyroxenes). Concerning thorium (Th), it seems that maria and highland pit areas show higher Th content (3-3.5 ppm) than impact melts. Finally, impact melts present high rock abundances within regolith, low thermal intertia (0.03m) while they seem to retain higher nighttime soil temperatures (~ -271.15°C) compared to the maria and the highlands, reflecting thus a distinct thermal behavior (Figures 5c and d).

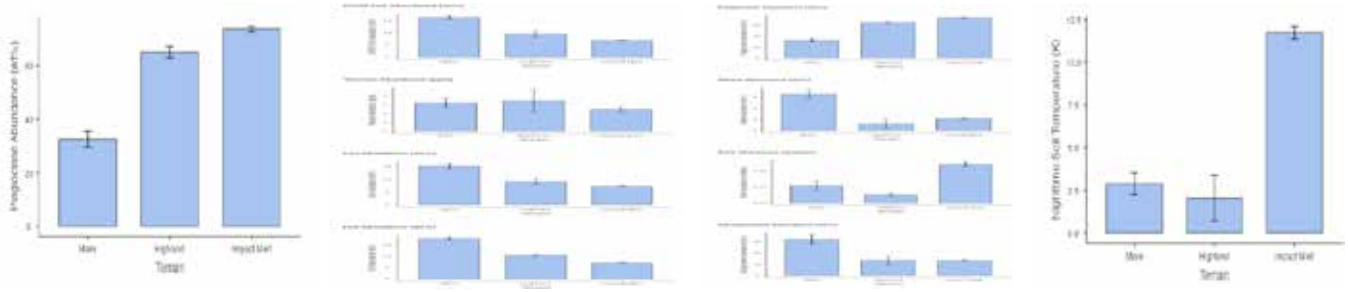

Figure 5. Examples of geophysical variables for the three different lunar terrain types (maria, highlands and impact melts; (a) plagioclase content (%wt), (b) iron content (%wt), (c) rock abundance in regolith (unitless) and (d) nighttime soil temperature (in K). Vertical bars correspond to value variations.

The linear correlation analysis reveals strong relationships between geophysical variables (Figure 6). Notably, Fe-content presents a high positive correlation with nighttime soil temperature (r = 0.92). Additionally, there is a strong positive correlation (r = 0.89) between rock abundances within the regolith and nighttime soil temperatures, which is consistent with Powell *et al.* (2023). In parallel, a significant negative correlation observed between nighttime soil temperatures and thermal inertia (Diviner H-Parameter) (r = -0.97) shows that nighttime temperatures are sensitive to the thermophysical properties of the regolith. High thermal inertia materials, such as large rocks, seem to remain warmer during the lunar night and thus result to anomalously warm nighttime temperatures (Williams *et al.*, 2017).

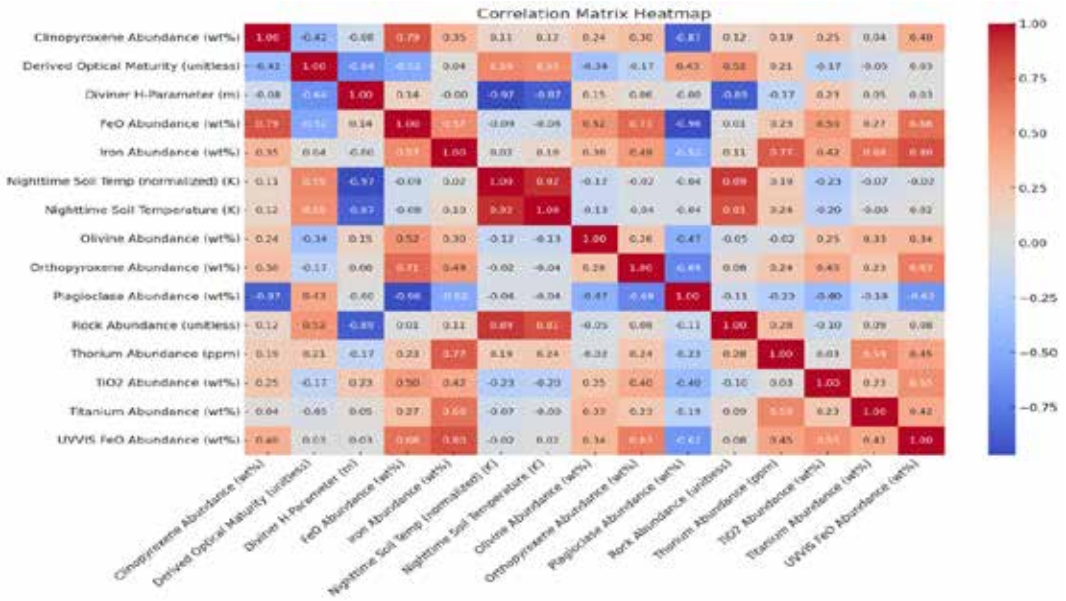

Figure 6. Correlation matrix heatmap of geophysical characteristics. The matrix is symmetric.

In conclusion, the examination of the morphometric and geophysical properties of lunar pits showed that they often have undefined or elliptical shape, varying geometry and are often present in several clusters, near depressions located within crater impact melts. Mineralogy and chemistry are consistent with the geological context of their locations. Although the spatial resolution of the current available data is often a limiting factor, the examination of their properties provides insights to the Moon's geological history, surface processes and stability. Furthermore, lunar pits are potentially linked to subsurface lava tubes or caves which could be promising sites for future human exploration, human habitats and infrastructures. Their unique structure potentially offers natural protection from extreme temperatures, cosmic radiation, and meteorite impacts, making them prime candidates for sustainable lunar bases, landing site selection and long-term lunar sustainability research.

This study is part of Mr. Klimis' BSc thesis. Future continuation of this work includes the study of the each pit cluster, comparison of different pit clusters within different geological contexts, thermal properties (outside and within pits), and the detection of new pits potentially linked to subsurface lava tubes or caves.

References

Carrer, L., Pozzobon, R., Sauro, F., et al., 2024. Radar evidence of an accessible cave conduit on the Moon below the Mare Tranquillitatis pit. Nature Astronomy 8, 1119–1126. (https://doi.org/10.1038/s41550-024-02302-y)

Haruyama J, Hioki K, Shirao M, Morota T, Hiesinger H, Van Der Bogert C, Miyamoto H, Iwasaki A, Yokota Y, Ohtake M, Matsunaga T, Hara S, Nakanotani S, Pieters C.M., 2009. Possible lunar lava tube skylight observed by SELENE cameras. Geophysical Research Letters, 36, L21206.(https://doi.org/10.1029/2009GL040635)

Hong, I-S., Yi, Y., Kim, E., 2014. Lunar Pit Craters Presumed to be the Entrances of Lava Caves by Analogy to the Earth Lava Tube Pits. Journal of Astronomy and Space Sciences 31(2), 131-140. (https://doi.org/10.5140/JASS.2014.31.2.131)

Horvath, T., Hayne, P.O., Paige, D.A., 2022. Thermal and Illumination Environments of Lunar Pits and Caves: Models and Observations from the Diviner Lunar Radiometer Experiment. Geophysical Research Letters 49(14), e2022GL099710. (https://doi.org/10.1029/2022GL099710)

Nesnas, I.A.D., Kerber, L., Sellar, G., Balint, T., Denevi, B., Parness, A.J., Kornfeld, R.P., Smith, M., McGarey, P., Brown, T., Sunada, E., Gonter, K.A., Hockman, B., Hayne, P., et al., 2023. Moon Diver: Exploring a pit's exposed strata to understand

lunar volcanism, Acta Astronautica 211, 163-176, (https://doi.org/10.1016/j.actaastro.2023.05.042)

Powell, T.M., Horvath T., Robles, V.L., Williams, J.-P., Hayne, P.O., Gallinger, B.T., Greenhagen, D.S., McDougall, D.S., Paige, D.A, 2023. High-Resolution Nighttime Temperature and Rock Abundance Mapping of the Moon Using the Diviner Lunar Radiometer Experiment With a Model for Topographic Removal. JGR Planets 128(2), e2022JE007532 (https://doi.org/10.1029/2022JE007532)

Robinson, M.S., et al. 2012. Confirmation of sublunarean voids and thin layering in mare deposits. Planetary and Space Science 69(1), 18-27. (https://doi.org/10.1016/j.pss.2012.05.008)

Wagner, R.V., Robinson, M.S., 2022. Lunar Pit Morphology: Implications for Exploration and Science. Journal of Geophysical Research: Planets 127(8), e2022JE007328. (https://doi.org/10.1029/2022JE007328)

Wagner, R.V., Robinson, M.S., 2014. Distribution, formation mechanisms, and significance of lunar pits. Icarus 237, 52-60. (https://doi.org/10.1016/j.icarus.2014.04.002)

Williams, J.P., Paige, D.A., Greenhagen, B.T., Sefton-Nash, E., 2017. The global surface temperatures of the Moon as measured by the Diviner Lunar Radiometer Experiment, Icarus 283, 300-325. (https://doi.org/10.1016/j.icarus.2016.08.012)

Zhu, K., Yang, M., Yan, XY, Li, WK., Feng, W., Zhong,M., 2024. GRAIL gravity gradients evidence for a potential lava tube at Marius Hills on the moon, Icarus 408,115814, (https://doi.org/10.1016/j.icarus.2023.115814)